Coastal winds dynamics in the Peruvian upwelling system under warming conditions : impact of El Niño and regional climate change

Adolfo Chamorro Gómez

Sorbonne Université

École doctorale 129: Sciences de l'Environnement

Laboratoire d'Océanographie et du Climat: Expérimentations et Approches Numériques

Dynamique des vents côtiers dans le système d'upwelling du Pérou dans des conditions de réchauffement: impacts d'El Niño et du changement climatique régional

Coastal winds dynamics in the Peruvian upwelling system under warming conditions: impact of El Niño and regional climate change

par (by)

Adolfo CHAMORRO

Thèse de doctorat de Sciences du climat, de l'atmosphère et des océans

Dirigée par (Directed by): Vincent ECHEVIN et François COLAS

Présentée et soutenue publiquement le 06 décembre 2018

devant le jury composé de :

Francis CODRON	Professeur (Sorbonne Université)	Président
Pierrick PENVEN	Directeur de recherche (IRD/LOPS)	Rapporteur
Claude ESTOURNEL	Directeur de recherche (AERO/OBS-MIP)	Rapporteure
José RUTLLANT	Professeur (Universidad de Chile)	Examinateur
Sébastien MASSON	Physicien adjoint (Sorbonne Université)	Invité

This thesis work is dedicated to my wife, Evelyn, who has been a constant source of support and encouragement during academic challenges and of the life. This work is also dedicated to my parents, Vicente and Francisca, and to my sisters (Yeni, Tatiana, Enma, Selma) and brother (Jonatan), who have always support me unconditionally and whose good examples have taught me to work hard for the things that I aspire to achieve.

Acknowledgements

This research was funded by a PhD fellowship from CIENCIACTIVA/CONCYTEC-PERU to study at the University Pierre and Marie Curie (UPMC) of Paris, France. It is also a contribution to the cooperative agreement between the Instituto del Mar del Perú (IMARPE) and the Institut de Recherche pour le Developpement (IRD)

I would like to specially acknowledge to my advisors, Drs. Vincent Echevin and François Colas from IRD, for their invaluable academic support and patience in the development of this thesis. Also, thanks to Drs. Jorge Tam and Dimitri Gutiérrez, my supervisors at IMARPE. I would also like to acknowledge to all my lab colleagues from LMOECC (Laboratorio de Modelado Oceanográfico, Ecosistémico y del Cambio Climático) at IMARPE and LOCEAN (Laboratoire d'Océanographie et du Climat : Expérimentations et Approches Numériques) at UPMC who have greatly contributed towards my evolution and supported me during the development of this thesis.

Adolfo CHAMORRO **06 décembre 2018**

Sujet : Dynamique des vents côtiers dans le système d'upwelling du Pérou dans des conditions de réchauffement: impacts d'El Niño et du changement climatique régional

Résumé : Le système d'upwelling péruvien est l'un des systèmes marins côtiers les plus productifs de l'océan mondial. Comme dans les autres systèmes d'upwelling, le vent de surface le long de la côte est le principal moteur de l'upwelling, amenant des eaux froides et riches en nutriments vers la couche de surface où se produit la production primaire. Une caractéristique unique du système d'upwelling du Pérou est sa proximité avec l'équateur: lors des événements El Niño dans le Pacifique équatorial, l'upwelling côtier est très réduit en raison de l'advection vers l'est des eaux chaudes équatoriales. Cette thèse vise à étudier la variabilité du vent côtier et ses processus lors du réchauffement de la couche de surface, à différentes échelles de temps: (1) des échelles de temps interannuelles, correspondant aux événements El Niño, et (2) des échelles de temps multi-décadaires résultant du changement climatique régional. Une série de domaines emboités d'un modèle atmosphérique régional est utilisée pour simuler le vent de surface. Le modèle reproduit bien la variabilité saisonnière et interannuelle des vents le long des côtes au cours de la période récente. Dans la première partie de la thèse, on étudie les processus responsables de l'augmentation, contre-intuitive, du vent observée au large du Pérou au cours de la période El Niño 1997-1998. Des expériences de sensibilité montrent que le réchauffement inhomogène des eaux de surface, plus important dans le nord, entraîne un gradient de pression accru le long de la côte, accélérant le vent. Dans une seconde partie de la thèse, l'évolution des vents côtiers est étudiée dans le scénario du «pire cas» du changement climatique RCP8.5. La circulation atmosphérique est simulée à l'aide d'une descente en échelle dynamique d'un ensemble multi-modèles (31 modèles CMIP5-GIEC) de la circulation atmosphérique moyenne. Forcés par le gradient de pression le long de la côte, les vents diminuent en été (de 0 à 5% environ), tandis qu'ils s'accroissent en hiver (de 5 à 10% environ), renforçant ainsi légèrement le cycle saisonnier. L'utilisation d'un domaine emboité à haute résolution (7 km) de la région du Pérou permet de simuler une augmentation accrue localement des vents en hiver dans la zone de la baie de Paracas. Les changements de vent sont principalement associés aux changements d'intensité et de position de l'anticyclone du Pacifique Sud. Le rôle de facteurs locaux tels que les changements de température de surface entre la terre et la mer s'avère négligeable dans nos simulations.

Mots clés : Modélisation atmosphérique régionale, Downscaling dynamique, Vent côtier, El Niño, Changement climatique.

Subject : ***Coastal winds dynamics in the Peruvian upwelling system under warming conditions: impact of El Niño and regional climate change***

Abstract: The Peruvian upwelling system is one of the most productive coastal marine systems of the world ocean. As in other upwelling systems, alongshore surface wind is the main driver of the coastal upwelling, bringing cold and nutrient rich waters to the surface layer where primary production occurs. An unique feature of this upwelling system is its proximity to the Equator: during El Niño events in the equatorial Pacific, the coastal upwelling is strongly reduced due to the eastward advection of equatorial warm waters. This thesis aims to study the coastal wind variability and the processes responsible for it during the ocean surface layer warming conditions, at different time scales: (1) interannual time scales, corresponding to El Niño events and (2) multi decadal time scales resulting from regional climate change. A suite of regional atmospheric model embedded domains is used to simulate the surface winds. The model reproduces well the seasonal and interannual variability of alongshore winds in the recent period. In the first part of the thesis, the counter-intuitive wind increase observed off Peru during the 1997-1998 El Niño is studied. Sensitivity experiments show that the inhomogenous alongshore surface warming, larger in the north, drives an enhanced alongshore pressure gradient that accelerates the alongshore wind. In the second part of the thesis, the evolution of coastal wind changes is investigated under the "worst case" RCP8.5 climate change scenario. The atmospheric circulation is simulated using a dynamical downscaling of a multi-model (31 CMIP5-IPCC models) ensemble mean atmospheric circulation. Mainly driven by the alongshore pressure gradient, summer winds decrease (by 0–5 %) whereas winter winds increase (by 5–10 %), thus slightly reinforcing the seasonal cycle. The use of a high resolution nested grid (7 km) off Peru allows to simulate an enhanced local wind increase in winter in the Paracas bay area. The wind changes are mainly associated to changes in the intensity and position of the South Pacific Anticyclone. The role of local factors such as land-sea surface temperature changes is shown to be negligible in our simulations.

Keywords : Regional atmospheric modelling, Dynamical downscaling, Coastal wind, El Niño, Climate change.

Contents

Chapter 1

Introduction

1.1 The Peruvian upwelling system

Upwelling systems are regions of the ocean where cooler and nutrient rich waters from the deep ocean are transported to the surface under the action of surface winds. The nutrient rich upwelled water stimulates phytoplankton blooms that create areas with high fisheries resources (Ryther, 1969; Cushing, 1990) on one hand and, on the other hand, it has a strong influence upon the regional climate due to the presence of cool surface waters (Mechoso et al., 2014; Bretherton et al., 2004).

Regions of upwelling are located in equatorial and coastal regions of the ocean. The upwelling systems in the eastern boundaries of the oceans, also known as Eastern Boundary Upwelling Systems (EBUS), are the most productive regions of the world ocean due to their important coastal biological productivity which support large commercial fisheries, up to 20% of the global fish catch (Pauly and Christensen, 1995). The four main EBUS are the Benguela upwelling system situated off southwestern Africa, the Canary upwelling system off northwestern Africa, the California upwelling system off western North America, and the Humboldt upwelling system off western South America. Due to the biomass of phytoplankton in these regions, upwelling zones can be identified by high concentrations of Chlorophyll-a (Fig. 1.1).

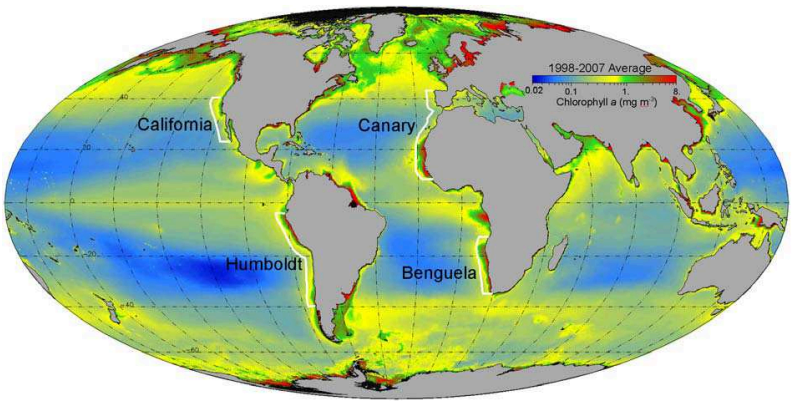

Fig. 1.1 *Chlorophyll-a concentration from SeaWIFS satellite for the 1998-2007 period and EBUS location (Fréon et al., 2009).*

The Peruvian upwelling system is part of the Humboldt upwelling system and it is located aproximately between 5°S and 20°S along the coast of Peru. It is the most productive region among the EBUS (Chavez et al., 2008). It is of fundamental importance because of its immense fishery resources which support a large part of the regional economy (∼ 10% of the world's fish catch; FAO Fisheries and Aquaculture Statistics, http://www.fao.org/fishery/statistics/).

Upwelling regions are located on the eastern flanks of the large-scale subtropical anticyclones, where winds parallel to the coast directed towards the equator induce the upwelling processes. In particular, the Peruvian upwelling system is located on the eastern flank of the South Pacific Anticyclone (SPA) and the upwelling is induced by southerly alongshore winds associated with the southeast trade winds (Fig. 1.2).

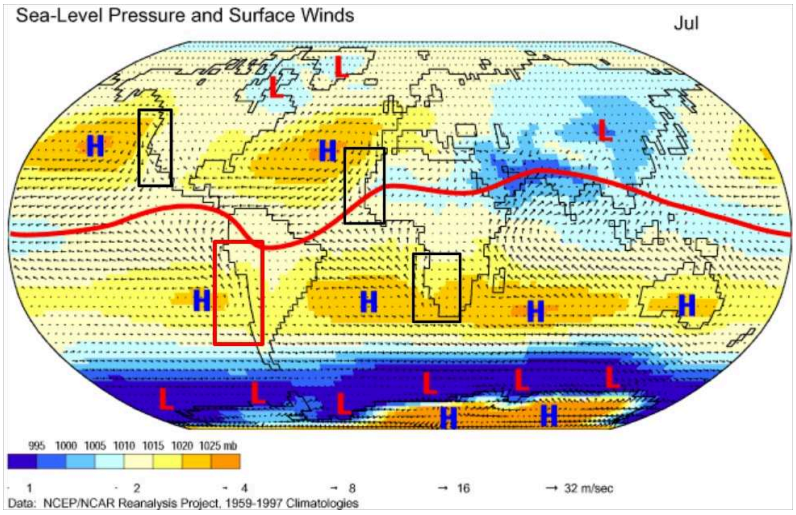

Fig. 1.2 *Monthly average sea level pressure and surface winds for July, using the 1959-1997 climatological base period of the NCEP Reanalysis project. The red line denotes the Inter Tropical Convergence Zone location. (Source of image: Climate Lab Section of the Environmental Change Research Group, Department of Geography, University of Oregon)*

1.1.1 Regional climatic features

The southeast Pacific climate system, where Peruvian upwelling system is located, together with strong ocean coastal upwelling, is characterized by an extensive stratocumulus deck at the top of the marine boundary layer and the longest continental mountain chain in the world named the Andes Cordillera (Fig. 1.3). The stratocumulus deck plays an important role in the regional climate by reflecting incoming solar radiation. The Andes Cordillera reaches altitudes above 4 km, it is located along the west coast of the continent from equator to about 40° and it represents an obstacle for tropospheric flow (Richter and Mechoso, 2006; Takahashi and Battisti, 2007).

Over the tropical ocean at approximately 8°N, the Intertropical Convergence Zone (ITCZ) is located where the northeast and southeast trade winds converge and warm air rises creating a low pressure zone. The rising air produces high cloudiness, frequent

thunderstorms, and heavy rainfall. A high-pressure system is located in the southern part of the Pacific Ocean, called the South Pacific Anticyclone (SPA), associated with the large scale subsidence. Its intensity shows a semiannual variation with maximums in February and October, and minimums in January and May. It is located at its southernmost position (∼37 °S) and far from the continent (∼108 °W) in February and March, and reaches its northermost position (∼26 °S) and close to the continent (∼86 °W) in May (Ancapichun and Garcés-Vargas, 2015). Surface winds that travel from high to low pressure systems over the region are called southerly trade winds. They increase from summer to winter at lower latitudes (5–20 °S) and decrease at higher latitudes (20–40 °S; Rahn and Garreaud (2013)).

The subtropical subsidence over the southeast Pacific ocean together with the ascent over the ITCZ, the low-level trade winds, and the upper-level poleward flow form the Hadley cell, a major feature of the atmosphere general circulation.

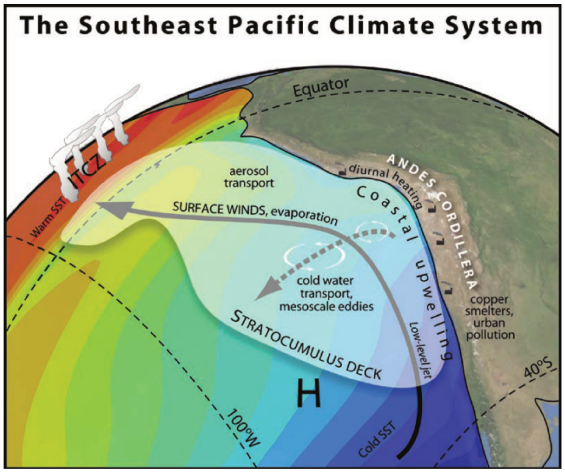

Fig. 1.3 *The Southeast Pacific Climate System (Mechoso et al., 2014).*

1.1.2 Coastal dynamics

We present here a description of the main physical processes and mechanisms that determine the structure of the interacting atmospheric and oceanic boundary layers (the last one is sometimes called the Ekman layer; Fig. 1.4). Their interactions are very important drivers of the coastal wind and the surface currents.

a) The marine atmospheric boundary layer

The marine atmospheric boundary layer, also known as Planetary boundary layer (PBL), is part of the lower troposphere that interacts directly with the sea surface through turbulent transport processes. The PBL consists of a surface boundary layer, a well-mixed layer and a capping entrainment layer. The surface boundary layer is the lowest layer of the PBL (∼10 % of the boundary layer) where the air is in contact with the surface and where strong vertical gradients in temperature, humidity and wind exist. Since the PBL height ranges from ∼500 m to 3000 m, the surface layer is 50–300 m thick.

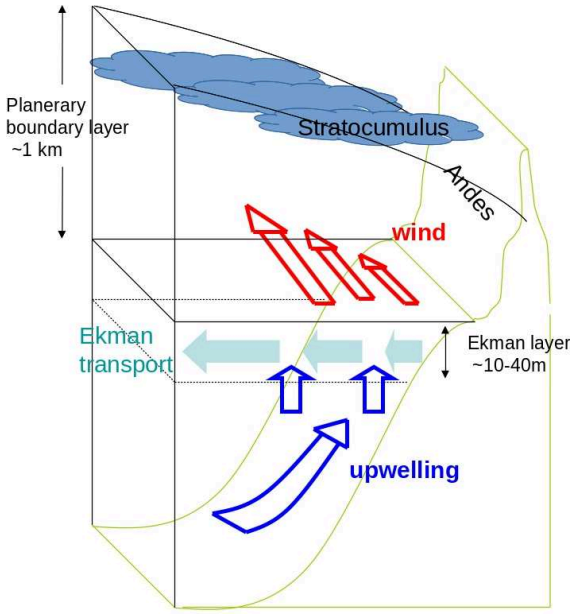

Fig. 1.4 *A scheme of the main physical processes (courtesy of V. Echevin)*

The subtropical subsidence over the southeast Pacific ocean produces a temperature inversion in the PBL (Bretherton et al., 2010) several meters above the surface. In a temperature inversion, a warm air layer (of ∼600 m thick at 30 °S) is trapped between cooler layers above and below. The PBL is often topped by a shallow layer of stratocumulus cloud. In fact, the SEP is covered by the largest and most persistent deck of stratocumulus in the world (Klein and Hartmann, 1993).

A special aspect of the planetary boundary layer is its turbulent nature, which has an effect on the vertical profiles of wind, temperature and moisture within the boundary layer.

b) The oceanic boundary layer

It is the upper layer of the ocean. In the coastal region, upwelling is the main physical process, which is primarily a response of the ocean to the atmospheric forcing. In the Peruvian upwelling system, it is sustained by a permanent moderate wind blowing equatorward. The alongshore wind pushes the surface water away from the coast inducing the rise of cold water to the surface. The wind-driven oceanic flow is confined to the surface in the Ekman layer. In the Ekman layer the frictional force is balanced by the Coriolis force. The net horizontal motion averaged in depth is perpendicular to the wind and is referred as the Ekman transport. The Ekman transport is to the left of the wind in the Southern Hemisphere. On the other hand, the wind intensity, increasing offshore, creates divergence of the Ekman transport which also drives vertical motions and enhances the upwelling. This process is known as Ekman pumping. The profile of the wind decrease towards the coast (Capet et al., 2004), called wind drop-off, is affected by orography and air-sea interactions (Boé et al., 2011; Renault et al., 2015), but it has not been extensively studied for the Peru region. (see red arrows in Fig. 1.4). Zonal and meridional compo-

nents of Ekman transport T_x and T_y, and Ekman pumping W_{Ek} can be computed using the following definitions:

$$T_x = \frac{\tau_y}{\rho f}$$
$$T_y = -\frac{\tau_x}{\rho f}$$

and

$$W_{ek} = \frac{1}{\rho f}\left(\frac{\partial \tau_y}{\partial x} - \frac{\partial \tau_x}{\partial y}\right)$$

where τ_x and τ_y are the zonal and meridional components of the surface wind stress, ρ is the seawater density and f is the Coriolis parameter.

1.2 The El Niño - Southern Oscillation (ENSO)

1.2.1 Large scale characteristics

The ENSO is a irregular oscillation of the ocean-atmosphere climate system that occurs across the equatorial Pacific ocean with a period of 2 to 7 years, caused by recurring redistributions of heat and atmospheric momentum (McPhaden, 1999). ENSO perturbs the east-west atmospheric circulation pattern along the equator, known as the Walker Circulation. ENSO consists of a warm phase, El Niño, and a cold phase, La Niña.

El Niño event, the warm phase of the ENSO, is characterized by unusually warm ocean temperatures in the central and eastern equatorial Pacific, higher sea-level pressures in the Western Pacific and weakening of the Trade Winds leading to a flattening of the thermocline associated with a depression of the thermocline in the eastern Pacific, and an elevation of the thermocline in the west (top right Fig. 1.5). According to the locations of sea surface temperature (SST) anomalies, El Niño can be divided into two types: eastern Pacific El Niño (EP El Niño) and central Pacific El Niño (CP El Niño) (Capotondi et al. (2015); U.S. CLIVAR Report, 2013). La Niña, the cold phase of the ENSO which is the opposite of the El Niño, is characterized by stronger than normal trade winds over the Pacific ocean, and extensive cooling of the central and eastern Pacific ocean and the thermocline moves closer to the surface (bottom right Fig. 1.5).

The Southern Oscillation is the atmospheric component of ENSO. It involves a fluctuaction of the surface pressure accross the equatorial Pacific and occurs in concert with El Niño. They both rely on and modulate each other (Fig. 1.6). Bjerknes (1969) showed that an anomalous positive difference of SST between the West and East Pacific enhances the easterly wind stress in the equatorial Pacific, which in turns amplifies the anomalous positive SST difference (the La Niña phase). The opposite conditions, an anomalous negative difference of SST between the West and East Pacific, would lead to El Niño. This positive feedback between atmosphere and ocean is called the Bjerknes feedback.

El Niño is characterized by anomalous westerly winds in the West-Central Pacific, which cause the generation of eastward propagating oceanic Kelvin waves and westward-moving Rossby waves. Kelvin waves lead to the accumulation of warm water and the deepening of the thermocline in the eastern Pacific (Wyrtki, 1975). Some scientists (Suarez

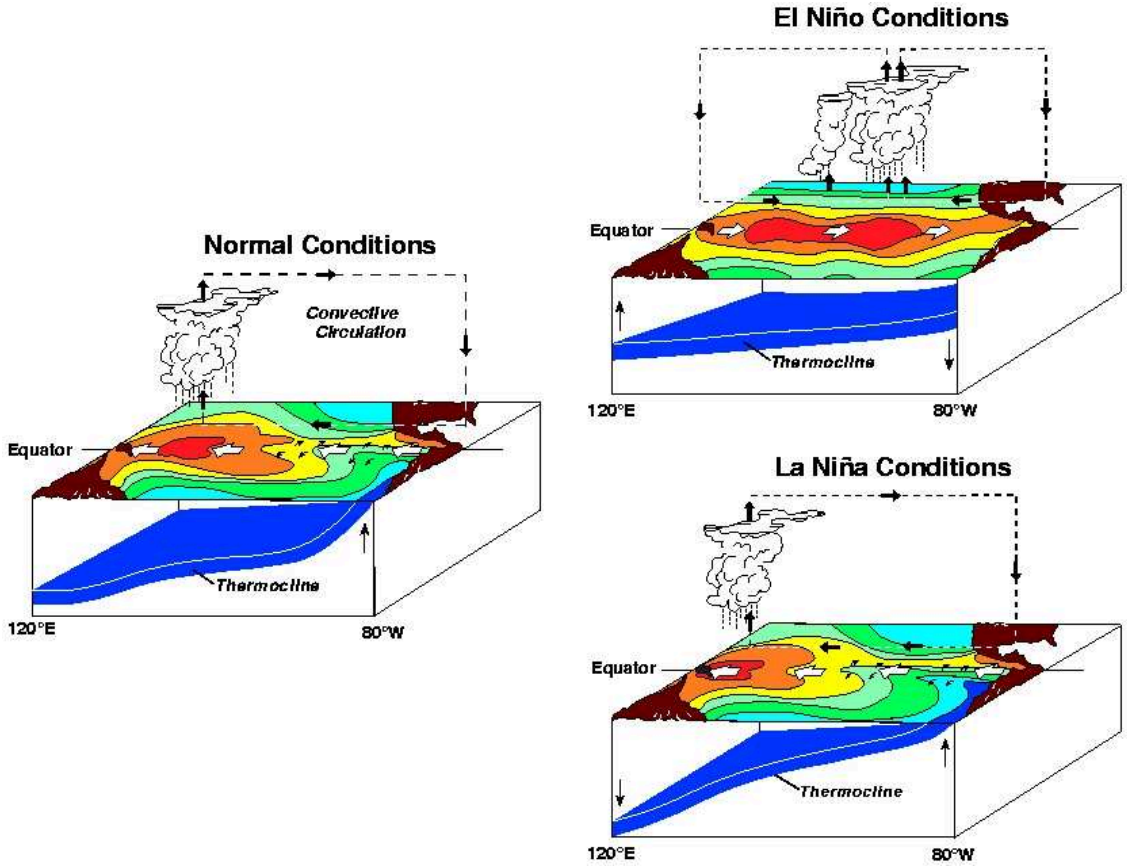

Fig. 1.5 *Schematic diagrams of El Niño, Normal and La Niña conditions. Source:* https://www.pmel.noaa.gov/elnino/schematic-diagrams

and Schopf, 1988; Battisti and Hirst, 1989) have postulated that upwelling Kelvin wave generated by reflection of Rossby wave could cancel the warming in the east (the so-called Delayed-oscillator theory).

1.2.2 The impact of El Niño on the Peruvian upwelling system

A unique aspect of the Peruvian upwelling system is its proximity to the equator in the Eastern Pacific, which places it directly under the influence at interannual time scales of El Niño events.

During El Niño events, SST off the coast of Peru rises up strongly above normal (for example 3 °C during EN 1997-1998; Picaut et al. (2002)), the thermocline and nutricline deepen significantly which reduce the productivity (Barber and Chavez, 1983; Espinoza-Morriberón et al., 2017), while the upwelling favorable winds increase. Due to the deeper thermocline, upwelling brings up warm water with few nutrients, causing serious economic consequences like the reduction of the Peruvian anchoveta fisheries, populations of fish and seabirds (Fig. 1.7). In addition to the fishing industry, agriculture is another of the main sectors of the economy that is severely affected by the El Niño events due to heavy rains, floodings or extremely hot or cold weather (Bayer et al., 2014).

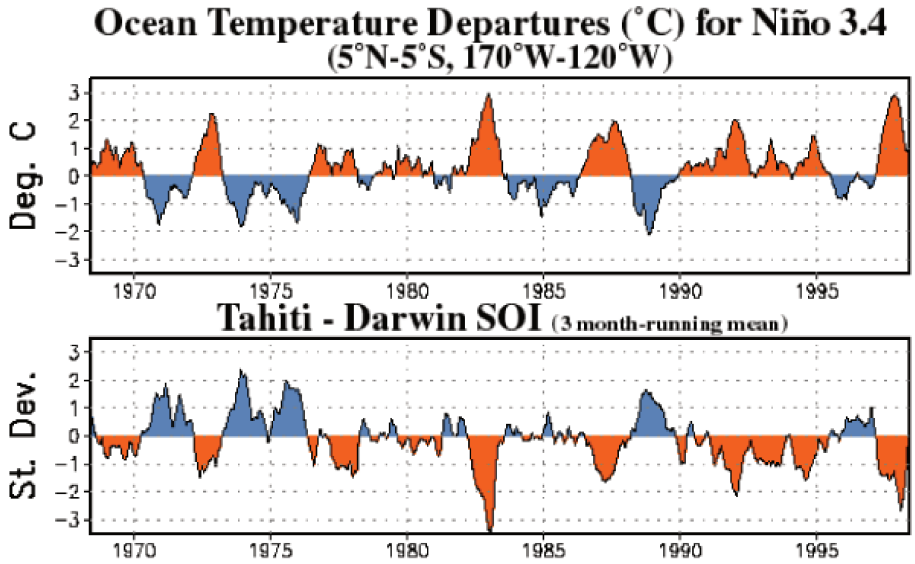

Fig. 1.6 *Times serie of the temperature in eastern equatorial Pacific (averaged over the area 5°N-5°S and 170°W-120°W, the so-called Niño 3.4 index) and the sea level pressure difference between East and West Pacific (the so-called SOI index). Negative values of the SOI and positive values of the Niño 3.4 index correspond to El Niño episodes while a positive SOI index and a negative value of the Niño 3.4 index are typical of La Niña periods. Source:* `http://www.cpc.ncep.noaa.gov/products/analysis_monitoring/ensocycle/soi.shtml`

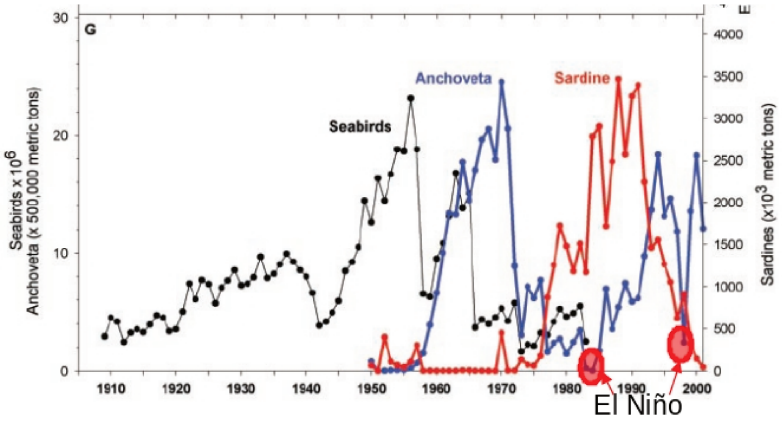

Fig. 1.7 *Time series of seabird abundance, anchovy and sardine landings in the Peruvian upwelling system (Chavez et al., 2003).*

The observations showed that during El Niño events while on one hand the coastal wind is strongly increased (Enfield, 1981; Kessler 2006; Fig. 1.8), on the other hand, the upwelling of cool water is cut off by the poleward advection of tropical waters along the coast (Wyrtki, 1975; Colas et al., 2008). Note that there is still upwelling during El Niño, but of warmer water because of the deepening of the thermocline.

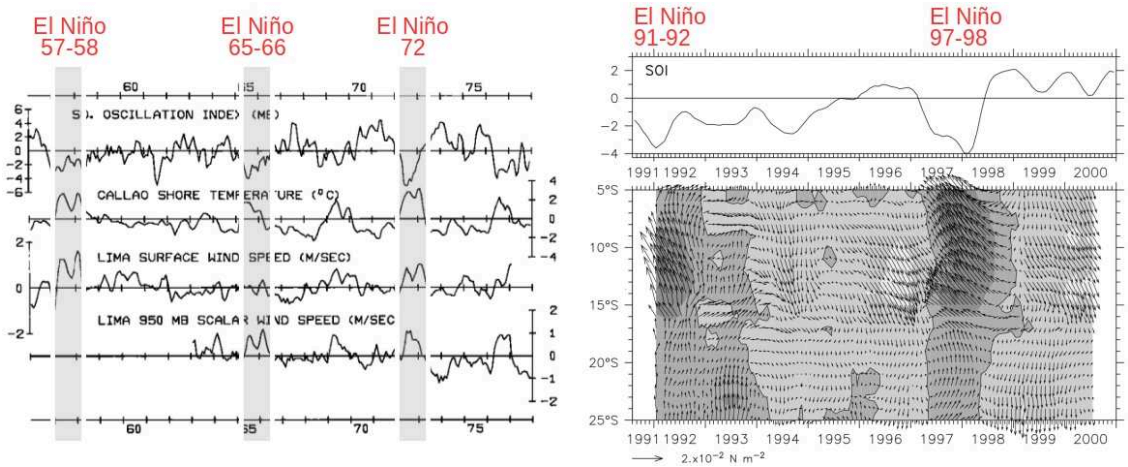

Fig. 1.8 *Coastal wind observations off Peru during El Niño events from anemometer and radiosonde wind data at Lima-Callao airport (left panel; Enfield (1981)) and from ERS satellite (right panel; Kessler (2006)).*

While the occurence of upwelling-favorable winds off the coast of Peru during El Niño events led to realize that coastal warming off Peru must be remotely forced by Kelvin waves (Wyrtki, 1975), the processes that drive the nearshore wind increase off Peru during El Niño remain unclear. Some studies suggested that the wind intensification off the coast of Peru during El Niño could be driven by the strengthening of the cross-shore pressure gradient owing to an enhanced cross-shore thermal contrast between land and sea, which should support a geostrophic wind (Enfield (1981); Bakun and Weeks (2008); Fig. 1.9a). On the other hand, Kessler (2006) suggested that anomalous SST gradients that appear along the Peruvian coasts (due to the fact that SST anomalies are largest in the North coast than in the south during El Niño) could drive a strengthening of the alongshore pressure gradient and so produce the wind acceleration (Fig. 1.9b), but the mechanisms were not studied. In addition, a warm SST anomalies could enhance the turbulent mixing in the PBL and increase the transfer of vertical momentum from upper layers to the ocean surface, causing surface wind intensification (e.g. Wallace et al. (1989); Fig. 1.9c).

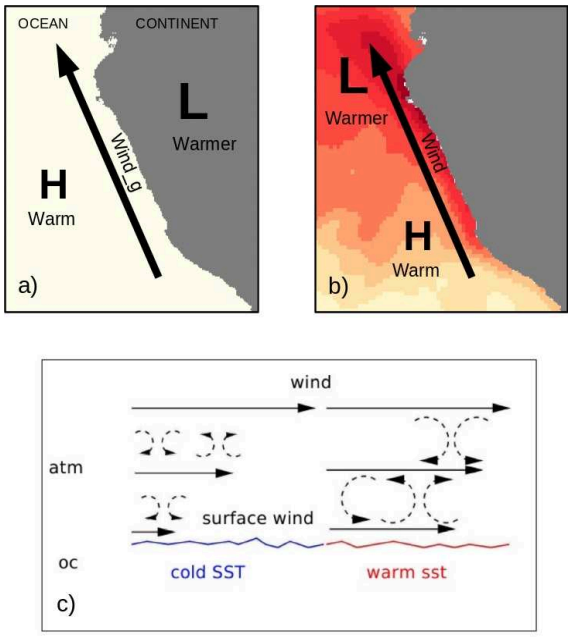

Fig. 1.9 *A scheme of some hypothesis proposed to explain the wind intensification off the Peru coast during El Niño (courtesy of F. Colas)*

1.3 Global climate change

Climate change refers to the change in the mean state or the variability of the climate system over long periods of time (typically decades or longer), due to natural variability or as a result of human activity (IPCC AR4 WG1, 2007).

1.3.1 Greenhouse effect

Solar radiation that passes through the atmosphere warms the surface of the Earth and then some of the radiations go back into space. However, due to the presence of greenhouse gasses in the atmosphere (H_2O, CO_2, CH_4, O_3, etc.) a part of the outgoing radiation is trapped and reemitted in all directions. This so-called natural "greenhouse effect" balances the average temperature on Earth (Fig. 1.10). Without greenhouse gases, the average surface temperature would be very low (around $-18\,°C$ rather than the about $14.5\,°C$ found today) to support life as we know it.

However, as greenhouse gases have increased rapidly in the last decades due to industrial activities, the natural greenhouse effect has intensified which have led to an unusually ever-rising average global temperature (Fig. 1.11).

1.3.2 Climate change scenarios

Climate change scenarios or socioeconomic scenarios are projections of future greenhouse gases (GHG) emissions used by analysts to assess future vulnerability to climate change (Carter et al., 2001). The scientific community, led by the Intergovernmental Panel on Climate Change (IPCC), has developed climate change scenarios which are based on possible

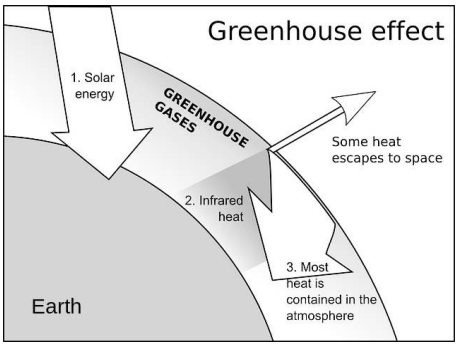

Fig. 1.10 *Schematic of greenhouse effect. Adapted from* https://www.eartheclipse.com

future population levels, economic activity, governance, social values, and technological changes.

a) Idealized scenarios

These are simple scenarios based on the assumption of an progressive increase (1% yr–1) of the atmospheric CO_2 concentration until a doubling ($2CO_2$ scenario) or quadrupling ($4CO_2$ scenario) of its initial value (Covey et al., 2003). The scenario of reference is called "preindustrial" scenario with CO_2 concentration fixed to its preindustrial level (280 ppm; Fig. 1.12).

b) Special Report on Emissions Scenarios (SRES) scenarios

These are a group of 40 scenarios developed by the IPCC in the year 2000. Each scenario is divided into one of four families (A1, A2, B1, B2), each with common themes (e.g: Population changes, energy sources, economic development, etc.). B1 scenario is the more optimistic and A2 is the more pesimistic. Political or legislative actions have no effect on the development of these scenarios, for example commitments made under the Kyoto protocol. The SRES scenarios were used in the IPCC Third Assessment Report (TAR), published in 2001, and in the IPCC Fourth Assessment Report (AR4), published in 2007 (Fig. 1.12).

c) Representative Concentration Pathways (RCPs) scenarios

The RCPs is a set of four new pathways developed for the climate modeling community as a basis for climate change modeling experiments (van Vuuren et al., 2011). It have been adopted by the IPCC for its fifth Assessment Report (AR5) in 2014 and it supersedes the SRES scenarios projections published in 2000. The four RCPs cover a wide range of possible radiative forcing (relative to pre-industrial values) found in the scientific literature published for the year 2100, i.e. from 2.6 to 8.5 W/m2. So, each RCP is based on possible emission scenarios already published. Total radiative forcing is determinated by positive forcing from greenhouse gases and negative forcing from aerosols, where the CO_2 forcing is the most dominant factor (Fig. 1.13).

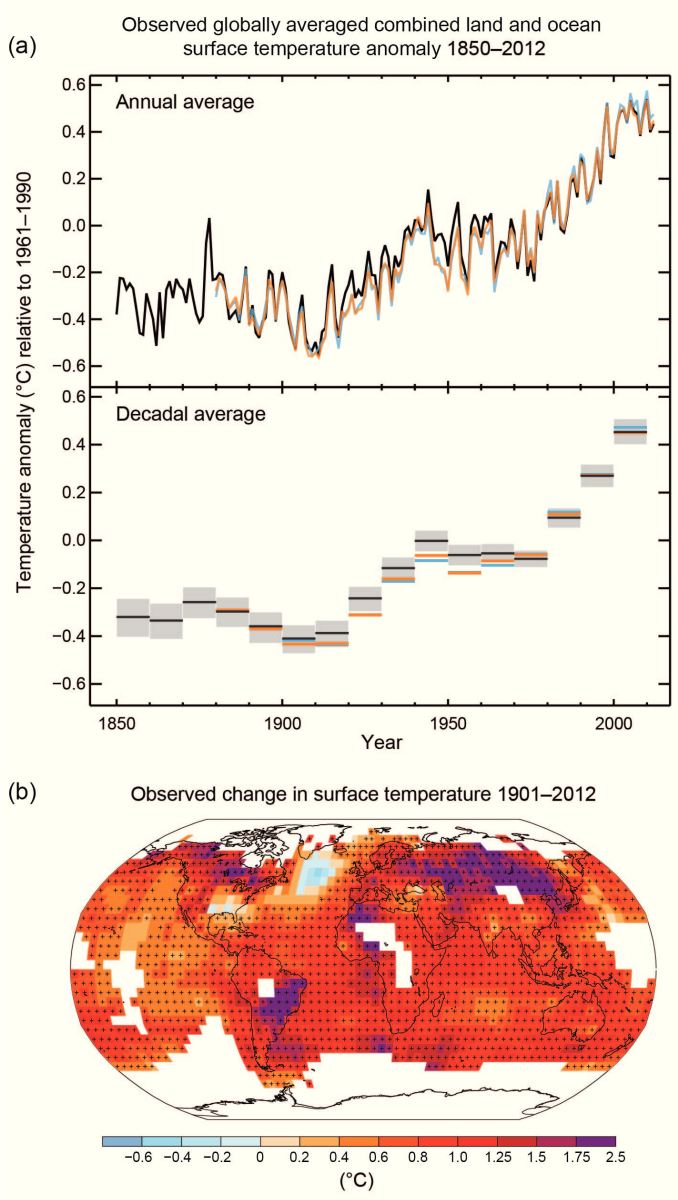

Fig. 1.11 *a) Observed global mean combined land and ocean surface temperature anomalies, from 1850 to 2012 from three data sets. Top panel: annual mean values. Bottom panel: decadal mean values including the estimate of uncertainty for one dataset (black). Anomalies are relative to the mean of 1961-1990. b) Map of the observed surface temperature change from 1901 to 2012 derived from temperature trends determined by linear regression from one dataset (orange line in panel a). Source: IPCC, 2013: Summary for Policymakers.*

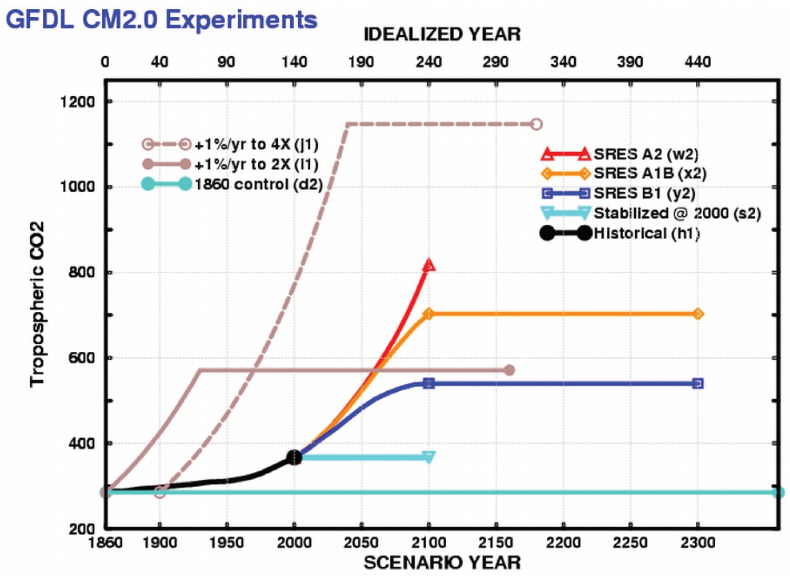

Fig. 1.12 *SRES and idealized scenarios (Stouffer, 2009)*

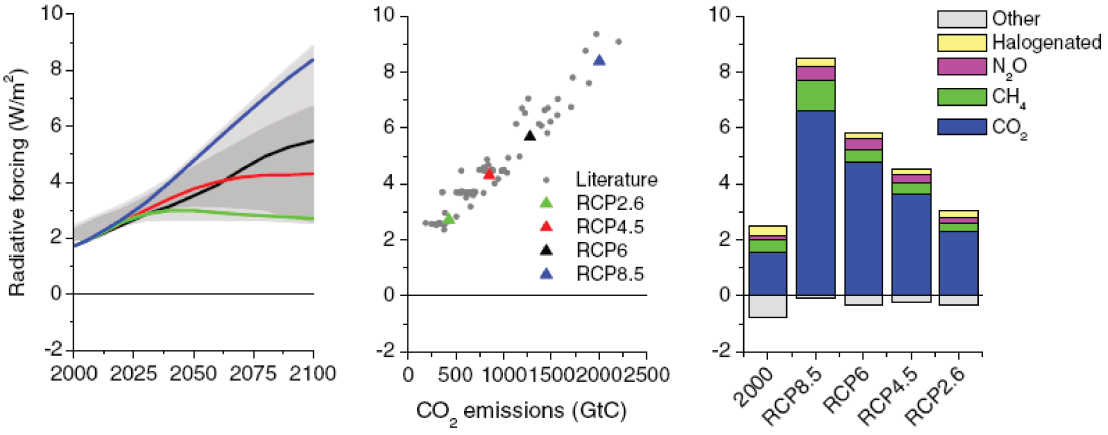

Fig. 1.13 *Trends in radiative forcing (left), cumulative 21st centuryCO2 emissions vs 2100 radiative forcing (middle) and 2100 forcing level per category (right) (van Vuuren et al., 2011).*

1.3.3 Global climate change projections

The Coupled Model Intercomparison Project (CMIP) was established as a standard experimental protocol for studying the climate change simulations of different coupled atmosphere-ocean general circulation models (AOGCMs). The research based on the phase five of CMIP (CMIP5) dataset, which involve 20 climate modeling groups from around the world (with 65 different model configurations), provided much of the new material underlying the Intergovernmental Panel on Climate Change (IPCC) Fifth Assessment Report (AR5).

CMIP5 provide projections of future climate change on two time scales, the so-called near term (out to about 2035) and long term (out to 2100 and beyond). Results from CMIP5 models show that global surface temperature change for the end of the 21st century is likely to exceed 1.5 °C relative to 1850 to 1900 for all RCP scenarios except RCP2.6. It is likely to exceed 2 °C for RCP6.0 and RCP8.5, and more likely than not to exceed 2 °C for RCP4.5. Surface temperatures increase at a greater rate over land than ocean due to the larger evaporation and heat capacity of oceans waters. Precipitation spatial variability increases, with reduction in the subtropics and increase at high latitudes and low tropical levels (Fig. 1.14).

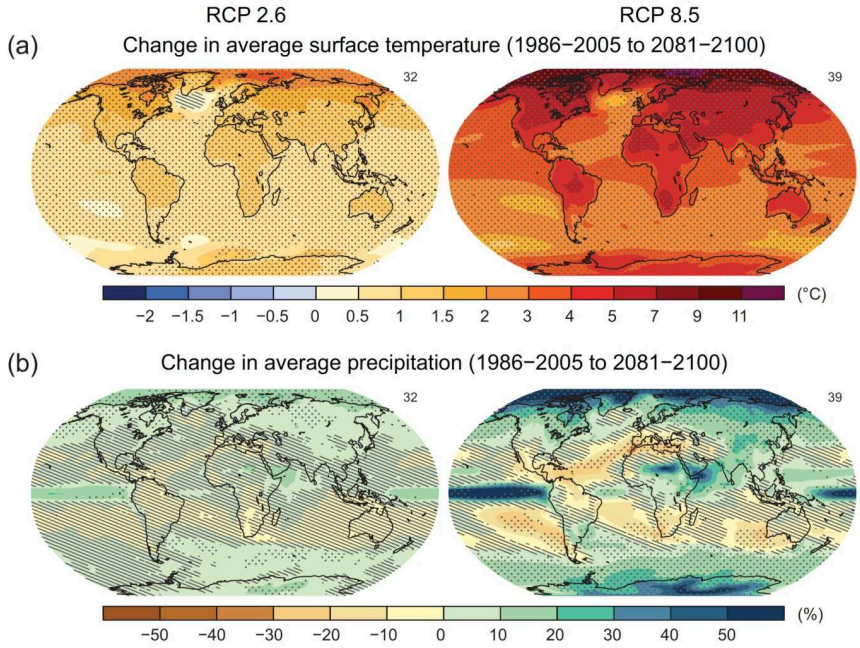

Fig. 1.14 *Maps depicting the annual mean surface temperature change (in °C) and the average change (in %) in annual mean precipitation for the RCP2.6 and RCP8.5 scenarios for the time period between 2081 and 2100 (source: IPCC 2013 SPM)*

1.3.4 Effects of climate change on the upwelling-favorable coastal winds

Changes in alongshore winds, which are the main driving forces of upwelling process in the EBUS, may be driven by changes in the large scale atmospheric circulation, particularly the strength and location of the subtropical high pressure centers.

In that regard, the meridional circulation in the tropics, known as the Hadley circulation, has been predicted to expand toward the poles in response to warming (Lu et al., 2007). Rykaczewski et al. (2015) suggest that the poleward migration of the subtropical atmospheric high pressure systems, which is associated with the Hadley cell expansion, could explain the projected intensification of winds over the major upwelling regions at high latitudes and the weakening of winds at low latitudes that they found using outputs from 21 AOGCMs of the CMIP5 database (Fig. 1.15). Using the same database, Wang et al. (2015) also found that wind-driven upwelling season will increase its duration and become more intense at high (but not low) latitudes.

On the other hand, the strength of the zonal circulation in the equatorial Pacific, known as the Walker circulation, has been predicted to decrease in response to global warming (Vecchi and Soden, 2007). Since the descending branch of the Walker cell is located in the eastern equatorial Pacific, its decrease could lead to reduced winds in northern Peru, assuming that a continuity of low level airflow exists between the Peruvian trade winds and the equatorial trade winds. However, the links between the zonal Walker circulation and the Peruvian trade winds have not been studied and thus are uncertain. In fact, as mentioned above, it has been observed that equatorial trade winds may decrease while coastal winds off Peru may increase, as during El Niño events (Kessler, 2006).

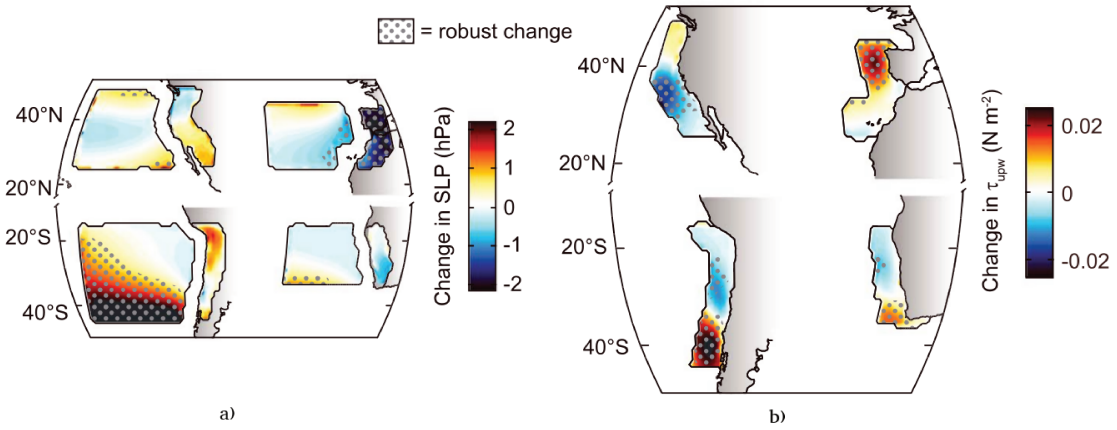

Fig. 1.15 *a) Projected mean change between the periods 2071-2100 (scenario RCP 8.5) and 1861-1890 (historical) for a) sea level pressure and b) meridional wind stress for the main EBUS regions (Figure adapted from Rykaczewski et al. (2015)). Data obtained from 21 AOGCMs of CMIP5 project. Note that Humboldt upwelling system was cut by the north at 15°S.*

In addition to the impact of large scale atmospheric circulation changes, Bakun (1990) proposed that the nearshore winds in upwelling regions may increase in the future due to the increase of land-sea temperature difference. He suggested that under global warming, due to the increase of the greenhouse gases, land temperature will rise faster than ocean

temperature driving an enhancement of the cross-shore pressure gradient and thereby increasing the upwelling favorable winds.

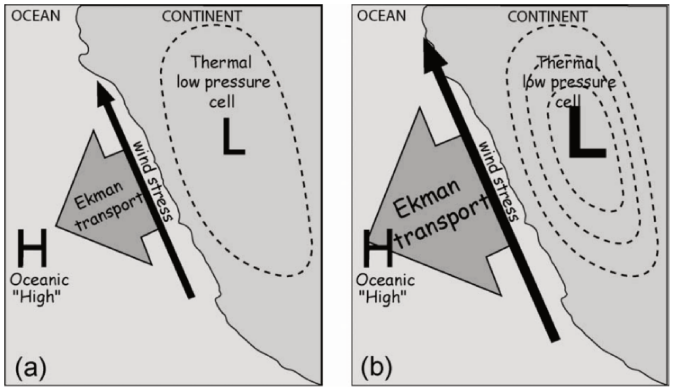

Fig. 1.16 *Diagram of Bakun's mechanism for the upwelling favorable wind intensification (Bakun and Weeks, 2008).*

Bakun based his hypothesis on wind observations reported by ships at sea (COADS data base), which show a positive trend in upwelling favorable winds over the last decades in the four major eastern boundary upwelling systems (Fig. 1.17). However, these observations were partly biased due to increases in anemometer height of ship masts (Tokinaga and Xie, 2011). Narayan et al. (2010) show that the trends in meridional wind stress in the four major upwelling systems obtained from three different datasets (COADS, NCEP/NCAR and ERA-40) differ substantially from each other. In an attempt to investigate if contemporary wind trends support Bakun's hypothesis, Sydeman et al. (2014) performed a statistical analysis from 22 published studies and found an increased probability of wind intensification within most upwelling systems, but mainly at higher latitudes.

a) Regional modelling studies on the Peruvian upwelling system

In the Humboldt upwelling system, a possible strengthening of the upwelling-favorable winds was provided by the observations of a negative trend in coastal SST off northern Chile (Falvey and Garreaud, 2009) and off central and southern Peru (Gutiérrez et al., 2011). However, these trends could be associated to low frequency climate variations (interannual to multidecadal) that may confound trends in relatively short time series. For example, Vargas et al. (2007) showed using data from marine sediments that interdecadal variability of coastal winds in the Peru-Chile current is associated with Pacific Decadal Oscillation (PDO), that is a long-lived El Niño like pattern of Pacific climate variability.

There are not many references on the regional impact of climate change on coastal winds in the Humboldt upwelling system. Garreaud and Falvey (2008) perfomed a dynamic downscaling (using a regional dynamical model) of the Hadley Center model under A2 and B2 climate scenarios and found an intensification of the wind off Chile, consistent with the observed downward trend in ocean temperatures. Goubanova et al. (2011) applied a statistical downscaling method to the outputs of the IPSL-CM4 model under the pre-industrial, $2CO_2$ and $4CO_2$ climate scenarios and found a wind decrease in summer off Peru and a wind increase during all seasons off Chile (Fig. 1.18). These results can

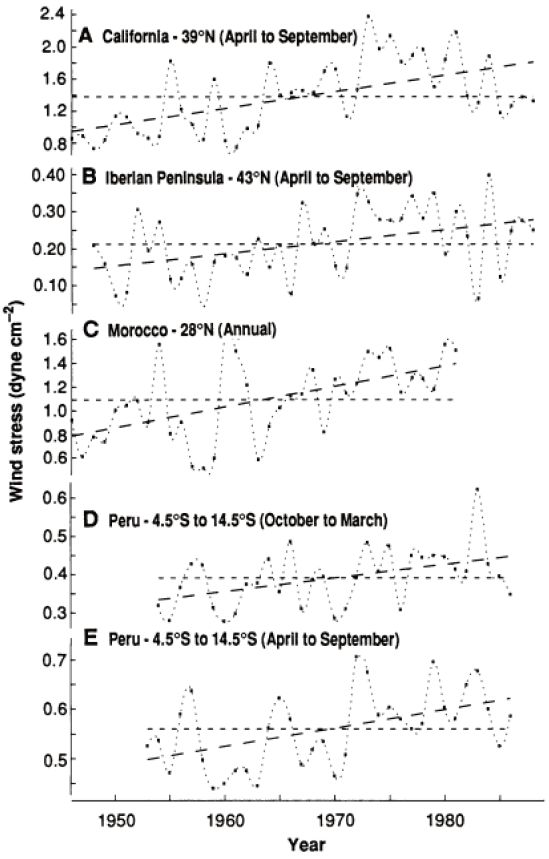

Fig. 1.17 *Monthly average of alongshore wind stress off A) California, B) the Iberian Peninsula, C) Morocco and, D) and E) Peru. Short and longer dashes indicate the long term mean and the linear trend of each time serie, respectively. Adapted from (Bakun, 1990).*

be explained by the southeastern displacement of the South Pacific Anticyclone observed in low resolution IPSL-CM4 simulations. This has the effect of reducing meridian pressure gradient in the northern Humboldt system and increase it in the southern Humboldt system. These trends have been confirmed by the application of the statistical method to other models of IPCC (Goubanova et al., 2011). Belmadani et al. (2014) confirmed these results in a dynamical downscaling study using the atmospheric model LMDz, which achieves a resolution of 50 km in the Humboldt system. It was forced by the surface temperatures of the climate scenarios used in the study of Goubanova et al. (2011). A wind decrease (increase) off Peru (Chile) was obtained with this model associated with a decrease (increase) in the alongshore pressure gradient associated with the poleward displacement of the South Pacific Anticyclone. No increase in land-sea temperature contrast (i.e. "Bakun's mechanism") was found driving the observed changes (Fig. 1.19).

The limitations of these model-based regional projections are the low spatial resolution (50-100 km), the use of a single global model for the downscaling, and the use of idealized, old and "academic" climate scenarios ($2CO_2$ and $4CO_2$ emission scenarios).

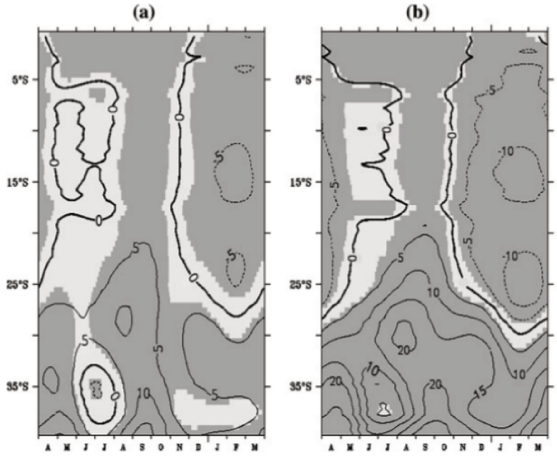

Fig. 1.18 *Change (in %) of the alongshore wind component off Peru and Chile, between 0°S and 40°S, between the scenarios a) pre-industrial and $2CO_2$, b) pre-industrial and $4CO_2$. Adapted from Goubanova et al. (2011).*

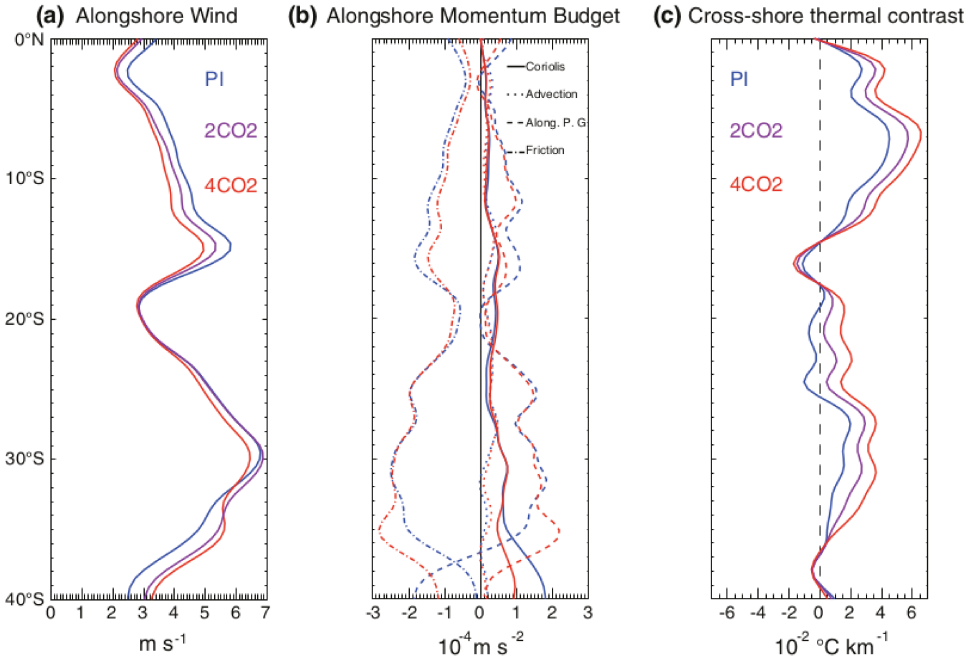

Fig. 1.19 *a) Mean alongshore wind for pre-industrial (PI), $2CO_2$, and $4CO_2$. b) Mean alongshore momemtum balance for PI and $4CO_2$. c) Mean cross-shore temperature along the coast for PI $2CO_2$, and $4CO_2$. Quantities are computed in a one-degree coastal band. From Belmadani et al. (2014).*

b) Regional modelling studies on other upwelling systems

There are few references about the impact of climate change on coastal wind in other upwelling systems.

Miranda et al. (2013) analized outputs from climate change atmospheric simulations (under the IPCC A2 scenario, and the periods 1961-1990 and 2071-2100) with the RACMO regional model at 50 km of horizontal resolution and found an intensification of upwelling favorable wind at three west Iberian capes (Finisterre, Carvoeiro and St. Vincent) of the northern part of the Canary upwelling system. They were associated with an increase of the land-sea thermal contrast and a decrease of the sea level pressure over land, in agreement with Bakun's hypothesis.

Snyder et al. (2003) used the RegCM2.5 regional climate atmospheric model (at 40 km of horizontal resolution) to estimate changes in wind-driven upwelling under increased CO_2 concentration (from 338-369 ppm to 635-686 ppm) in the California upwelling system. They compared the period 1980-1999 with CO_2 concentrations from 338 ppm to 369 ppm against the period 2080-2099 with CO_2 concentration from 635 ppm to 686 ppm. They found an increase of the upwelling-driven wind stress curl off northern California during warmest months (June-September) which produces an intensified upwelling season, and a temporal displacement of one month of the peak of the upwelling season. The land-ocean temperature gradient increased during summer months asociated with the intensification of the wind stress curl, in agreement with the hypothesis of Bakun (1990).

1.4 Research questions

This thesis aims to improve the knowledge of the key mechanisms governing the coastal wind changes off the Peru coast during warming conditions, namely El Niño situation and future climate change.

Coastal winds during El Niño events

Coastal winds off Peru during El Niño events are usually upwelling favorable which contrasts with the observed SST warming. The physical processes producing these wind anomalies have not been studied so far. This thesis addressed this issue through the following questions:

- What are the main forces that induce the alongshore wind anomalies off Peru during El Niño events?
- What is the impact of anomalously warm surface ocean on the low atmosphere conditions during El Niño?
- What are the respective roles of the large scale and local SST forcing on the alongshore wind anomalies?
- What is the role of the South Pacific Anticyclone on alongshore winds off Peru during El Niño event?
- Are the same dynamical processes active during different El Niño events?

Effects of climate change on coastal winds

The initial analysis of the Peruvian studies of the projected change for the upwelling favorable winds off Peru needs further refinement, and its results need to be confirmed by using more recent climate scenarios. This thesis addressed this issue through the following questions:

- What are the projected coastal wind changes in the Peruvian area by performing a dynamical downscaling of the multi model mean of an ensemble of global models?
- Are the projected coastal wind changes off Peru under older idealized scenarios different from those under the new scenarios RCP ?
- Are the projected coastal wind changes sensitive to the resolution of the regional model?
- What are the mechanisms responsible for possible projected wind changes? Are they the same as during El Niño events?

Chapter 2

Data and methods

In this chapter, we present the regional atmospheric model configured to address the research questions about El Niño processes and climate change in the Peru region. First, we describe the data used to build the lateral boundary and initial conditions, as well as the data obtained from observations used to calibrate and validate the model simulations. Then, we provide a brief description of the model. And finally, we show the steps carried out in order to configurate the model and to improve the simulations in our region of interest.

2.1 Data

2.1.1 Global atmospheric reanalysis data

Atmospheric reanalysis data from three database were used to build the initial and lateral boundary conditions for our simulations:

1. ERA-Interim reanalysis data (Dee et al., 2011) is the latest global atmospheric reanalysis produced by the European Centre for Medium-Range Weather Forecasts (ECMWF). It covers the period from 1979 to the present and includes 6-hourly, 4-dimensional variables with a spatial resolution of approximately 80 km and 60 vertical levels from the surface up to 0.1 hPa. It can be downloaded from http://apps.ecmwf.int/datasets/.

2. Climate Forecast System Reanalysis (CFSR, Saha et al. (2010)) is available at a horizontal resolution of 0.313° and 64 vertical levels (6-hourly). Data is available online at https://rda.ucar.edu/datasets/ds093.1/ from 1979 to 2010.

3. NCEP2 reanalysis (Kanamitsu et al., 2002) is a product from the National Center for Environmental Prediction (NCEP) and National Center for Atmospheric Research (NCAR). NCEP2 data has a spatial resolution of 2.5°, 17 vertical levels and temporal resolution of 6 h, covering 1979-present. It is a improved version of NCEP reanalysis in which errors were fixed and parameterization of physical processes were updated. It can be downloaded from https://www.esrl.noaa.gov/psd/.

ERA-Interim was used for the study about El Niño (chapter 3) and NCEP2 for climate change (chapter 4). CFSR was used for the model domain configuration (see section 2.3).

2.1.2 CMIP5 Models

The outputs from thirty one (31) CMIP5 models, for the historical runs from 1989 to 2009 and RCP8.5 scenario from 2080 to 2100, were assembled for the climate change study. Information about each model is listed in Table 2.1. The variables used to build the boundary conditions and the initial state (humidity, air temperature, zonal and meridional wind component, atmospheric pressure and sea surface temperature) were interpolated to a common $1^\circ \times 1^\circ$ grid before the multimodel mean was calculated.

Number	Model	Institution	Resolution (in degrees)
1	ACCESS1-0	CSIRO-BOM (Australia)	1.875×1.25
2	ACCESS1-3	CSIRO-BOM (Australia)	1.875×1.25
3	bcc-csm1-1	BCC (China)	1×1.33
4	BNU-ESM	GCESS (China)	2.8×2.8
5	CanESM2	CCCma (Canada)	2.8125×2.8125
6	CCSM4	NCAR (USA)	0.9×1.25
7	CESM1-BGC	NSF-DOE-NCAR (USA)	0.9×1.25
8	CESM1-CAM5	NSF-DOE-NCAR (USA)	0.9×1.25
9	CMCC-CM	CMCC (Italy)	0.75×0.75 (L31)
10	CMCC-CMS	CMCC (Italy)	0.75×0.75 (L95)
11	CNRM-CM5	CNRM-CERFACS (France)	1.5×1.5
12	CSIRO-Mk3-6-0	CSIRO-QCCCE (Australia)	1.875×1.875
13	FGOALS-g2	LASG-CESS (China)	3×2.8
14	FIO_ESM	FIO (China)	2.8×2.8
15	GFDL-CM3	NOAA GFDL (USA)	2×2.5
16	GFDL-ESM2G	NOAA GFDL (USA)	2×2.5
17	GFDL-ESM2M	NOAA GFDL (USA)	2×2.5
18	HadGEM2-CC	MOHC (UK)	1.25×1.875
19	HadGEM2-ES	MOHC (UK)	1.25×1.875
20	inmcm4	INM (Russia)	1.5×2.0
21	IPSL-CM5A-LR	IPSL (France)	1.875×3.75
22	IPSL-CM5A-MR	IPSL (France)	1.25×2.5
23	IPSL-CM5B-LR	IPSL (France)	1.875×3.75
24	MIROC5	MIROC (Japan)	2.8×2.8
25	MIROC-ESM-CHEM	MIROC (Japan)	2.8×2.8
26	MIROC-ESM	MIROC (Japan)	2.8×2.8
27	MPI-ESM-LR	MPI (Germany)	1.875×1.875 (L47)
28	MPI-ESM-MR	MPI (Germany)	1.875×1.875 (L95)
29	MRI-CGCM3	MRI (Japan)	1.125×1.125
30	NorESM1-M	NCC (Norway)	1.875×2.5
31	NorESM1-ME	NCC (Norway)	1.875×2.5

Table 2.1 – List of CMIP5 Models used

2.1.3 Observational data

Wind observations from two different satellite-borne scatterometers (ERS and QuikSCAT) were used to evaluate the realism of the modelled surface winds over the sea surface. The two products were processed by CERSAT (2002a, b) and downloaded from http://www.ifremer.fr/cersat. Wind data from ERS are provided at $1° \times 1°$ resolution over the period 1992–2000 at a weekly frequency, and QuikSCAT wind fields at $1/4° \times 1/4°$ resolution over the period 2000-2008 at a daily frequency.

The daily Optimum Interpolation Sea Surface Temperature (OISST) at 1/4° (Reynolds et al., 2007) was used as SST forcing for the atmospheric model. It is commonly known as the Reynolds SST and it is available from https://www.esrl.noaa.gov/psd/data/gridded/data.noaa.oisst.v2.html.

VOCALS-REx (VAMOS Ocean-Cloud-Atmosphere-Land Study Regional Experiment; Wood et al. (2011)) in situ measurements of wind, temperature and air temperature were also used to validated the simulations. The data were collected during oceanographic campaigns that took place in the Southeast Pacific between October and November 2008. We used radiosonde data collected by 216 launches (with altitude increments of 10 m) along a zonal section at 20 °S.

Shortwave radiation at ocean surface from the International Satellite Cloud Climatology Project (ISCCP; Zhang et al. (2004)) onto $1° \times 1°$ and daily resolution used by the OAFlux project (http://oaflux.whoi.edu) were used to evaluate the model solution heat fluxes and cloud cover. Data sets of air specific humidity at surface were also obtained from the OAFLUX project.

2.2 The Weather Research and Forecasting (WRF) model

The Weather Research and Forecasting (WRF) model is a numerical weather prediction (NWP) and atmospheric simulation system designed for both research and operational applications (Skamarock et al., 2008). It is an open-source model which development is led by the National Center for Atmospheric Research (NCAR), the National Oceanic and Atmospheric Administration (NOAA), the Air Force Weather Agency (AFWA), the Naval Research Laboratory, the University of Oklahoma, and the Federal Aviation Administration (FAA). It is suitable for a broad span of applications including real-time NWP, data assimilation development and studies, parameterized-physics research, regional climate simulations, air quality modeling, atmosphere-ocean coupling, and idealized simulations.

Figure 2.1 shows the principal components of the WRF system. It has three main components, the WRF Pre-processing System (WPS), the WRF model and the Post-Processing & Vizualization component. WPS is used for setting initial and boundary conditions (i.e. simulation area, terrain, land use, soil type, etc) on the simulation domain using external data sources. The WRF model contains two dynamical solvers, referred to as the ARW (Advanced Research WRF) core and the NMM (Nonhydrostatic Mesoscale Model) core. The ARW core was used in our simulations. The dynamical core runs the model simulations with selected physical parameterizations, time step, etc. The Post-Processing & Vizualization component refers to the graphics and verification tools used to process the output data.

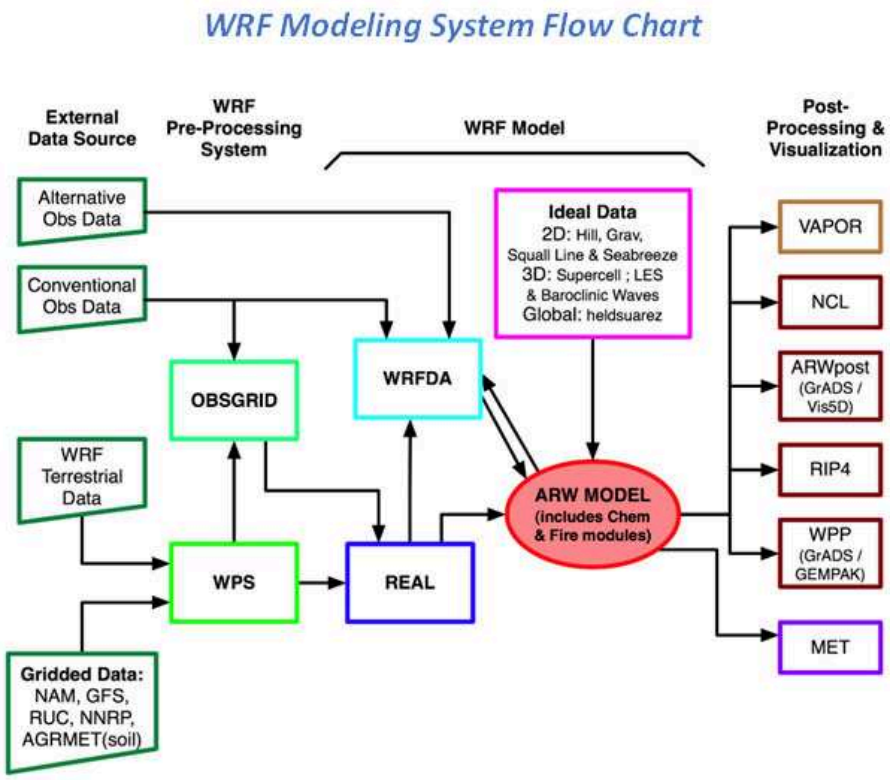

Fig. 2.1 *WRF software infrastructure. It has three main components: the WRF Pre-processing System (WPS), the WRF model and the Post-Processing & Vizualization component. Source:* http://www2.mmm.ucar.edu/wrf/users/model.html.

2.2.1 Primitive equations

The so-called primitive equations are those that govern the evolution of the atmospheric motions. They consist of the following main sets of balance equations.

Equation of state:

$$p = \rho R_d T$$

Conservation of mass:

$$\frac{\partial \rho}{\partial t} + \frac{\partial U}{\partial x} + \frac{\partial V}{\partial y} + \frac{\partial W}{\partial z} = 0$$

Conservation of momemtum:

$$\frac{\partial U}{\partial t} = -U\frac{\partial U}{\partial x} - V\frac{\partial U}{\partial y} - W\frac{\partial U}{\partial z} - \frac{1}{\rho}\frac{\partial P}{\partial x} + fV + U_m$$
$$\frac{\partial V}{\partial t} = -U\frac{\partial V}{\partial x} - V\frac{\partial V}{\partial y} - W\frac{\partial V}{\partial z} - \frac{1}{\rho}\frac{\partial P}{\partial y} - fU + V_m$$
$$\frac{\partial W}{\partial t} = -U\frac{\partial W}{\partial x} - V\frac{\partial W}{\partial y} - W\frac{\partial W}{\partial z} - \frac{1}{\rho}\frac{\partial P}{\partial z} - g + W_m$$

Conservation of energy:

$$\frac{\partial \Theta}{\partial t} + \frac{\partial U\theta}{\partial x} + \frac{\partial V\theta}{\partial y} + \frac{\partial W\theta}{\partial z} = \rho Q$$

where $U = \rho u$, $V = \rho v$, $W = \rho w$ and $\Theta = \rho\theta$. $\vec{v} = (u, v, w)$ are the velocity components in the (x,y,z) directions respectively, θ is the potential temperature, ρ is the air density, f is the Coriolis parameter, P is the atmospheric pressure, U_m, V_m, W_m include vertical and horizontal diffusion, Q is the heat flow per unit of mass, R_d is the gas constant for dry air, and T is the absolute temperature.

The WRF model solves the primitive equations written in flux form using a terrain-following hydrostatic pressure vertical coordinate, which is denoted by η and defined as:

$$\eta = (p_h - p_{ht})/\mu$$

where $\mu = p_{hs} - p_{ht}$, p_h is the hydrostatic component of the pressure, and p_{hs} and p_{ht} refers to values along the surface and top boundaries, respectively. η varies from a value of 1 at the surface to 0 at the upper boundary of the model domain (Fig 2.2).

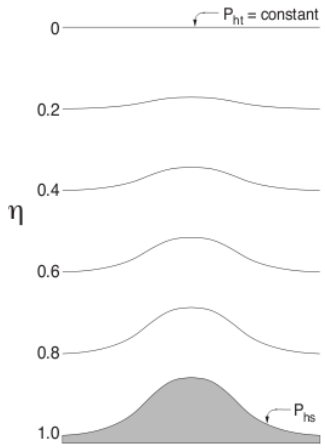

Fig. 2.2 *WRF vertical coordinate η (Skamarock et al. 2008).*

2.2.2 Model discretization

a) Temporal discretization

The model uses a third order Runge Kutta (RK) time integration scheme (i.e. of three substeps) with a user-defined large time step Δt, and with a small step $\Delta\tau$ for acoustic and gravity wave modes.

Defining the prognostic variables in the WRF-ARW solver as $\Phi = (U, V, W, \Theta, \phi', \mu', Q)$ and the model equations as $\Phi_t = R(\Phi)$, the Runge Kutta 3rd order time integration takes

the form of 3 steps to advance a solution $\Phi(t)$ a $\Phi(t + \Delta t)$:

$$\begin{aligned} \Phi^* &= \Phi^t + \frac{\Delta t}{3} R(\Phi^t) \\ \Phi^{**} &= \Phi^t + \frac{\Delta t}{2} R(\Phi^*) \\ \Phi^{t+\Delta t} &= \Phi^t + \Delta t R(\Phi^{**}) \end{aligned}$$

b) Spatial discretization

The spatial discretization in the WRF-ARW solver (which is used for our simulations) uses the Arakawa C-grid staggering for the variables as shown in Fig. 2.3. That is, variables from WRF can be located at one of 4 possible points within each grid cell: at the center of the cell (θ-point), at the center of the left face (u-points), at the center of the front face (v-points), and at the center of the bottom face (w-points).

Scalar variables (e.g. temperature, pressure, etc.) generally live at θ-points. One exception is the geopotential, which lives at w-points. This grid and variable definitions define the spatial discretization for the WRF-ARW solver.

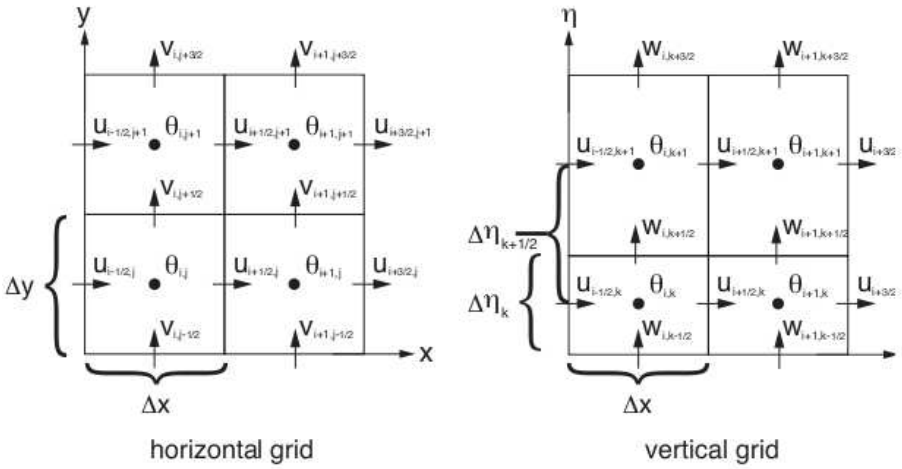

Fig. 2.3 *Horizontal and vertical grids of the WRF-ARW solver (Skamarock et al. 2008)*

2.3 Model configuration

We calibrated the WRF model version 3.3.1 in terms of the sensitivity to physical parameterizations and to the model domain configuration. It was used in our study about El Niño. For our study on climate change, we used the same physical parameterizations and a similar domain configuration nested in other bigger domain (see section 4.2). In addition, we also examined the sensitivity of the model results to the lateral boundary conditions from different databases.

On the other hand, we also present a set of modifications to the WRF code that was done to add some capabilities to the model, and the machine configuration used to run our simulations.

2.3.1 Sensitivity to physical parameterizations

As first step, the model performance with six differents set of physical parameterizations were tested on the domain shown in Fig. 2.4. It has a resolution of 0.25° with 60 vertical sigma levels and covers the Peru and Northern Chile region between 30 °S and 12 °N.

The six sets of different physical parameterizations are summarized in Table 2.2. For this purpose, WRF sensitivity experiments were carried out and compared with observations for the year 2008. The year 2008 was selected as the test period because of the availability of the in-situ observation data from the VOCALS-Rex cruises experiment and QuikSCAT satellite data.

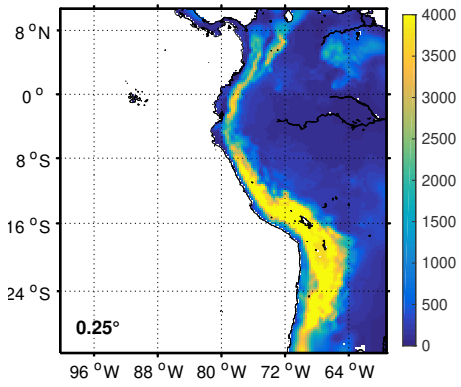

Fig. 2.4 *WRF domain used to evaluate the sensitivity to physical parameterizations.*

	WRF sensitivity experiments					
Physics options	WRF1	WRF2	WRF3	WRF4	WRF5	WRF6
Shortwave radiation	Dudhia	Dudhia	Goddard	Dudhia	RRTMG	Dudhia
Planetary Boundary Layer	YSU	MYNN2	MYNN2	MYNN2	YSU	TEMF
Surface Layer	MM5	MM5	MM5	MYNN	MM5	TEMF

Table 2.2 – Parameterization schemes for physical processes for each of WRF testing experiments

The following parameterizations were used:

- Shortwave radiation:
  - The Dudhia (1989) scheme, a simple downward integration, allowing efficiently for clouds and clear-sky absorption and scattering.
  - Goddard shortwave (Chou and Suarez, 1994), a two-stream multi-band scheme with ozone from climatology and cloud effects.

  - RRTMG shortwave (Iacono et al., 2008), a new shortwave scheme with the MCICA method of random cloud overlap.

- Planetary Boundary Layer:
  - Yonsei University scheme (YSU; Hong and Lim (2006)), a non-local-K scheme with explicit entrainment layer and parabolic K profile in unstable mixed layer.
  - Mellor-Yamada Nakanishi and Niino Level 2.5 PBL (MYNN2; Nakanishi and Niino (2009)), predicts sub-grid TKE terms.
  - Total-Energy Mass Flux (TEMF; Angevine, Jiang and Mauriten ,2010) scheme, a sub-grid total energy prognostic variable, plus mass-flux type shallow convection.
- Surface Layer:
  - MM5 similarity (Zhang and Anthes, 1982), based on Monin-Obukhov with Carslon-Boland viscous sub-layer and standard similarity functions from look-up tables.
  - MYNN surface layer, Nakanishi and Niino PBL's surface layer scheme.
  - TEMF surface layer, Total Energy-Mass Flux surface layer scheme.
- Longwave radiation: RRTM scheme (Mlawer et al., 1997).
- Microphysics: WRF single-moment 6-class scheme (Hong and Lim, 2006).
- Cumulus: Betts–Miller–Janjic scheme (Janjic, 1994).
- Land surface: Noah land surface model (Chen and Dudhia, 2001).

a) Evaluation of near-surface variables

Model-simulated winds, humidity and shortwave flux on the sea surface are validated against satellite observations. Results are presented for the six sets of physical parameterizations (see Table 2.2).

Figure 2.5 shows the mean sea surface wind for the year 2008 from QuikSCAT and the WRF sensitivity experiments. All WRF experiments reproduce the regional pattern of the surface winds in agreement with QuikSCAT observations. They show that winds off the Peru coast are strongest offshore between 6–20 °S and blow predominantly from the northwest direction. They decrease in the nearshore region and are oriented alongshore. The WRF6 experiment shows a marked underestimation of the wind intensity almost everywhere. All the other WRF experiments show a wind speed positive bias nearshore off northern Chile and off the Peru coast (Fig. 2.6), showing that, the model does not reproduce properly the nearshore wind drop-off. It will be shown later (in section 4) that it is an issue partly related to the model horizontal resolution.

The model-simulated shortwave flux is examined. Note that surface meteorological variables and ocean surface dynamics are very sensitive to this variable. Figure 2.7 shows the mean net shortwave flux at the ocean surface for the year 2008 from ISCCP observations and WRF. Observations show two regions of minimum values of about 180-200 and

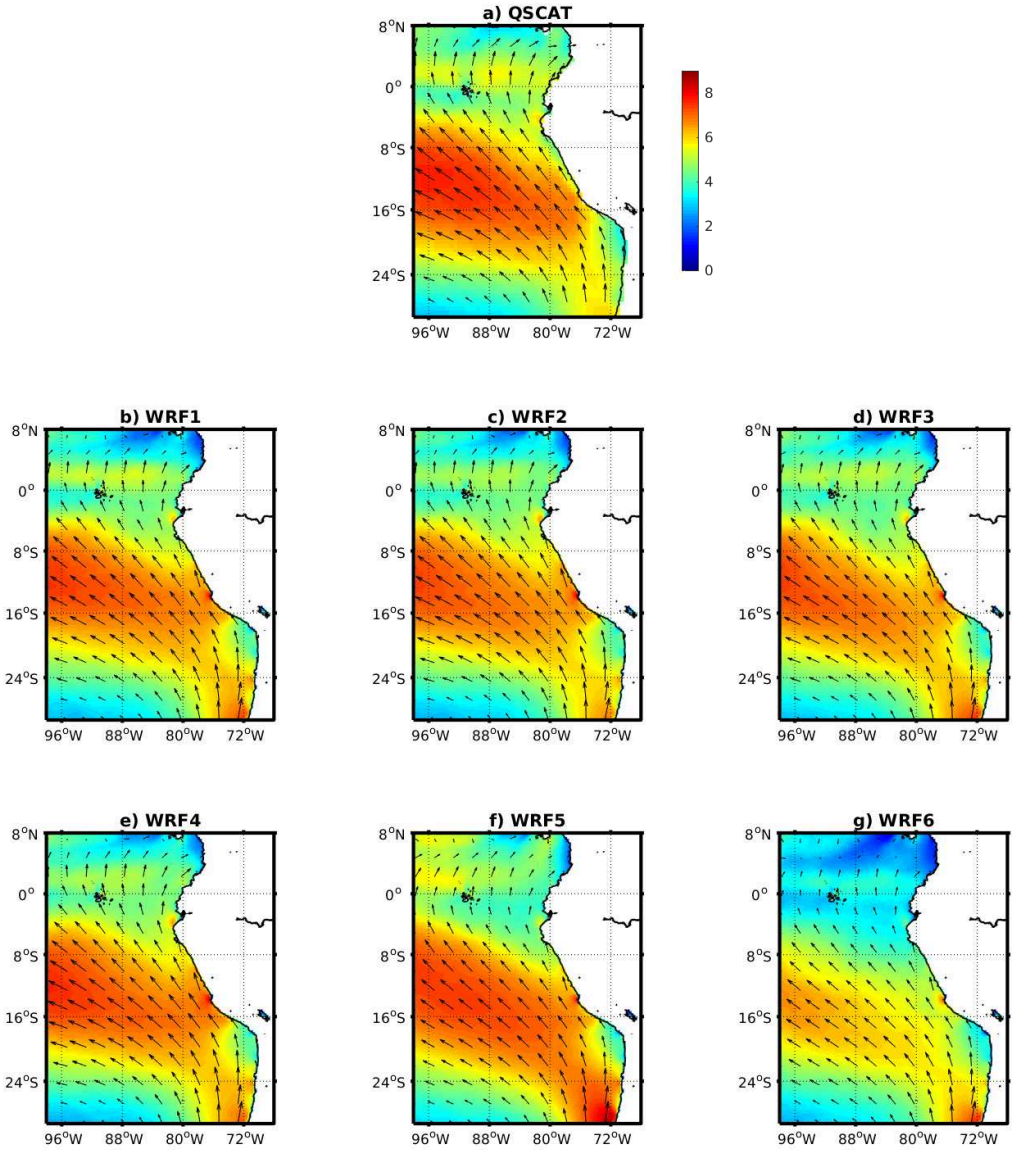

Fig. 2.5 *Mean surface wind speed (in* $\mathrm{m\,s^{-1}}$*, colours) and direction (arrows) for the year 2008 from a) QuikSCAT satellite and b)-g) WRF sensitivity experiments.*

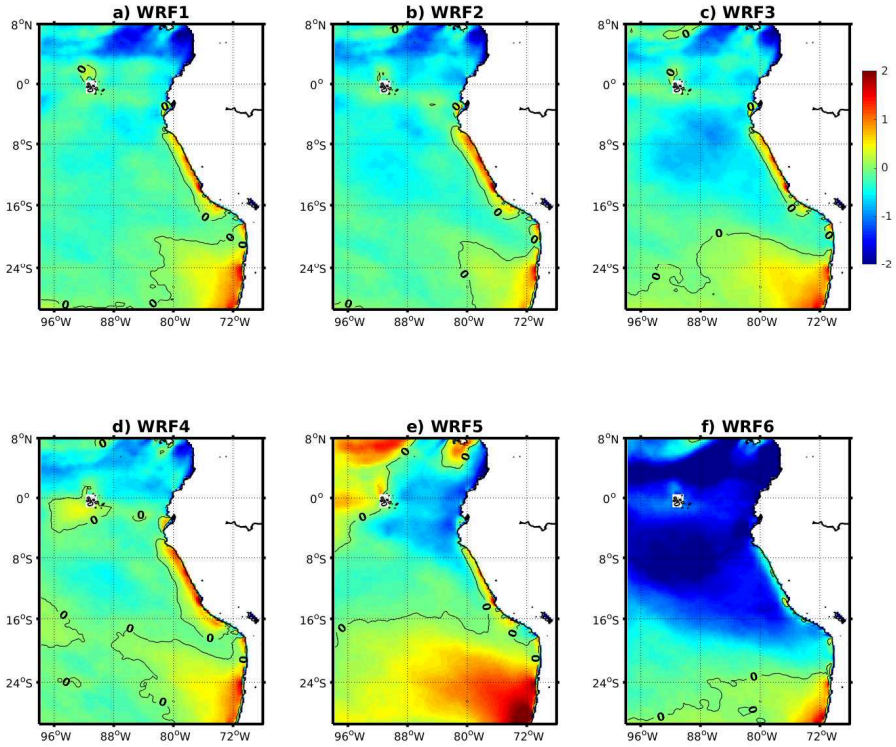

Fig. 2.6 *Mean wind speed bias (in* $\mathrm{m\,s^{-1}}$*) from WRF sensitivity experiments with respect to QuikSCAT observations for the year 2008.*

160-180 $\mathrm{W\,m^2}$, located around 600 km offshore northern Chile and off the coast, north of the equator, respectively. Both minimums are reproduced by WRF1, WRF2, WRF3, WRF4 sensitivity experiments. WRF3 shows a large positive bias everywhere, but WRF5 and WRF6 are worse, since they are not able to reproduce the regional shortwave flux pattern.

Simulated humidity was also evaluated. Figure 2.8 shows the mean water vapor mixing ratio for the year 2008 from OAFLUX observations and WRF sensivity experiments. Observations show that humidity spatial distribution is almost zonally uniform with high values in the north and low values in the south of the domain. It shows values around 9-11 $\mathrm{g\,kg^{-1}}$ off the coast of southern Peru and around 11-15 $\mathrm{g\,kg^{-1}}$ off the northern coast of Peru. All WRF sensitivy experiments reproduce relatively well the regional spatial distribution of humidity, but show the largest biases nearshore off southern Peru and northern Chile (Fig. 2.9). WRF1, WRF5 and WRF6 experiments show a strong positive bias almost everywhere in the model domain.

b) Impact of schemes on vertical profiles

Vertical profiles of wind, temperature and humidity from WRF1 and WRF4 experiments were compared with the VOCALS-REx observations. Figure 2.10 shows cross-shore vertical sections at 20 °S of the mean meridional and zonal wind and temperature of WRF1

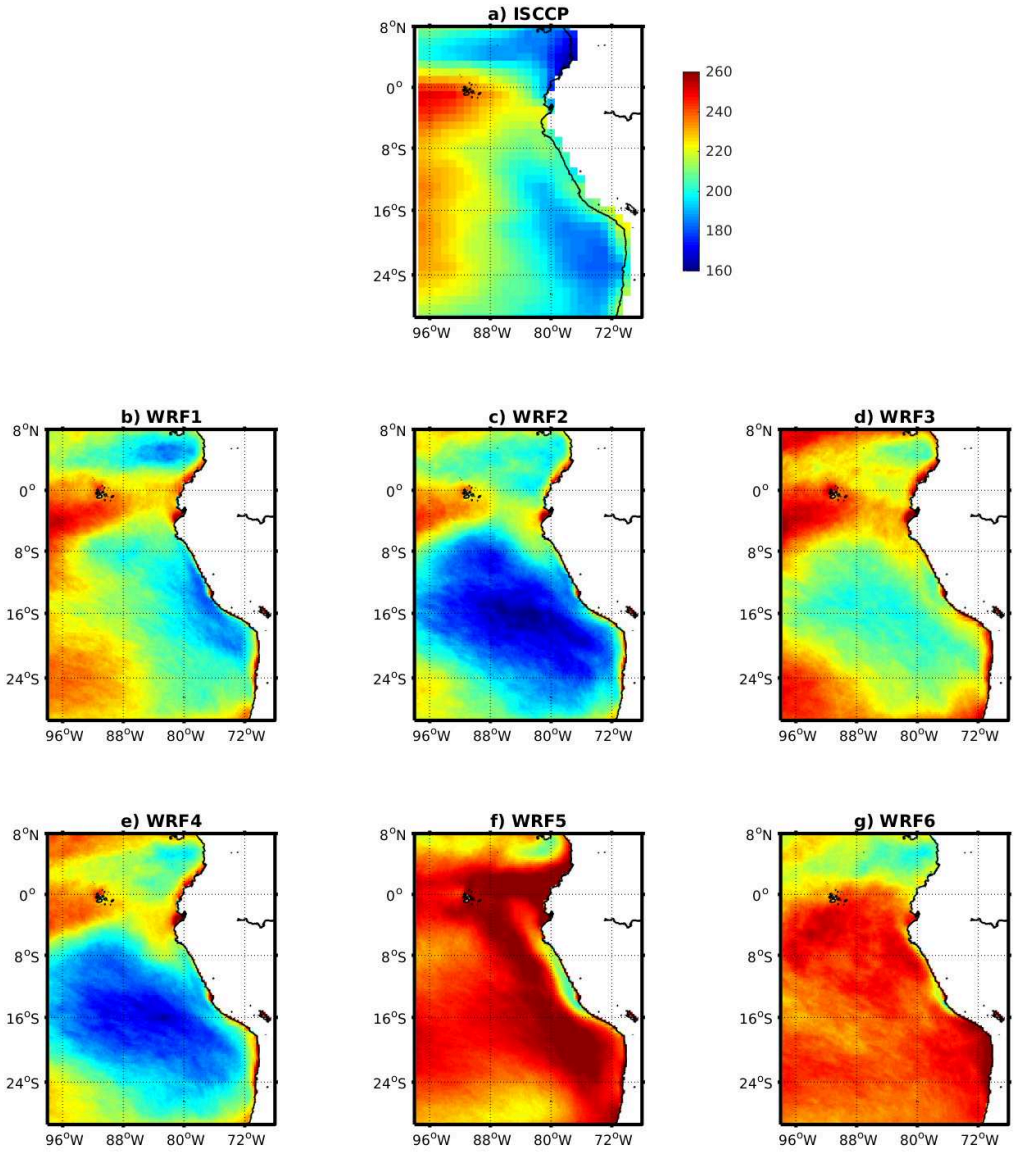

Fig. 2.7 *Mean net shortwave flux at ground surface for the year 2008 (in* $\mathrm{W\,m^{-2}}$*) from a) ISCCP observations and b)-g) WRF sensitivity experiments.*

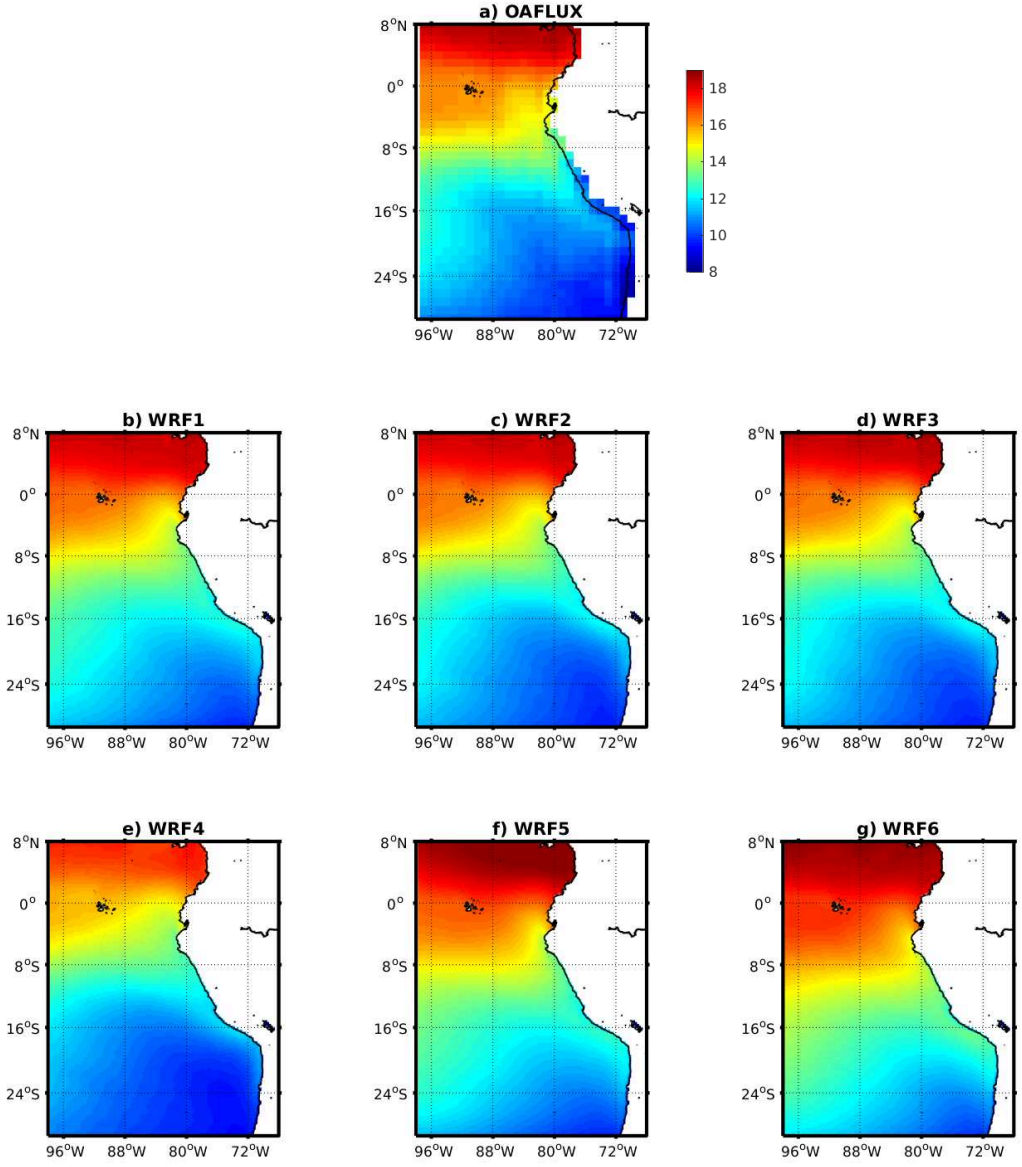

Fig. 2.8 *Mean water vapor mixing ratio for the year 2008 (in* $\mathrm{g\,kg^{-1}}$*) from a) OAFLUX observations and b)-g) WRF sensivity experiments.*

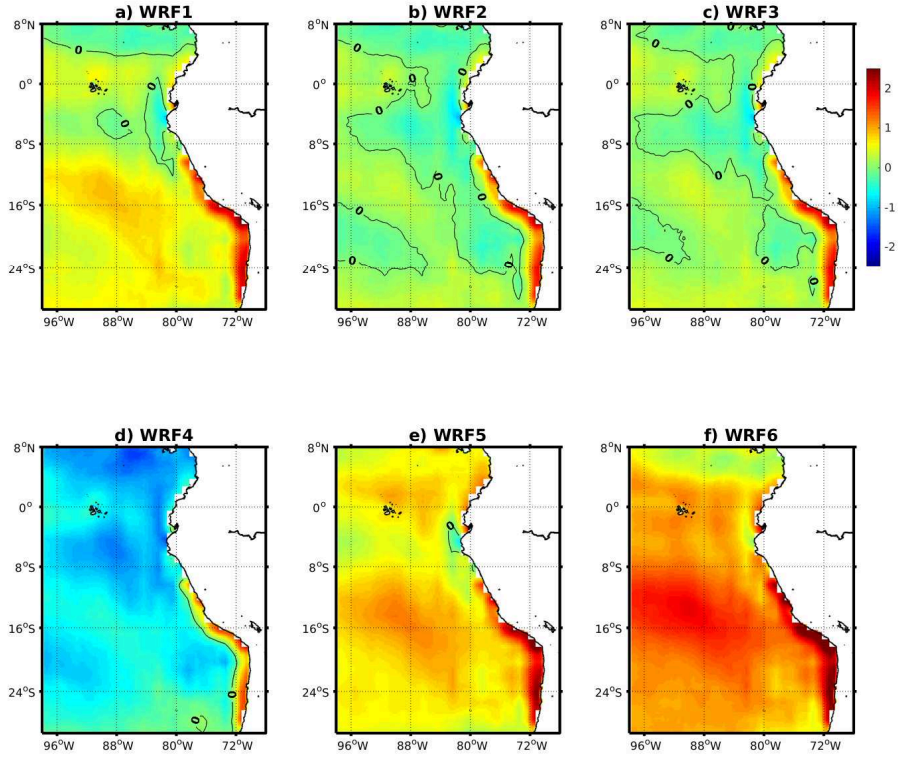

Fig. 2.9 *Mean water vapor mixing ratio bias (in* $\mathrm{g\,kg^{-1}}$*) from WRF sensitivity experiments with respect to OAFLUX observations for the year 2008.*

and WRF4 sensitivity experiments and VOCALS-REx observations between 28 October and 3 November 2008. Both WRF experiments reproduce the zonal and meridional vertical structure of the winds in agreement with observations. They show that meridional winds flow southward at high levels (above ∼600 hPa) and northward near the sea surface, with a maximum intensity offshore at ∼900 hPa in observations and ∼950 hPa in the WRF experiments. The meridional wind changes its direction at height of ∼500 hPa at 85 °W both in model and observations. The height of the wind reversal decreases toward the shore reaching ∼960 hPa in observations and ∼890 hPa at 72 °W in WRF. The vertical structure of temperature shows a temperature inversion between ∼800-950 hPa both in observations and WRF (magenta contours in Figs. 2.10a, b, c). Zonal winds flow eastward at high levels (above ∼700 hPa) and westward near the sea surface. The height of the wind reversal decreases towards the coast, from ∼700 hPa at 85 °W (both observations and WRF experiments) to ∼950 hPa in observations and ∼880 hPa in WRF experiments at 73 °W.

Figure 2.11 shows the vertical profiles of mean potential temperature and humidity at 20 °S,85 °W from WRF1, WRF4 experiments and VOCALS-REx observations between 25 and 27 October 2008. Note that some additional profiles were also calculated for dates close to those of the measurements, which allow to obtain a representation of the high frequency variation of the simulated profile. Vertical profiles of potential temperature are

well reproduced by both WRF experiments near surface and in upper layers. On the other hand, the vertical profile of specific humidity is sligthly better reproduced by WRF4, but it is significantly underestimated by WRF1 between 870 and 920 hPa.

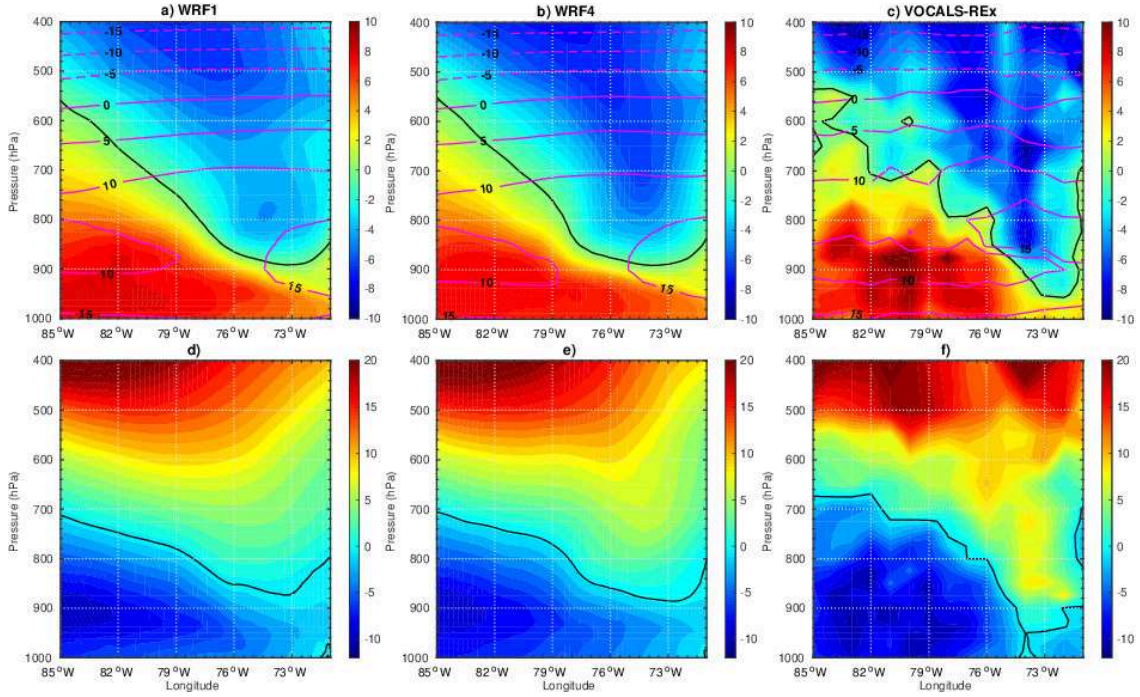

Fig. 2.10 *Cross-shore vertical sections at* 20 °S *of the mean meridional wind (shading, in* $\mathrm{m\,s^{-1}}$*) and air temperature (magenta contours, in* °C*) from a)-b) WRF1 and WRF4 sensitivity experiments and c) VOCALS-REx observations, and zonal meridional wind (shading, in* $\mathrm{m\,s^{-1}}$*) from d)-e) WRF1 and WRF4 sensitivity experiments and f) VOCALS-REx observations. Data averaged between 28 October and 3 November 2008. Black contours indicate zero meridional wind speed.*

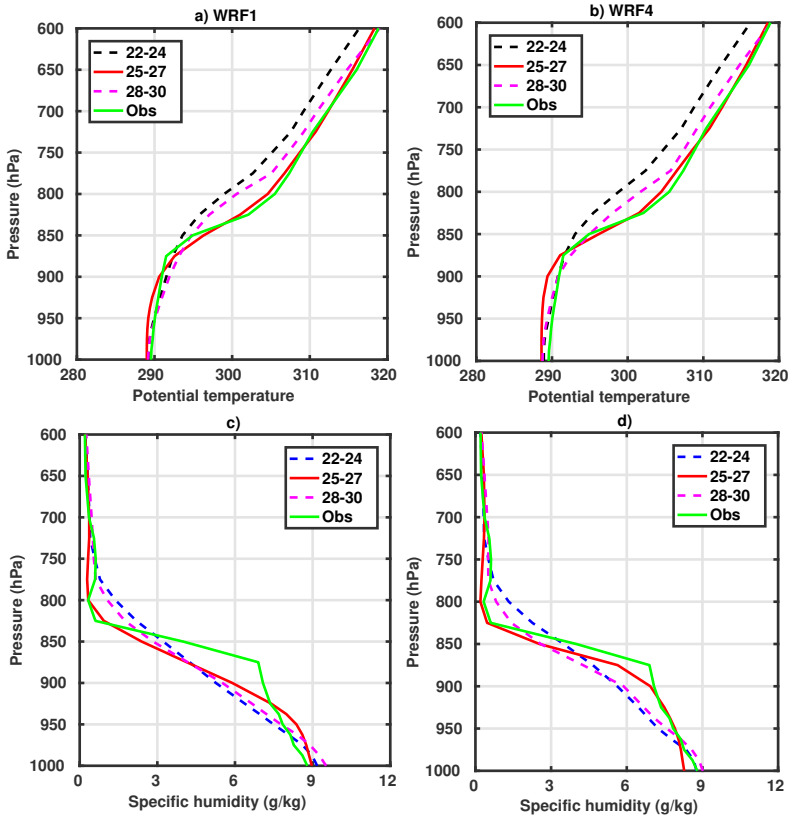

Fig. 2.11 *Vertical profiles at* 20 °S,85 °W *of a)-b) Potential temperature and c)-d) Specific humidity from WRF1 and WRF2 sensitivity experiments and VOCALS-REx observations. Dashed, red and magenta lines correspond respectively to mean profiles between 22-24, 25-27, and 28-30 October 2008 for WRF sensitivity experiments. Green lines correspond to VOCALS-REx observations mean profiles between 25-27 October 2008.*

The analysis carried out in this subsection indicates that the set of physical parameterizations of WRF4 (see Table 2.2) generates better results compared to the other sets of parametrizations, thus this set is used in the experiments hereafter.

2.3.2 Sensitivity to the domain configuration and to the lateral boundary conditions

As a second step, the small domain in Fig 2.4 was nested inside a bigger domain (see Fig. 2.12) to investigate the model sensitivity to the nested domain configuration. Note that the large domain has a resolution of 0.75° and encompasses the South East Pacific and the main part of South America. The number of vertical levels was set to 60 in both domains, defining 21 levels in the first 1000 m, which allows to better represent the complex topography of the Andes mountain.

In order to assess the model sensitivity to the lateral boundary conditions, we forced our simulation by two differents databases: the ERA-Interim and CFSR reanalysis. Simulations were done for the period 1997-1998.

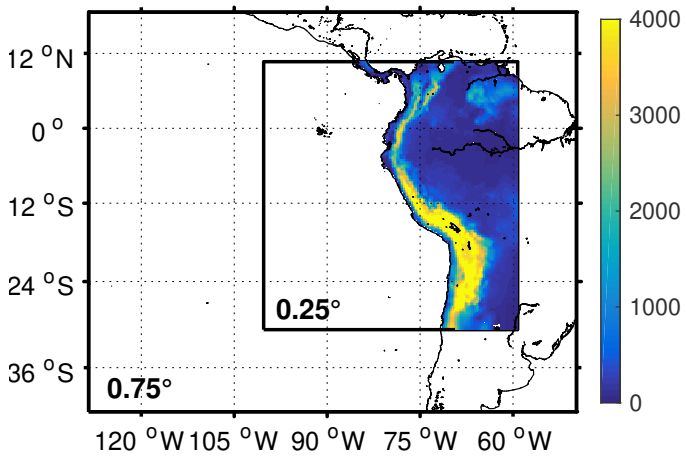

Fig. 2.12 *WRF domains used to evaluate the sensitivity to nested domain configuration and to the lateral boundary conditions*

Figure 2.13 shows the mean surface wind for the period 1997-1998 from WRF simulations with three different configurations. The first of them was configured using a single domain (in Fig. 2.4) and forced by the ERA-Interim reanalysis. The second was configured using the nested domains configuration (in Fig. 2.12) and also forced by the ERA-Interim reanalysis. And the third was also configured using the nested domains but forced by the CFSR reanalysis. In the inner part of the domain, the simulated wind spatial pattern is almost the same for the single and nested configurations. There are major differences in the offshore part of the domain, mainly near its western border. Differences between simulations with different lateral boundary conditions (ERAI and CFSR) are relatively small. Similar differences are observed at high levels in wind and air temperature (Fig. 2.14), that is, small differences in the inner part and major differences in the outer part.

These analyses show that a nested domain can be useful to obtain clean solutions (without lateral boundary efffects) of the model around the border of its domain. Moreover, it should be useful in a future work when the WRF atmospheric fields produced in our simulations will be used to force a regional oceanographic model. On the other hand, the sensitivity of model results to the change of the database used to build the lateral boundary conditions is weak, especially in the nearshore region. Thus, the nested domain configuration was used in our simulations hereafter.

2.3.3 WRF code modifications

A set of modifications to the WRF code was performed (following Oerder (2016)) in order to add some capacities to the model : (1) to compute the turbulence shear stress (2) to extract the individual horizontal momentum tendency terms and (3) to record the mean cumulative of the momemtum terms.

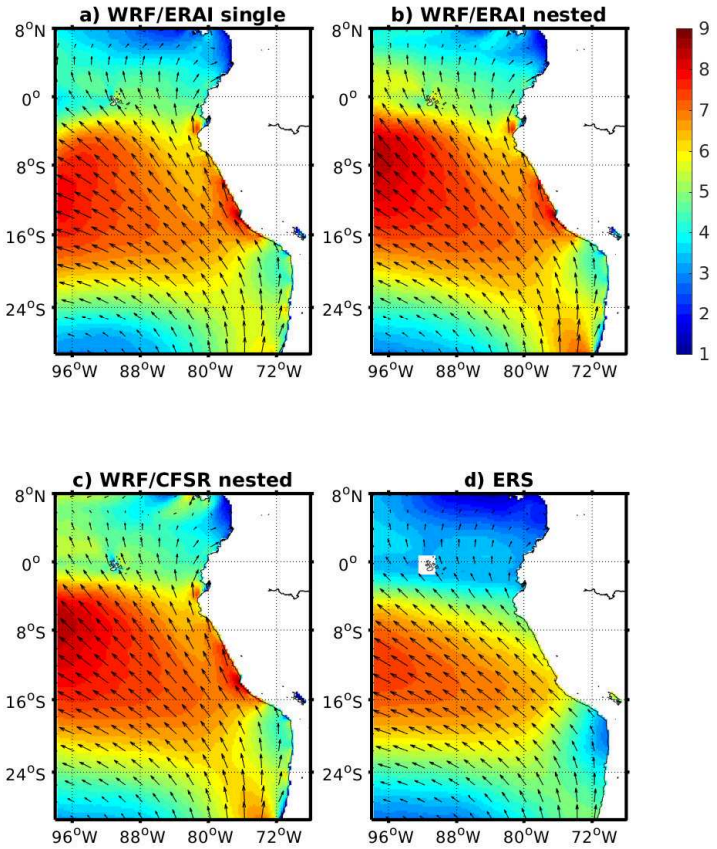

Fig. 2.13 *Mean surface wind speed (in* $\mathrm{m\,s^{-1}}$*)) and direction (arrows) for the period 1997-1998 from WRF simulations with three different configurations: a) Single domain forced with ERA-Interim data, b) Nested domain forced with ERA-Interim data, and c) Nested domain forced with CFSR data.*

a) Computing the turbulence shear stress

In the PBL scheme used in our simulations (i.e MYNN), momemtum mixing is parameterized by a Reynolds turbulent stress ($\vec{\tau}$), which is defined as:

$$\vec{\tau} = \rho K_M \frac{\partial \vec{\nu}}{\partial z}$$

with ρ the air density, K_M the momentum vertical diffusion coefficient, and $\frac{\partial \vec{\nu}}{\partial z}$ the vertical shear of horizontal velocity.

It is not calculated by default by the WRF model. For this reason, functions of the MYNN PBL scheme were modified to record the values of the momentum vertical diffusion coefficient (K_M). Then, the $\vec{\tau}$ term was calculated and recorded in the WRF outputs.

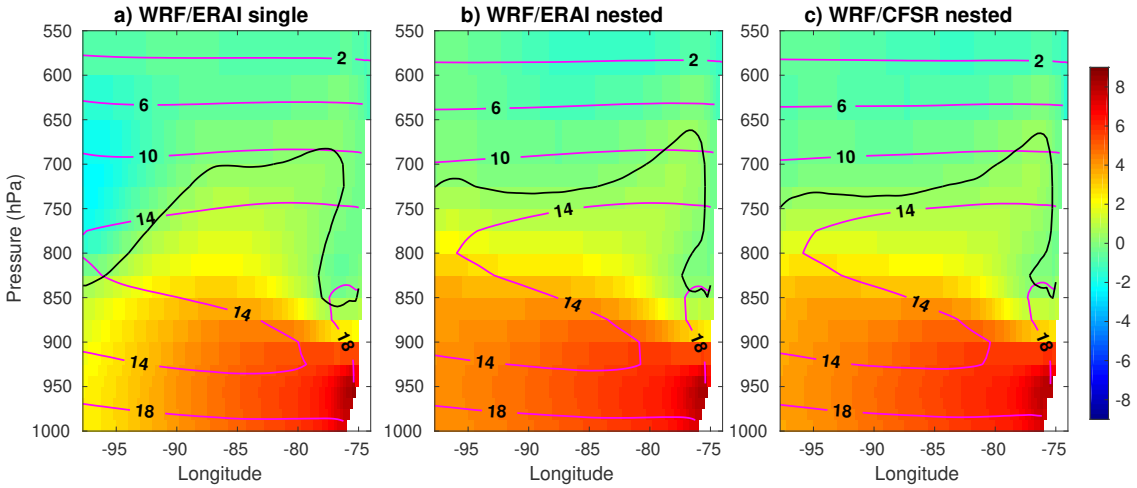

Fig. 2.14 *Cross-shore vertical sections at* 15 °S *of the mean meridional wind (shading, in* $\mathrm{m\,s^{-1}}$*) and air temperature (magenta contours, in* °C*) from three WRF simulations with different configurations (same as Fig. 2.13).*

b) Extracting horizontal momentum tendency terms

Wind horizontal velocity time variations are driven by the following momemtum balance:

$$\frac{\partial \vec{\nu}}{\partial t} = \left(\vec{\nu}\cdot\vec{\nabla}\right)\vec{\nu} + \frac{\partial}{\partial z}\left(\frac{\vec{\tau}}{\rho}\right) - f\hat{k}\times\vec{\nu} - \frac{1}{\rho}\vec{\nabla}P \tag{2.8}$$

with f the Coriolis parameter, P the pressure and $\hat{k}$ the vertical unitary vector. The right-hand terms of equation represent the wind advection, the effect of turbulent vertical mixing of momentum, the Coriolis and the pressure gradient forces, respectively.

The standard WRF configuration only allows the user to record the output of total zonal and meridional components of horizontal momentum tendency (first term in equation (2.8)), which are recorded over each user-defined large time step. However, additional variables had to be introduced within the dynamical solver to record the output of the others momentum terms (the right-hand terms of equation (2.8)) to make them available for history output.

c) Recording the mean cumulative

A simple time average of the momentum equation (2.8) relates the forcing time average to the difference between the final and initial wind but not to the average wind $\langle V\rangle$. They showed that $\langle V\rangle$ is related to the momentum terms by the following formula:

$$\frac{\langle V\rangle - V(t_o)}{\Delta t} = \sum_{F_n\in forces}[F_n]$$

where $V(t_o)$ is the initial velocity at the beginning of the time interval, Δt the time step, and F_n the momentum terms. The bracket ([]) is the double time averaging operator defined as:

$$[F_n] = \frac{1}{N+1}\sum_{p=0}^{N}(\sum_{k=1}^{p} F_n)$$

with N the number of time steps during the time interval.

For this reason, the WRF code was modified to record the double time average of each momentum terms at each model time step, following Oerder et al. (2016).

2.3.4 Model run optimization

The simulations were mainly performed on the supercomputer Curie from the GENCI at the CEA (projects x2014011140, x2015011140 and x2016011140) in France and some of them on the cluster of the Institute of the Sea of Peru (IMARPE). Curie machine has 10080 eight-core processors, Intel® Xeon® Next Generation (2.7 GHz), total of 80640 cores, for MPI parallel codes. The IMARPE cluster has 12 BLADE DELL servers (Xeon E5-2680v3 2.5GHz), total of 288 Cores. Both of them use the Linux operating system.

The WRF model was built to run on both machines utilizing MPI Intel compilers version 14. After doing tests, we chose 200 processors to execute the WRF model, which guarantees optimal use of the computational resources (see graph 2.15). Each year of simulation requires aproximately 6000 hours of time computing.

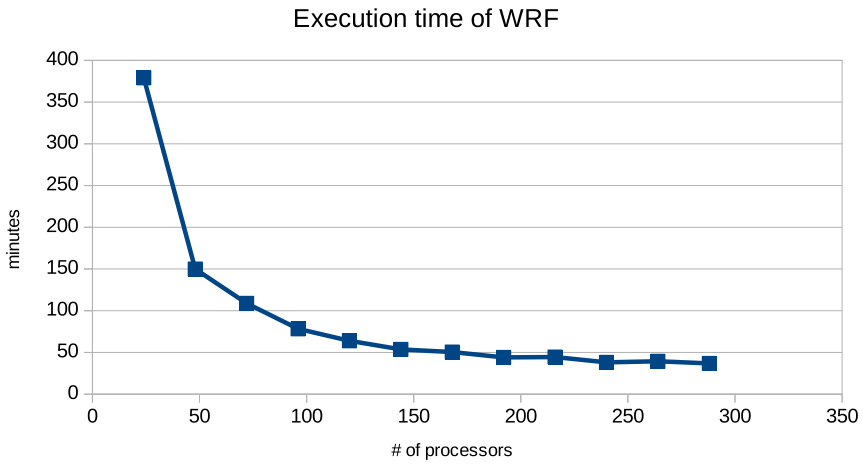

Fig. 2.15 *Execution time of the WRF model (1 month of simulation) when varying the number of CPU cores on the IMARPE cluster.*

Chapter 3

Coastal winds dynamics during El Niño events

3.1 Introduction

The Peruvian upwelling system is strongly impacted by El Niño events (see chapter 1). During the so-called "canonical" El Niño events, there is an apparent contradiction between the coastal SST warm anomalies and the coastal wind intensification off the Peru coast (Kessler, 2006). The purpose of this chapter is to study this apparent paradox, using the WRF regional atmospheric model to simulate the surface winds response to El Niño SST anomalies. The specific aims are:

- to study the physical mechanisms responsible for the intensification of alongshore coastal winds in the Peruvian upwelling system during the 1997-1998 El Niño event by analysing the momentum budget of the atmospheric boundary layer.
- to study the roles of the large scale signal and SST local forcing on the alongshore wind anomalies in order to disentangle the main drivers of wind intensification during the 1997-1998 event.

The interpretation is extended to other El Niño conditions during the 1979-2016 period using data from Reanalysis.

3.2 Summary

The WRF regional atmospheric model was used to study the physical processes driving the wind intensification off the Peru coast during the intense 1997-1998 El Niño event. As anomalously warm waters accumulated near the coast, the equatorward coastal wind increased by $\sim$1–1.5 $\mathrm{m\,s^{-1}}$ during 5-6 months (up to $\sim$40 % increase with respect to the climatological mean over the 1994-2000 period) as observed by the ERS satellite.

A simulation performed for the period 1994-2000 reproduced the coastal wind response to local sea surface temperature (SST) forcing and large scale atmospheric conditions during El Niño 1997-1998. The model, evaluated against satellite data, represented well the intensity, seasonal and interannual variability of alongshore winds. However, the wind

decrease towards the coast (the so-called wind drop-off; Capet et al. (2004)) was poorly simulated, especially between 10–16 °S.

A momentum balance analysis showed that the coastal wind intensification was mainly driven by the enhancement of the alongshore pressure gradient. Vertical mixing tended to counterbalance the alongshore pressure gradient, leading to a quasi-equilibrium between the alongshore pressure gradient and the frictional force. Moreover, a quasi-linear relation between surface wind and pressure gradient anomalies was found. Our results are consistent with previous modeling studies in the region (Muñoz and Garreaud, 2005; Belmadani et al., 2014).

The enhancement of the alongshore pressure gradient occured because the atmospheric pressure decreased more north (∼6 °S) than south (14 °S), in association with the larger increase of SST, air temperature and humidity off northern Peru (i.e associated with the inhomogeneous warming along the coast during El Niño event).

Surface warming induced an increase of the height of the PBL of up to two and a half times and of the vertical turbulent mixing coefficient ($K_z = \tau/(\partial V/\partial z)$) of up to three times their values in mean climatological conditions. However vertical mixing of momentum ($\partial\tau/\partial z$) remained negative and was stronger (in absolute value) during El Niño than in mean climatological conditions. Thus, vertical profiles of wind, mixing coefficient, and momentum trends showed that the surface wind intensification was not caused by the increase of turbulence in the planetary boundary layer. Moreover, the temperature inversion in the vertical mitigated the development of pressure gradient due to air convection during part of the event. We concluded that it is likely that two conditions, a SST anomaly alongshore gradient and a weak (or absent) temperature vertical inversion, would be necessary to drive a strong wind anomaly in the coastal region. The SST gradient drives the pressure gradient, and the weak temperature inversion allows shallow convection to develop without activate any "back-pressure effect" (a mechanism compensating the surface pressure gradient; Hashizume et al. (2002)).

In addition, two sensitivity experiments were done to isolate the respective impacts of the large scale atmospheric signal (called BRY-EN experiment, forced by 1997-1998 El Niño boundary conditions and neutral SST forcing from the years 1994-1995) and of the SST local forcing (called SST-EN experiment, forced by El Niño SST forcing and 1994-1995 neutral boundary conditions) on the coastal wind intensification. Analysis of simulations show that the wind intensification was primarily driven by the local SST forcing whereas large scale variability associated with the South Pacific Anticyclone modulated its effects.

Due to the model computational cost, the simulations were performed for a relatively short time period (1994-2000) including only one El Niño event. In order to evaluate if the same dynamical processes were active during other El Niño events, we performed similar diagnostics using the ERA-Interim reanalysis data of 0.75° (∼80 km) over the period 1979-2016. They confirmed that intensifications of alongshore wind off Peru were associated with SST alongshore gradient anomalies, as during the 1997-1998 event.

3.3 Article published in *Climate Dynamics*

Our results are detailed in the following article.

Reference: Chamorro A, Echevin V, Colas F, Oerder V. Tam J, Quispe-Ccalluari C (2018) Mechanisms of the intensification of the upwelling-favorable winds during El Niño 1997–1998 in the Peruvian upwelling system. Climate Dynamics 1-17. https://doi.org/10.1007/s00382-018-4106-6

Mechanisms of the intensification of the upwelling-favorable winds during El Niño 1997-1998 in the Peruvian Upwelling System

Adolfo Chamorro (1,2), Vincent Echevin (2), Francois Colas (2), Vera Oerder (2,3), Jorge Tam (1), Carlos Quispe-Ccalluari (1)

email: achamorro@imarpe.gob.pe

(1) Instituto del Mar del Perú (IMARPE), Callao, Perú
(2) LOCEAN-IPSL, IRD/CNRS/MNHN/UPMC, UMR7159, Paris, France
(3) Instituto Milenio de Oceanografía (IMO-Chile), Universidad de Concepción, Concepción, Chile

Abstract. The physical processes driving the coastal wind intensification off the Peru coast during the intense 1997-1998 El Niño (EN) event were studied using a regional atmospheric model. A simulation performed for the period 1994-2000 reproduced the coastal wind response to local sea surface temperature (SST) forcing and large scale atmospheric conditions. Simulated winds, evaluated with satellite data, captured well the wind intensity, alongshore and intraseasonal variability. An alongshore momentum budget showed that the pressure gradient was the dominant force driving the surface wind acceleration. The pressure gradient tended to accelerate the coastal wind, while turbulent vertical mixing decelerated it. A quasi-linear relation between surface wind and pressure gradient anomalies was found. Alongshore pressure gradient anomalies were caused by a greater increase in near-surface air temperature off the northern coast than off the southern coast, associated to the inhomogeneous SST warming. Vertical profiles of wind, mixing coefficient, and momentum trends showed that the surface wind intensification was not caused by the increase of turbulence in the planetary boundary layer. Moreover, the temperature inversion in the vertical mitigated the development of pressure gradient due to air convection during part of the event. Sensitivity experiments

allowed to isolate the respective impacts of the local SST forcing and large scale condition on the coastal wind intensification. It was primarily driven by the local SST forcing whereas large scale variability associated with the South Pacific Anticyclone modulated its effects. Examination of other EN events using reanalysis data confirmed that intensifications of alongshore wind off Peru were associated with SST alongshore gradient anomalies, as during the 1997-1998 event.

Keywords

Ocean-atmosphere interactions; Coastal winds; El Niño 1997/1998; Peruvian Upwelling System

1. Introduction

The Peruvian Upwelling System is one of the major upwelling systems of the world in terms of fisheries (Zuta and Guillen 1970; Chavez et al. 2008). A key oceanic process in this nearshore marine environment is the upwelling of deep, nutrient-replete, cold water to the surface forced by Ekman divergence associated to predominantly equatorward coastal winds. As in other upwelling regions, it is characterized by an intense biological productivity (Chavez & Messié, 2009) and strong air-sea interactions (e.g. Halpern, 2002; Small et al., 2008; Boé et al., 2011; Oerder et al., 2016). A unique aspect of the Peruvian system is its proximity to the equator in the Eastern Pacific, which places it directly under the influence of El Niño events (EN hereafter). During so-called “canonical” EN events, warm surface waters accumulate in the Eastern Tropical Pacific off the Ecuador and Peru coasts (*e.g.* Picaut et al., 2002) causing a dramatic reduction of the upwelling of cold water (*e.g.* Colas et al. 2008). The upwelling reduction is somewhat mitigated by an increase of the equatorward coastal wind (Wyrtki, 1975; Kessler, 2006). This local wind increase is seemingly paradoxical since large-scale trade winds are weakened in the equatorial (Bjerknes, 1966) and subtropical (Rahn et al., 2012) regions. Figure 1a shows that mean spatial distribution of the wind anomalies off Peru coast during the strongest El Niño event observed to date, between November 1997 and February 1998. Positive wind

anomalies were maximum along the Peru coasts and decreased offshore. Negative wind anomalies at the equator indicate the weakening of the southerly trade winds in the equatorial Pacific. The strongest alongshore positive wind anomalies reached ~1.5 m s^{-1} during November 1997-February 1998 which represents a ~40 % increase with respect to the climatological mean (Figure 1b).

The processes that drive the nearshore wind increase during EN have not been studied in detail. Previous studies suggested that the wind intensification could be driven by a strengthening of the cross-shore pressure gradient (supporting a geostrophic wind) owing to an enhanced cross-shore thermal contrast between land and sea (Bakun, 1990; Bakun et al., 2010). This enhanced thermal contrast would be caused by a stronger temperature increase over land than over sea during EN, due to the greenhouse effect induced by moist air. On the other hand, Enfield (1981) suggested that the enhanced cross-shore thermal contrast during EN was forced by a stronger shortwave heating over land associated to a reduction of nearshore cloudiness. Other studies suggested that the wind intensification may be driven by the strengthening of the alongshore pressure gradient associated with the alongshore SST gradient which appears off the Peru coasts during EN (Kessler, 2006), but no demonstration was made. In addition, the enhanced atmospheric turbulence due to the surface ocean warming may result in the downward vertical mixing of momentum from the upper layers of the atmosphere to the ocean surface, thus increasing the surface wind (*e.g.* Wallace et al., 1989).

Large scale atmospheric circulation is also impacted by EN, which may affect coastal winds through modifications of the South Pacific Anticyclone (SPA). Dewitte et al. (2011) showed that the alongshore wind intraseasonal (*i.e.* 10-60 days band) variability off central Peru (~15°S) was forced by migratory disturbances across the SPA. Rahn et al. (2012) showed that the SPA was weaker during EN, resulting in decreasing winds off central Chile. Such weakening might mitigate the coastal wind increase during EN off Peru, and a poleward displacement of the SPA might have a similar effect, as shown by

Belmadani et al. (2014) in the context of climate change. However, the influence of large-scale atmospheric circulation interannual variability on the coastal winds off Peru remains to be extensively investigated.

In this paper, a regional atmospheric model forced by realistic oceanic (i.e. Sea Surface Temperature) and lateral boundary conditions was used to investigate the physical processes driving the coastal wind intensification during the strong 1997-1998, “eastern pacific” El Niño event. The respective roles of the large scale signal and SST local forcing on the alongshore wind anomalies were also studied for this particular event. Data and methods are described in section 2. Results are presented in section 3, and discussion and conclusions are given in section 4.

2. Data and Methods

2.1 Regional atmospheric model

The Weather Research and Forecasting (WRF) model version 3.3.1 (Skamarock and Klemp 2008) was used to simulate the coastal wind during the period 1994-2000, which includes the very strong 1997-1998 El Niño event (McPhaden, 1999). WRF is a fully compressible and nonhydrostatic model. Its vertical coordinate is a terrain-following hydrostatic pressure coordinate. The model uses a Runge-Kutta 3rd order time integration scheme, and 5th order upwind biased advection schemes in space. Two nested domains, with one-way offline nesting, were used (Fig.2). The large domain has a resolution of 0.75° and encompasses the South East Pacific and the main part of South America. The small domain has a resolution of 0.25° and covers the Peru and Northern Chile region (30°S-12°N). Both domains include the Andes. The relatively high resolution of the nested domain allows to better represent the orography (Fig. 2), a crucial element of the regional dynamics (e.g. Xue et al. 2004). Both grids have 60 vertical sigma levels between the surface and the top of the atmosphere (defined by the 50 hPa top pressure), with 21 levels in the first ~1000 m. The time steps for the large and nested domains are 180 s and 60 s, respectively.

The parameterizations for short and long wave radiation, cloud physics, land surface and planetary boundary layer (PBL) used in this study are listed in Table 1. Most of them (except the Dudhia (1989) shortwave radiation scheme) are identical to those in the 1/12° configuration of Oerder et al. (2016) for the Peru-northern Chile region.

Data from the ERA-interim reanalysis (Dee et al. 2011) were used as initial and boundary conditions. The daily Optimum Interpolation Sea Surface Temperature (OISST) at 0.25° (Reynolds et al. 2007) was used as SST forcing. WRF outputs were recorded every 6 hours using instantaneous and average values.

2.2 Observational data

Observations from two different satellite-borne scatterometers were used to evaluate the realism of the model surface winds: the ERS weekly wind fields at 1°x1° resolution over the period 1992-2000 and a monthly climatology of QuikSCAT wind fields (hereafter QSCAT) at 1/2°x1/2° resolution grids. The two products were processed by CERSAT (2002a,b) and downloaded from www.ifremer.fr/cersat. Surface winds were interpolated on the 1/4° model grid.

Daily SST and output from ERA-interim reanalysis (see above) were also used in the analysis.

2.3 Monthly momentum budget

In order to investigate the dominant forces that induce the monthly wind changes, we used the following relation demonstrated in Madec (2008; for the NEMO ocean model) and Oerder et al. (2016):

$$\frac{\langle V \rangle - V(0)}{\Delta t} = \sum_{F_n \in \text{ forces}} \left[F_n \right] \quad (1)$$

where <V> is the monthly mean wind, V(0) the initial state, Δt the time step, and F_n

the momentum terms: advection $(\vec{v}.\vec{\nabla})\vec{v}$, vertical mixing $\frac{\partial}{\partial z}\left(\frac{\vec{\tau}}{\rho}\right)$, Coriolis $-f\vec{k}x\vec{v}$ and pressure gradient $\frac{-1}{\rho}\vec{\nabla}P$. The bracket ($[]$) is a the double time averaging operator defined as:

$$[F_n]=\frac{1}{\mathrm{N+1}}\sum_{\mathrm{p=0}}^{N}\left(\sum_{\mathrm{k=1}}^{p}F_n\right) \qquad (2)$$

with N the number of time steps during one month.

Based on Eq. (1), we obtain the following relation:

$$\langle V\rangle_{\mathrm{M+1}}-\langle V\rangle_M=\sum_{\mathrm{Fn}\in\ \mathrm{forces}}\left(\Delta\mathrm{t}[F_n]_{\mathrm{M+1}}-\Delta\mathrm{t}[F_n]_M+\sum_t\Delta\,\mathrm{tF}_n\right) \qquad (3)$$

The left side of the equation represents the change of the monthly mean wind (from month M to month M+1) and the right side represents the sum of the forces contribution. We computed the anomalies of the alongshore (*i.e.* parallel to the WRF model smoothed coastline) component of Eq. (3) (with respect to the climatology over 1994-2000) in a coastal band of one degree width (4 grid points of the nested domain).

2.4 Virtual temperature

Virtual temperature is computed in order to estimate the relative contribution of humidity to air density and pressure during EN. The virtual temperature of moist air is the temperature that dry air should have to reach a total pressure and density equal to those of the moist air (Wallace and Hobbs, 2006). It is defined by:

$$T_v=\mathrm{T}*(1+0.61*Q_v) \qquad (4)$$

with T the air temperature and Q_v the mixing ratio, which describes humidity.

We computed the monthly virtual temperature anomaly as:

$$T_v'=(1+0.61*\overline{Q_v})*\mathrm{T}'+(\overline{T}*0.61)*Q_v' \qquad (5)$$

with primes marking the monthly anomalies and overlines marking the monthly means. The two terms on the right side of Eq. (5) represent the relative contribution of air

168 temperature and humidity anomalies to the virtual temperature anomaly. Given that
169 virtual temperature is directly proportional to the pressure (for a fixed mass of gas, at a
170 constant volume), these terms contribute to the atmospheric pressure.
171
172 **2.5 Model simulations**
173
174 We carried out three experiments with the WRF model. First, a control run was performed
175 over the 1994-2000 period. Then, two experiments (BRY-EN and SST-EN) were performed
176 to isolate the role of the large scale signal from the role of the SST local forcing. The BRY-
177 EN experiment was carried out using the 6-hourly atmospheric boundary conditions from
178 the years 1997-1998 (Niño boundary conditions) and daily SST forcing from the years
179 1994-1995 (so-called SST neutral conditions) to isolate the role of the large scale signal.
180 The SST-EN experiment was performed using the 6-hourly atmospheric boundary
181 conditions from the years 1994-1995 (normal boundary conditions) and daily SST forcing
182 from the years 1997-1998 (SST Niño conditions) to isolate the role of the SST local
183 forcing. Note that the 1994-1995 period is considered as “normal conditions” as it did not
184 present strong anomalies with respect to climatological conditions.
185
186 **3. Results**
187 **3.1 Validation**
188 3.1.1 Mean and annual cycle of the surface wind
189 The simulated surface winds were compared with ERS and QSCAT observations. Figures 3
190 a-c show the annual mean surface wind field obtained from both satellites and the model
191 for the year 2000, when the two satellite observation periods were overlapping. South of
192 the equatorial line, the observed surface winds were strong (~6-8 m s^{-1}) and they blowed
193 north-westward over the oceanic region. They were weaker and approximately parallel to
194 the coastline in the nearshore region, with a maximum (~5-6 m s^{-1}) near 15°S and
195 minimum (~3-4 m s^{-1}) near 18°S (Figs. 3a,c). The model reproduced the observed wind
196 spatial patterns, with a wind intensity closest to that of QSCAT. However, the wind drop-

197 off (*i.e.* wind decrease towards the coast, *e.g.* Capet et al., 2004) was poorly simulated,
198 especially between 10°S and 16°S. Note that wind speed was lower in ERS than QSCAT
199 by ~0.5 m s^{-1} over a large part of the model domain, but that the wind directions were
200 consistent. The differences in wind intensity between ERS and QSCAT are attributed to
201 the use of different operating frequencies, different temporal sampling of the satellites,
202 and gridded products with different spatial resolutions (Bentamy et al. 2013).
203
204 Figures 3 d-f show the climatological mean annual cycle of the alongshore wind near the
205 Peru coast. The seasonal cycles were computed over the same time period for ERS and
206 the model (1994-2000), but different time period for QSCAT (2000-2008). The observed
207 alongshore winds were strongest during austral winter (July-September) and early spring
208 (October) around 15°S. The model wind climatology was in relatively good agreement
209 with the satellite wind climalogies (with correlations > 0.85). It reproduced the local
210 maximun values (coastal jets) near 4°S and 15°S which are both seen in QSCAT but not in
211 ERS. ERS did not capture the local maximum at 4°S likely due to its lower spatial
212 resolution. The model overestimated the intensity of the alongshore wind with respect to
213 ERS and QSCAT between 3°S and 17°S, and slightly underestimated it with respect to
214 QSCAT in the equatorial region (0-2°S).
215
216 3.1.2 Wind and temperature cross-shore vertical structures
217 The meridional wind and temperature cross-shore vertical structures in the central Peru
218 (at ~15°S) simulated by the model were compared against the ERA-interim reanalysis
219 data (Figure 4). Reanalysis data showed the coastal jet core located a height of ~250 m
220 and within the first 100 km from the coast, with a wind intensity of ~8 m s^{-1} (Fig.4a). The
221 coastal jet is capped by a temperature inversion, which bottom is located at ~600 m
222 above sea level nearshore. The model reproduced relatively well the intensity of the
223 coastal jet core, although with a position much closer to the coast. In overall, the vertical
224 structures of wind and temperature were well reproduced by the model in the first ~1000
225 m. Note that the steep topography of the Andes is logically represented with greater

226 detail in the WRF model (Fig. 4b).

227

228 3.1.3 Surface winds and SST anomalies during El Niño

229 The model reproduced the spatial structure of the wind anomalies off Peru (north of
230 ~20°S) during November 1997-February 1998 (Fig. 5a) found in the satellite observations
231 (Fig. 1b). Persistent positive (equatorward) alongshore wind anomalies occured from April
232 1997 to October 1998 (Fig. 5b) in the 5°S-10°S latitude band. There was a short
233 relaxation period in August 1997 with weak negative anomalies south of 10°S. The
234 strongest positive anomalies (>1.5 m s^{-1}) occured between November 1997 and March
235 1998. Furthermore, strong negative anomalies (<-1 m s^{-1}) occured in December 1997 -
236 February 1998 north of 5°S. The general pattern of alongshore wind anomalies from the
237 model was consistent with that from ERS (Fig. 1b). However, some discrepancies were
238 found, such as an overestimation of modelled wind anomalies in May-June 1997 (a
239 nucleus of positive anomalies of ~1 m/s in WRF vs none in ERS) and an underestimation
240 in January 1997 (a nucleus with negatives anomalies of ~ -1 m/s in ERS vs none in WRF).
241 Strong SST positive anomalies (>3°C) were seen between May 1997 and May 1998 along
242 the equator in the Eastern Pacific and along the Peru coast (Fig. 5c), with two main peaks
243 (>4°C) between 5°S and 10°S in July-August 1997 and November 1997-April 1998 (Fig.
244 5d). These peaks were related to the poleward propagation of downwelling coastal-
245 trapped waves, which strongly deepened the thermocline during EN, shutting down the
246 upwelling of cold water (Colas et al., 2008). The amplitude of the SST anomalies slightly
247 reduced in September-October 1997 but remained quite strong (>3°C). Note that
248 although the two SST anomaly peaks were of a relatively similar amplitude, only the
249 second peak was synchronous with strong wind anomalies (> 1.5 m s^{-1}, Fig. 5a) during
250 November 97-April 98, whereas the wind response to the first peak in July-August 1997
251 was weaker (<1 m s^{-1} in the model and less than 0.5 m s^{-1} in ERS; Fig. 1b). Besides, the
252 model also reproduced the negative wind anomalies north of 5°S between November
253 1997 and April 1998, a period during which SST anomalies were positive.

254

3.2 Alongshore momentum budget

In order to investigate the forces that induced the wind anomalies off Peru coast during EN, we computed the anomalies of the forces involved in the meridional monthly momentum budget (Eq. 3) in the first layer of the model. Each term was averaged for the period November 1997-February 1998 (Fig. 6a-d).

Comparison of anomalies of advection, vertical shear of the meridional turbulent stress (hereafter named vertical mixing term), pressure gradient and Coriolis terms shows that pressure gradient and vertical mixing were the dominant forces (Figs. 6b,c). The pressure gradient anomaly was positive (Fig. 6c), thus accelerated the equatorward wind during EN. Expectedly, vertical mixing anomaly was opposed to the equatorward wind thus negative (Fig. 6b). The two terms almost balanced each other everywhere in the domain, except in the region between 0-5°S where advection anomaly was relatively strong (Fig. 6a) and pressure gradient and vertical mixing anomalies were much weaker. Coriolis term anomalies had much smaller values (Fig. 6d).

Figure 6e shows the time evolution of the monthly anomalies of the surface forces projected alongshore. The terms were averaged in a one-degree-wide coastal band between 7°S and 15°S (this coastal region was chosen because the coastline is relatively rectilinear and the wind anomalies were relatively homogeneous in space). The pressure gradient and vertical mixing were the main forces during the entire time period. The dates corresponding to pressure gradient maximum (positive anomalies) values coincided with those of vertical mixing minimum (negative anomalies) values (*e.g.* in June-July and November-December 1997 and April-May 1998). The advection term was weaker, except in July-September and October-November 1997. The contribution of the Coriolis force was negligible during the entire period. The tendency was almost equal to the sum of all terms (error was ~6% over the simulation period), showing that the budget (Eq. (3)) is virtually closed.

The wind acceleration during EN occurred during different phases (Fig. 6e, dashed-black line). It began in March 1997 ($\Delta V'$~1 m s^{-1} from March to April 1997) and was maintained until June 1997, due to a positive equatorward pressure force stronger than the sum of the other (negative) terms. The wind anomaly then strongly decreased (ΔV~-1.2 m s^{-1} from June to July 1997) due to a negative advection of momentum between June and August 1997, which was related to the large scale forcing. A similar momentum budget for the BRY-EN experiment confirmed this large scale modulation (figure not shown). The wind acceleration became strong again in September 1997 (ΔV~1.5 m s^{-1} from September to October), when advection weakened and the pressure gradient dominated the other forces. The tendency was weak from January to May 1998. In the later phase of EN, the wind anomaly was strongly reduced from May to July 1998, due to a decrease of the pressure gradient.

Consistently with previous studies (Muñoz and Garreaud, 2005; Belmadani et al., 2014), alongshore pressure gradient anomalies were highly correlated (0.8) with alongshore wind anomalies average over the coastal band (Fig. 6e), and along the coast between 4°S and 18°S (Fig. 7a). A strong correlation (around 0.75) between alongshore pressure gradient anomalies and alongshore wind anomalies was found for latitudes between 4°S and 18°S (Fig. 7b). In this sense, on average over a coastal band (7°S-15°S) ~64% of the temporal variability of the wind anomalies was explained by pressure gradient anomalies, suggesting that vertical mixing behaved like a linear bottom frictional term equilibrating the pressure gradient. This led to the following relation $V=\frac{-1}{c\rho}\frac{\partial P}{\partial y}$ with c the linear friction coefficient and ρ the surface air density. From our model results, c was ~ 4 10^{-5} s^{-1}, thus comparable to Muñoz and Garreaud (2005)'s estimation for the Chile central coast (c ~ 5 10^{-5} s^{-1}). The steep orography of the Andes precluded the development of an anomalous cross shore flow, thus the alongshore pressure gradient can not be equilibrated by the Coriolis force. Consequently the alongshore flow built up until the

311 frictional force (i.e. vertical mixing term) balanced the alongshore pressure gradient.

312

313 In summary, the pressure gradient term played a major role in initiating and terminating
314 the wind anomaly during this EN event. In the next sections we study in detail the
315 processes that drive the pressure gradient increase at the beginning of the event.

316

317 **3.3 Air temperature and humidity contributions to the alongshore pressure**
318 **gradient**

319 As surface pressure is related to virtual temperature in the air column (see Section 2.4),
320 we examined the relative contributions of temperature and humidity anomalies to the
321 virtual temperature anomalies (VTA) (see Eq.(5) in section 2.4) during EN (November
322 1997-February 1998). The VTA distribution displayed the largest positive anomalies (>4
323 °K) along the north coast between 4°S and 8°S and in the lowest 300 m (Fig. 8a).
324 Temperature variations dominated VTA (Fig. 8b), while humidity anomalies contributed to
325 at most ~15% of the VTA (north coast around 400 m, Fig.8c). The humidity anomaly was
326 stronger at 400 m because humidity was higher and nearly constant from the surface up
327 to ~400 m before decreasing progressively with altitude during EN, whereas it
328 progressively decreased with altitude with a relatively constant vertical gradient from the
329 surface to 900m under normal conditions (Fig. 8d). These results show that the stronger
330 temperature increase in the north of Peru was the main driver of the alongshore pressure
331 gradient anomaly during the EN event, while humidity did not play an important role.
332 This thermally driven pressure gradient was confirmed by the high correlation (0.84)
333 between the surface wind anomaly in the coastal band and the alongshore SST gradient
334 (Fig. 9). This correlation was slightly higher (0.87) with a 1 month lag (when the SST
335 gradient leads the wind). This suggests that the anomalously warm surface ocean forced
336 the low atmosphere by heating the air column more in the north than in the south, thus
337 generating the pressure gradient that drove the equatorward wind anomaly.

338

339

3.4 Downward mixing of momentum during EN

Due to the air warming and humidification associated with the presence of anomalously warm surface waters in the nearshore region, shallow convection was enhanced. In the coastal band, the planetary boundary layer height (PBLH) increased by ~200 m (~50%) around June 97 and by ~100-150m (~100%) between December 1997-March 1998 (Fig. 10). The PBLH increases were in phase with the SST anomalies peaks, and slightly stronger in the north than in the south, in agreement with the SST spatial changes (not shown).

Given this PBL variability, a potential mechanism for the wind intensification could be associated with the increase of turbulence in the PBL during EN, which may generate a more efficient downward vertical flux of momentum (Wallace et al., 1989). However, turbulent mixing tended to decelerate the wind even more during the warm EN phases (Fig. 6e). To further investigate why Wallace et al. (1989)'s mechanism can not explain the EN wind increase, we examined the vertical profiles of alongshore wind, turbulent vertical mixing coefficient, momentum budget forces contribution, and temperature during climatological and EN conditions in November 1997-February 1998 (Fig. 11). The wind intensification during EN occurred between the sea surface and ~1600 m (black line in Fig. 11a). The wind maximum (~8 m s^{-1}) shifted from ~300 m in normal conditions to ~500 m. There was a decrease of wind shear (dV/dz) below ~500m during EN, mainly due to the velocity increase at the surface (~20%) and a virtually unchanged velocity at 300 m (black line in Fig. 11a). Turbulent vertical mixing coefficient (K_z) increased almost twofold during EN reaching a maximum of ~40 $m^2.s^{-1}$ at 200 m (~15 m^2 s^{-1} in climatological conditions, blue line in Fig. 11a). The impact on the turbulent stress ($\tau=K_z.dV/dz$) of the wind shear decrease and turbulent vertical mixing (K_z) increase was such that the momentum vertical mixing term ($d\tau/dz$) reduced (*i.e.* more negative) during EN conditions (Fig. 6e; blue line in Fig. 11b). This also shows that the EN wind intensification near the surface was not driven by downward mixing of momentum. The pressure gradient (red line in Fig. 11b) increase was maximum at the surface and

decreased with height. The Coriolis and advection terms did not change much during EN (magenta and green lines on Fig. 11b). Note that the pressure gradient was strong at surface and in upper layers during EN. Air temperature decreased between the surface and 1600 m, showing no temperature inversion in this period (austral summer) in normal or EN conditions (Fig. 11c).

This time period is contrasted with the period July-August 1997, during which the surface wind anomalies were weak (Figs. 5a and 12a) in spite of SST anomalies of the same order (~4°C) as during November 1997-April 1998 (Fig. 5b). Between the surface and 800 m the wind reduced with respect to normal conditions, and did not change in the upper layers (800-1600m). The wind shear decreased between the surface and 400m (black line in Fig. 12a), mainly due to the velocity decrease between 300-400 m (~10%) and a virtually unchanged velocity at surface. Mixing coefficient (K_z) increased by almost 70% in this period, reaching a maximum of ~74 $m^2.s^{-1}$ at 250 m (~45 m^2 s^{-1} in climatological conditions at 220 m, blue line in Fig. 12a). The impact on the turbulent stress of wind shear and vertical mixing changes in this period was such that the momentum vertical mixing term did not change significantly (blue line in fig 12b). The wind decrease below ~600 m was likely driven by advection, which decreased below 500 m whereas the pressure gradient change remained positive. On the other hand, the pressure gradient vertical shear between the surface and ~600 m (Fig. 12b) was stronger than in November 1997-February 1998 period (Fig. 11b). Note also the well-marked temperature inversion in July-August 1997 (Fig. 12c). The effect of this particular vertical structure on the pressure gradient will be discussed below (Sect. 4.2).

3.5 Impacts of large scale atmospheric forcing and local SST forcing

In this subsection, we analyzed model sensitivity experiments to study the respective roles of the large scale signal and of the SST local forcing in driving the EN wind anomalies.

Figure 13a displays the alongshore surface wind anomalies (averaged in the coastal band

between 7°S and 15°S) for the CRTL, BRY-EN, SST-EN experiments. The large scale signal (BRY-EN simulation) during EN induced strong negative wind anomalies (~ -1 m s^{-1}) between March and September 1997, and moderate (<1 m s^{-1}) positive anomalies between October 1997 and March 1998. In contrast, the model forced by the 1997-98 SST forcing (SST-EN) simulated persistent positive wind anomalies between May 97 and August 97 (reaching ~1 m s^{-1} in August 97) and between November 1997 and May 1998 (peaking at ~1.5 m s^{-1} in January-February 98). There was a slightly negative anomaly in September 1997, which coincided with the slight decrease of SST anomaly in September-October 1997 (Fig. 5b). Note that the wind anomaly was negligible in CRTL in Jul-Aug 1997, in spite of a strong SST anomaly (~3-4 °C, Fig. 5b). This can be explained by the large scale signal, which forced a decrease of the equatorward wind (negative anomalies of ~ -1 m s^{-1} in July-September 1997 in BRY-EN) which compensated the wind increase (~ 0.5-1 m s^{-1} in SST-EN) forced by the anomalously warm SST.

In the first warm period (July-August 1997), the intensification of the wind driven by the SST forcing (SST-EN experiment) was compensated by the large scale signal (BRY-EN) not only at the surface but also as high as 1400 m (Fig. 13b). During the second period (November 1997-February 1998), boundary conditions (BRY-EN simulation) did not have a strong effect. The wind was modified very little in the vertical with respect to climatological conditions. The wind intensification below 200 m was fully forced by the anomalous SST (Fig. 13c).

Thus, the BRY-EN experiment showed that the large-scale atmospheric signal propagating into the Peru region through the open boundaries could mitigate (or enhance) the coastal wind anomalies during EN. The SPA center was located around its normal position into both periods (red lines in Figs 14 a,b). However, during March–September 1997, the SPA was weaker (-1-2 hPa anomaly) than in normal conditions (Fig.14a). This weakening should produce negative anomalies for the surface atmospheric pressure off Peru, which likely contributed to a decrease of the alongshore wind off Peru in the BRY-EN simulation.

Indeed, the maximum surface pressure in the SPA was well correlated (0.67) with BRY-EN wind anomalies during the EN period. In contrast with the March-September 1997 period, the SPA was slightly more intense in October 1997–March 1998 (Fig. 14b) and September 98 (not shown), favoring an intensification of the coastal wind during these time periods due to SST forcing (Fig.13a).

4. Discussion and conclusions

4.1 Summary

A regional atmospheric model was used to investigate the physical processes driving the wind intensification off the Peru coast during the 1997-1998 EN event. As anomalously warm waters accumulated near the coast, the equatorward coastal wind increased by ~1-1.5 m s^{-1} during 5-6 months (up to ~40 % increase with respect to the climatological mean over the 1994-2000 period). Simulated surface wind anomalies during EN were in good agreement with observed wind anomalies. A momentum balance analysis showed that the coastal wind intensification was mainly driven by the enhancement of the alongshore pressure gradient. Vertical mixing tended to counterbalance the alongshore pressure gradient, leading to a quasi-equilibrium between the alongshore pressure gradient and the frictional force, consistently with previous modeling studies in the region (Muñoz and Garreaud, 2005; Belmadani et al., 2013). The enhancement of the alongshore pressure gradient occured because the atmospheric pressure decreased more north (~6°S) than south (~14°S), in association with the larger increase of SST, air temperature and humidity off northern Peru. Surface warming induced an increase of the height of the PBL of up to two and half times and of the vertical turbulent mixing coefficient ($K_z=\tau/(dV/dz)$) of up to three times theirs values in normal conditions. However vertical mixing of momentum ($d\tau/dz$) remained negative and was stronger (in absolute value) during EN that in normal conditions, thus did not accelerate the equatorward wind.

4.2 The back-pressure effect during EN

The alongshore pressure gradient change was strong at surface and its vertical structure

varied during the EN period: the pressure gradient change was strong between the surface and ~1000m when there was no temperature inversion (*e.g.* in November 1997-February 1998; Figs. 11b,c). In contrast, it became negligible above 600m in the presence of a marked temperature inversion (*e.g.* in July-August 1997; Figs. 12b,c). Hashizume et al. (2002) showed that the so-called “back pressure effect”, a mechanism compensating the surface pressure gradients, was strong in the case of a marked temperature inversion above the PBL. Oerder et al. (2016) found that this effect reduced significantly the intensity of the surface pressure gradient above mesoscale SST positive anomalies in the Peru region. This is also likely the case in the Peru coastal region in our simulation during the period July-August 1997 (Fig. 12c). Note that temperature inversion is related to the strong atmospheric subsidence in the region led by the SPA (e.g. Haraguchi 1968).

In conclusion, it is likely that two conditions, a SST anomaly alongshore gradient and a weak (or absent) temperature vertical inversion would be necessary to drive a strong surface wind anomaly in the coastal region. The SST gradient drives the pressure gradient, and the weak temperature inversion allows shallow convection to develop without triggering any “back pressure effect”.

4.3 Land-sea thermal contrast

Bakun et al. (2010) suggested that the increase of humidity over coastal land during EN could enhance the local greenhouse heating effect, thus increasing land temperature more than SST. This thermal contrast would lead to the presence of lighter air over land than over sea, an intensification of the cross-shore pressure gradient and associated alongshore geostrophic wind. Similarly, Enfield (1981) suggested that a land-sea thermal contrast may occur due to an increase of downward solar radiation over land, which would be due to a reduction of cloudiness during EN. As Bakun et al. (2010) and Enfield (1981) suggested, humidity and incoming solar radiation increased over land during EN in our simulations (green and red lines respectively; Fig. 15). However, this increase in humidity and short wave radiation reaching the land surface did not support a strengthened land-sea thermal contrast. Indeed, the simulated land-sea contrast, which

485 was positive (*i.e.* air temperature was higher over land than over sea) in normal
486 conditions (not shown), decreased by ~100% during EN (blue line in Fig.15). Note that a
487 clear relation between land-sea thermal contrast and alongshore winds off Peru has not
488 been demonstrated in previous studies. Using a set of GCM simulations with a spatial
489 resolution of ~50 km in the Peru-Chile region, Belmadani et al. (2013) found that the
490 land-sea thermal contrast (dT/dx) increased off Peru in scenarios of climate change: at
491 8°S, dT/dx was ~4.5 10^{-2} K km^{-1} in preindustrial climate conditions, and reached ~6.5 10^{-2}
492 K km^{-1} in 4xCO2 climate conditions, thus increased by ~40% (see Figure 8c in Belmadani
493 et al., 2013). In spite of this strong increase, the alongshore wind decreased moderately
494 (~10%) off Peru. This reduction was driven by a decrease of the alongshore pressure
495 gradient associated to a poleward displacement of the SPA in a warmer climate
496 (Belmadani et al., 2013 and references herein). This and our results suggest that an
497 increase of the land-sea thermal gradient may not play a strong dynamical role for the
498 alongshore wind, at least for the range of horizontal resolution (~25 km in the present
499 study and ~50 km in Belmadani et al., 2013) explored in our model simulations. Note that
500 these resolutions do not allow to represent the coastal terrain located between the Andes
501 and the ocean with more than a few grid points.
502
503 **4.4 Dynamical processes during other EN events**
504 Due to the model computational cost, our simulations were performed for a relatively
505 short time period (1994-2000) including only one EN event. In order to evaluate if the
506 same dynamical processes were active during other events, we performed similar
507 diagnostics using the ERA-interim simulation over the period 1979-2016. This simulation
508 had a lower spatial resolution (~80 km) than our regional model, but it can give hints of
509 the processes at stake during EN events. The wind anomaly (in a coastal band of ~160
510 km and between 7°S and 15°S) for the 1997-98 EN was ~0.6-0.8 m s^{-1}, less than in our
511 model (~1.0-1.2 m s^{-1} for an average over 6 WRF grid points). We found relatively strong
512 wind anomalies during most EN events, in particular in 1982-83 (~0.8 m s^{-1}), 1987-88 (~1
513 m s^{-1}), 1992-93 (0.7 m s^{-1}), 2015-16 (0.8 m s^{-1}) (Fig. 16). In agreement with our analysis,

514 these four events were associated with positive alongshore SST gradient anomalies (*e.g.*
515 ~0.15 10^{-2} °C km^{-1} in 1982-83). There were also EN events with relatively weak wind
516 anomalies (i.e. 2002-2003). Note that strong SST gradient anomalies occurred during
517 relatively short time periods in 1993, 2002 and 2008, and were not associated with
518 positive wind anomalies. We may conjecture that other processes such as a
519 compensation by the large scale forcing through a modification of the SPA or the
520 presence of temperature inversion with a back pressure effect may be active during these
521 periods.
522
523 **4.5 Local air-sea coupled processes during EN**
524 Local air-sea coupled interactions not investigated in the present study may also play a
525 role during EN. First, the increase of humidity in the north of Peru leads to intense
526 precipitation on land and over the nearshore ocean (Takahashi, 2004), which may
527 enhance the ocean surface stratification. This may mitigate wind-driven oceanic vertical
528 mixing in the north and thus help maintaining the anomalous alongshore SST gradient
529 driving the coastal wind. On the other hand, the stronger coastal wind (Figs 1b and 5a),
530 SST (Fig.5b) and humidity (Fig.8c) anomalies in the north would increase evaporation and
531 thus cool the ocean more efficiently than further south. This effect may mitigate the SST
532 gradient and thus reduce the wind anomaly. Studying such feedbacks, which were not
533 taken into account in our forced atmospheric model framework, is beyond the scope of
534 the present study. These questions, which can be addressed using a regional high
535 resolution, ocean-atmosphere coupled model (*e.g.* Oerder at al. 2016), will be the purpose
536 of future studies.
537
538 5. **Acknowledgments**
539 This research is part of A. Chamorro's PhD thesis, funded by the fellowship from
540 CIENCIACTIVA/CONCYTEC-PERU at the University Pierre and Marie CURIE of France. It is
541 also part of the IDB project PE-G1001(Adaptation to Climate Change of the Fishery Sector
542 and Marine-Coastal Ecosystem), and it is a contribution to the cooperative agreement

543 between the Instituto del Mar del Peru (IMARPE) and the Institut de Recherche pour le
544 Developpement (IRD) and the LMI DISCOH. The simulations were performed on the
545 supercomputer Curie from the GENCI at the CEA (projects 2011040542, 2012061047 and
546 2014102286). Francois Pinsard is acknowledged for her help in the making of lateral
547 boundary forcing for the regional atmospheric model. Francis Codron and Clémentine
548 Junquas are acknowledged for useful discussions.

549

550 **6. References**

551 Bakun A, Field D, Renondo-Rodriguez A, Weeks SJ (2010) Greenhouse gas, upwelling
552 favourable winds, and the future of upwelling systems. Glob Chang Biol 16:1213-1228

553

554 Belmadani A, Echevin V, Codron F, Takahashi K, Junquas C (2014) What dynamics drive
555 future wind scenarios for coastal upwelling off Peru and Chile? Clim Dyn 43: 1893-1914.
556 doi:10.1007/s00382-013-2015-2

557

558 Bentamy A, Grodsky SA, Katsaros K, Mestas-Nuñez AM, Blanke B, Desbiolles F (2013)
559 Improvement in air-sea flux estimates derivedfrom satellite observations. Int J Remote
560 Sens 34(14):5243–5261. doi:10.1080/01431161.2013.787502

561

562 Bjerknes J (1966) Survey of El Niño 1957-58 in its relation to tropical Pacific meteorology.
563 Inter-American Tropical Tuna Commission Bulletin 12(2):, pp 1-62

564

565 Boé J, Hall A, Colas F, McWilliams JC, Qu X, Kurian J, Kapnick SB (2011) What shapes
566 mesoscale wind anomalies in coastal upwelling zones? Clim Dyn 36(11–12):2037–2049

567

568 Capet XJ, Marchesiello P., McWilliams JC (2004) Upwelling response to coastal wind
569 profiles. Geophys Res Lett 31, L13311. doi:10.1029/2004GL020123

570

571 Carr M-E., Strub PT, Thomas AC, Blanco JL (2002) Evolution of 1996 – 1999 La Nina and El

572 Nino conditions off the western coast of South America: A remote sensing perspective. J
573 Geophys Res 107(C12), 3236. doi:10.1029/2001JC001183
574
575 CERSAT (2002a) Mean wind fields (MWF product) user manual volume 1: ERS-1, ERS-2 &
576 NSCAT. Rep C2-MUT-W-05-IF. CERSAT-IFREMER, Brest
577
578 CERSAT (2002b) Mean wind fields (MWF product) user manual volume 1: QuikSCAT. Rep
579 C2-MUT-W-04-IF. CERSAT-IFR- EMER, Brest
580
581 Chavez FP, Bertrand A, Guevara-Carrasco R, Soler P, Csirke P (2008) The northern
582 Humboldt Current System: Brief history, present status and a view towards the future.
583 Prog Oceanogr 79(2–4):95-105. doi:10.1016/j.pocean.2008.10.012
584
585 Chavez FP, Messié M (2009) A comparison of eastern boundary upwelling ecosystems.
586 Prog Oceanogr 83(1):80-96.
587
588 Chen F, Dudhia J (2001) Coupling an advanced land surface hydrology model with the
589 penn state-NCAR MM5 modeling system. Part ii: Preliminary model validation. Mon
590 Weather Rev 129(4):587–604. doi:10.1175/1520-0493(2001)129<0587:CAA
591 LSH>2.0.CO;2
592
593 Colas F, Capet X, McWilliams JC, Shchepetkin A. (2008) 1997–98 El Niño off Peru: A
594 numerical study. Prog Oceanogr 79:138-155. doi:10.1016/j.pocean.2008.10.015.
595
596 Dee, D.P. et al (2011) The ERA-Interim reanalysis: configuration and performance of the
597 data assimilation system. Q J R Meteorol Soc A 137:553–597. doi:10.1002/qj.828
598
599 Dudhia J (1989) Numerical study of convection observed during the winter monsoon
600 experiment using a mesoscale two-dimensional model. J Atmos Sci 46:3077-3107.

doi:10.1175/1520-0469(1989)046<3077: NSOCOD>2.0.CO;2.

Enfield DB (1981) Thermally-driven wind variability in the planetary boundary layer above Lima, Peru. J Geophys Res 86(C3):2005-2016

Haraguchi PY (1968) Inversions over the tropical eastern Pacific ocean. Mon Weather Rev 96:177–185

Hashizume H, Xie SP, Fujiwara M, Tanimoto TWY (2002) Direct observations of atmospheric boundary layer response to SST variations associated with tropical instability waves over the Eastern Equatorial Pacific. J Clim 15:3379–3393. doi:10.1175/1520-0442(2002)015<3379:DOOABL>2.0.CO;2

Hong S, Lim J (2006) The WRF single-moment 6-class microphysics scheme (WSM6). J Korean Meteorol Soc 42(2):129–151

Janjic ZI (1994) The step-mountain eta coordinate model: further developments of the convection, viscous sublayer, and turbulence closure schemes. Mon Wea Rev 122:927–945. doi:10.1175/1520-0493(1994)122<0927:TSMECM>2.0.CO;2

Kessler WS (2006) The circulation of the eastern tropical Pacific: A review. Prog Oceanogr 69(2):181-217

Nakanishi M, Niino H (2009) Development of an improved turbulence closure model for the atmospheric boundary layer. J Meteorol Soc Jpn 87:895–912. doi:10.2151/jmsj.87.895

Madec G (2008) NEMO ocean engine. Note du Pole de modélisation,
Institut Pierre-Simon Laplace (IPSL) 27. ISSN No. 1288–1619.

McPhaden MJ (1999) Genesis and evolution of the 1997–98 El Niño. Science 283:950-954.

Mlawer E, Taubman S, Brown P, Iacono M, Clough S (1997) Radiative transfer for inhomogeneous atmosphere: RRTM, a validated correlated-k model for the long-wave. J Geophys Res 102:16,663–16,682. doi:10.1029/97JD00237

Muñoz RC, Garreaud RD (2005) Dynamics of the low-level jet off the west coast of subtropical South America. Mon Wea Rev 133:3661–3677. doi:10.1175/MWR3074.1

Oerder V, Colas F, Echevin V, Codron F, Tam J, Belmadani A (2015) Peru-Chile upwelling dynamics under climate change. J Geophys Res 120(2):1152-1172. doi: 10.1002/2014JC010299.

Penven P, Echevin V, Pasapera J, Colas F, Tam J (2005) Average circulation, seasonal cycle, and mesoscale dynamics of the Peru current system: Amodeling approach. J Geophys Res 110, C10021. doi:10.1029/2005JC002945

Picaut J, Hackert E, Busalacchi A, Murtugudde R , Lagerloef GSE (2002), Mechanisms of the 1997–1998 El Niño–La Niña, as inferred from space-based observations. J Geophys Res Oceans 107 (C5). doi: 10.1029/2001JC000850.

Rahn DA (2012) Influence of large scale oscillations on upwelling-favorable coastal wind off central Chile. J Geophys Res 117, D19114. doi:10.1029/2012JD018016

Renault L, Hall H, McWilliams JC(2015) Orographic shaping of USWest Coast wind profiles during the upwelling season. Clim Dynam 46:273–289. doi:10.1007/s00382-015-2583-4

Reynolds RW, Smith TM, Liu C, Chelton DB, Casey KS, Schlax MG (2007) Daily high-resolution-blended analyses for sea surface temperature. J Climate 20:5473-5496.

659 doi:10.1175/2007JCLI1824.1.
660
661 Skamarock W, Klemp J (2008) A time-split nonhydrostatic atmos- pheric model for
662 weather research and forecasting applications. J Comp Phys 227:3465–3485.
663 doi:10.1016/j.jcp.2007.01.037
664
665 Small, R. J., and Coauthors, 2008: Air–sea interaction over ocean fronts and eddies. Dyn.
666 Atmos. Oceans, 45, 274–319, doi:10.1016/j.dynatmoce.2008.01.001.
667
668 Strub PT, J Mesías, V Montecino, J Rutllant & S Salinas. 1998. Coastal ocean circulation off
669 Western South America. In: Robinson AR & KH Brink (eds). The global coastal ocean:
670 Regional studies and syntheses. The Sea 11: 273-314. John Wiley, New York.
671
672 Takahashi K (2004) The atmospheric circulation associated with extreme rainfall events in
673 Piura, Peru, during the 1997-1998 and 2002 El Niño events. Ann Geophys 22:3917-3926.
674 doi:10.5194/angeo-22-3917-2004
675
676 Takahashi K, Battisti DS (2007) Processes Controlling the Mean Tropical Pacific
677 Precipitation Pattern. Part I: The Andes and the Eastern Pacific ITCZ. Journal of Climate
678 20:3434-3451. doi: 10.1175/JCLI4198.1
679
680 Wallace JM, Hobbs PV (2006) Atmospheric Science: A Introductory Survey. 2nd ed.
681 Academic Press, pp 483
682
683 Wallace JM, Mitchell T, Deser C (1989) The influence of sea surface temperature on
684 surface wind in the Eastern Equatorial Pacific: seasonal and interannual variability. J Clim
685 2:1492–1499. doi:10.1175/1520-0442(1989)002<1492:TIOSST>2.0.CO;2
686
687 Wyrtki K (1975). El Niño: the dynamic response of the equatorial Pacific to atmospheric

forcing. Journal of Physical Oceanography 5:572–584

Xue H, Wang Y, Xie SP (2004) Effects of the andes on eastern pacific climate: a regional atmospheric model study. J Clim 17:587–602

Zuta S, Guillén O (1970) Oceanografía de las aguas costeras del Perú. Boletin Instituto del Mar del Perú 2: 157–324

7. Tables

Table 1. Parameterizations used in WRF model for the simulations.

Processes	Scheme	Reference
Shortwave Radiation	Dudhia scheme	Dudhia (1989)
Longwave Radiation	RRTM scheme	Mlawer et al. (1997)
Microphysics	WRF Single-Moment 6-class scheme	Hong and Lim (2006)
Cumulus	Betts-Miller-Janjic scheme	Janjic (1994)
Surface Layer	MYNN surface layer	Nakanishi and Niino (2009)
Land Surface	Noah Land Surface Model	Chen and Dudhia (2001)
Planetary Boundary Layer	MYNN Level 2.5 PBL	Nakanishi and Niino (2009)

8. Figure captions

Figure 1. a) ERS wind anomalies (in m s^{-1}) off Peru and Northern Chile during El Niño conditions in November-February 1997/1998. Arrows mark the direction of the monthly wind anomalies. b) Time-latitude diagram of ERS alongshore monthly wind anomalies off the Peru coast. The wind average was computed within a 100 km-wide coastal band and a 3-month running mean was applied. Positive values indicate equatorward wind anomalies.

Figure 2. South East Pacific model domain and Peru nested domain used in the WRF

710 simulations. Color shading indicates model topography (in meters) above sea level for the
711 small domain.
712
713 Figure 3. Mean surface wind (in m s^{-1}) in 2000 from a) ERS satellite, b) WRF model and c)
714 QSCAT satellite. Mean annual cycle of the alongshore wind (averaged in a 100-km-wide
715 coastal domain) from d) ERS and e) WRF over the period 1994-2000, and from f) QSCAT
716 over the period 2000-2008.
717
718 Figure 4. Vertical structure of the mean meridional wind (shading, in m s^{-1}) and air
719 temperature (black contours, in °C) at 15°S from a) ERA-Interim and b) WRF
720 model. Data was averaged for the 1994-2000 period.
721
722 Figure 5. a) Mean surface wind anomalies (in m s^{-1}) from WRF (over November 1997-
723 February 1998) and b) time-latitude diagram of WRF alongshore wind anomalies. c) Mean
724 sea surface temperature (SST) anomalies (in °C) from OISST (over the same time
725 period in a)) and d) time-latitude diagram of alongshore SST anomalies.
726
727 Figure 6. Anomalies of the meridional component of the surface forces contribution (in m
728 s^{-1}) during El Niño 1997/1998: a) advection (V-ADV'), b) vertical turbulent mixing (V-MIX'),
729 c) pressure gradient (V-PGF'), and d) Coriolis force (V-COR'). Anomalies were computed
730 with respect to a climatology over 1994-2000 and averaged over November 1997-
731 February 1998. e) Time series of the monthly anomalies (in m s^{-1}) of the alongshore
732 component of the surface forces in 1997-1998. The forces were averaged in a 100-km
733 coastal band between 7°S and 15°S,. Gray, black and black-dashed lines indicate
734 tendency, the sum of all terms and wind anomaly, respectively.
735
736 Figure 7. a) Alongshore anomalies of pressure gradient (in m s^{-1}, shading) and coastal
737 wind (in m s^{-1}, black contours) between the equator and 20°S. b) Latitudinal variation of
738 the correlation between alongshore pressure gradient anomalies and alongshore coastal

739 wind anomalies.

740

741 Figure 8. Alongshore vertical sections of the mean monthly anomalies (during November
742 1997-February 1998) of a) virtual temperature (in °C) and b) temperature and c) humidity
743 contributions (in °C) to the virtual temperature anomaly. Note the different scales for
744 temperature and humidity contribution. d) Vertical profiles of humidity in the northern
745 coastal region (4°S-8°S) during November 1997-January 1998 (full line) and normal
746 conditions (dashed line).

747

748 Figure 9: Time evolution of alongshore SST gradient (in °C/25km, positive equatorward,
749 red line) and wind (in m s^{-1}, black line) anomalies. Anomalies were smoothed using a 3-
750 month running mean, and averaged between 7°S and 15°S and within 100 km from the
751 coast.

752

753 Figure 10. Mean Planetary Boundary Layer Height (in meters, PBLH) off Peru. PBLH was
754 averaged between 7°S and 15°S and within 100 km from the coast. Red line marks PBLH
755 during 1997-1998, and black dashed line the climatology. Error bars indicate standard
756 deviation from the mean climatological values.

757

758 Figure 11. Vertical profiles of a) alongshore wind (in m s^{-1}), b) anomalies of alongshore
759 forces (in m s^{-1}) and c) air temperature (in °C). Averages were computed over
760 November 1997-February 1998, between 7°S and 15°S, and within 100 km from the
761 coast. Full and dashed lines correspond to El Niño and normal conditions, respectively.

762

763 Figure 12. Same as Figure 10 but for the period June-August 1997.

764

765 Figure 13: a) Time series of coastal alongshore wind anomalies (in m s^{-1}) from CRTL (black
766 line), SST-EN (red line), BRY-EN (blue line) experiments. Mean alongshore wind profiles (in
767 m s^{-1}) in b) July-August 1997 and c) November 1997-February 1998. Black-dashed, black,

768 red and blue lines mark the climatological (CLIM) ,CRTL, SST-EN and BRY-EN profiles,
769 respectively.
770
771 Figure 14. Mean (red contours) and anomalous (shading) sea level pressure (in hPa)
772 during a) March-September 1997 and b) October 1997–March 1998. White contours mark
773 pressure climatological values (1994-2000).
774
775 Figure 15. Anomalies of air humidity at 2 meters (in g kg^{-1}, green line), downward
776 shortwave radiation at sea surface (in W m^{-2}, red line) and land-sea air temperature
777 gradient at 2 meters (in 10^{-2} °C km, blue line). Anomalies of air humidity and shortwave
778 radiation were taken at the model land grid points closest to sea. Temperature gradient
779 was computed as the difference between the model land grid point closest to sea and the
780 sea grid point closest to land at each latitude. All variables were averaged between 7°S
781 and 15°S.
782
783 Figure 16. Time evolution of alongshore SST gradient (in °C/80 km, positive equatorward,
784 red line) and alongshore wind (in m s^{-1}, black line) anomalies for ERA-Interim reanalysis
785 over 1979-2016. Anomalies were averaged in a 160-km-wide coastal band and between
786 7°S and 15°S. Grey vertical bands indicate El Niño periods.

Figure 1

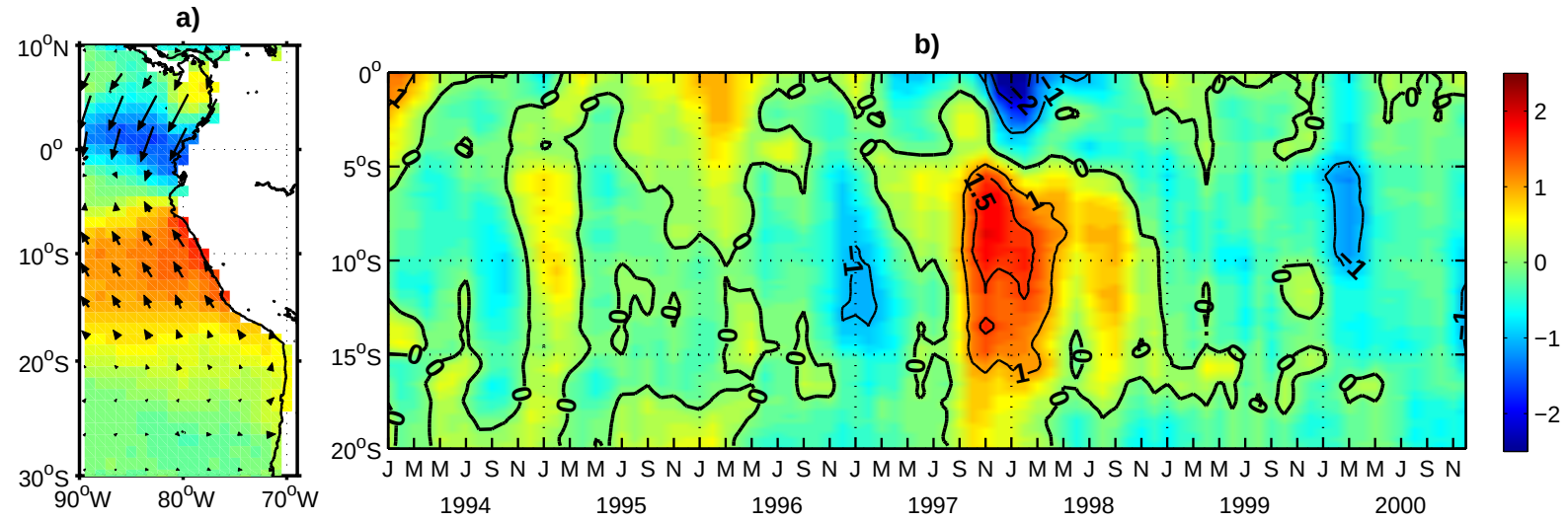
a)
10°N
0°
10°S
20°S
30°S
90°W
80°W
70°W
b)
0°
5°S
10°S
15°S
20°S
J M M J S N J M M J S N J M M J S N J M M J S N J M M J S N J M M J S N J M M J S N
1994
1995
1996
1997
1998
1999
2000
2
1
0
−1
−2

Figure 2

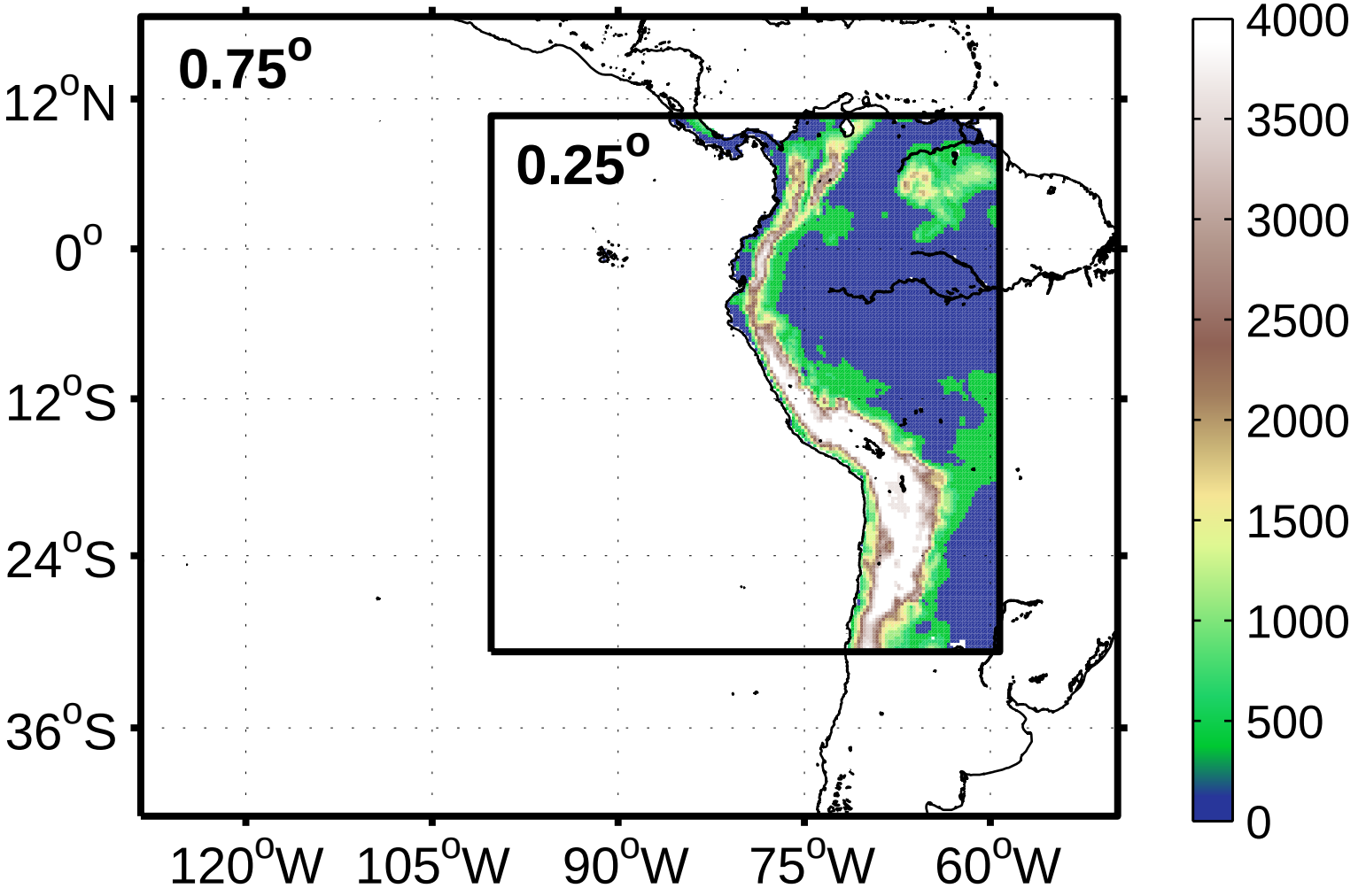
0.75°
0.25°
12°N
0°
12°S
24°S
36°S
120°W
105°W
90°W
75°W
60°W
4000
3500
3000
2500
2000
1500
1000
500
0

Figure 3

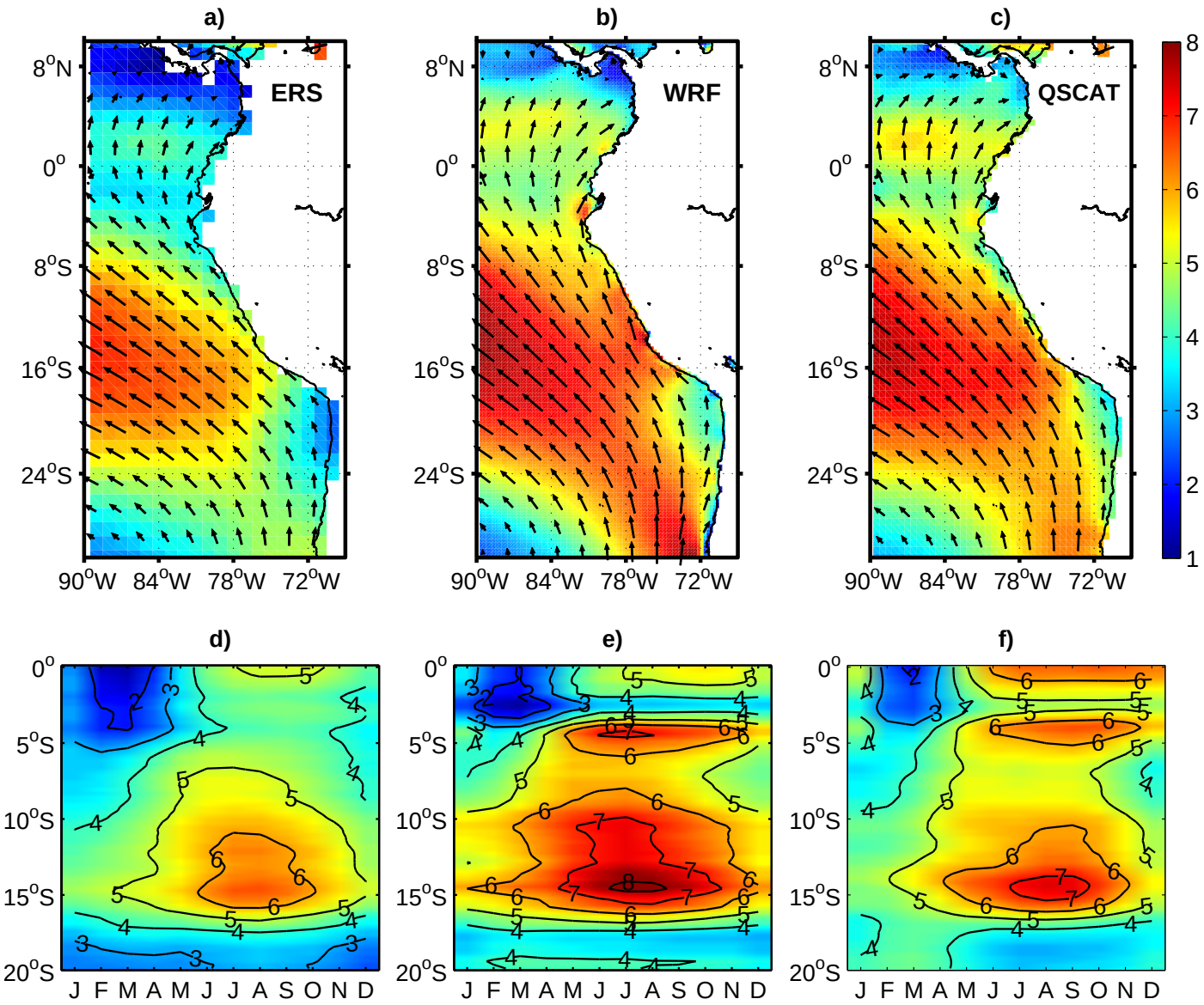
a)
b)
c)
ERS
WRF
QSCAT
8°N
0°
8°S
16°S
24°S
90°W 84°W 78°W 72°W
d)
e)
f)
0°
5°S
10°S
15°S
20°S
J F M A M J J A S O N D

Figure 4

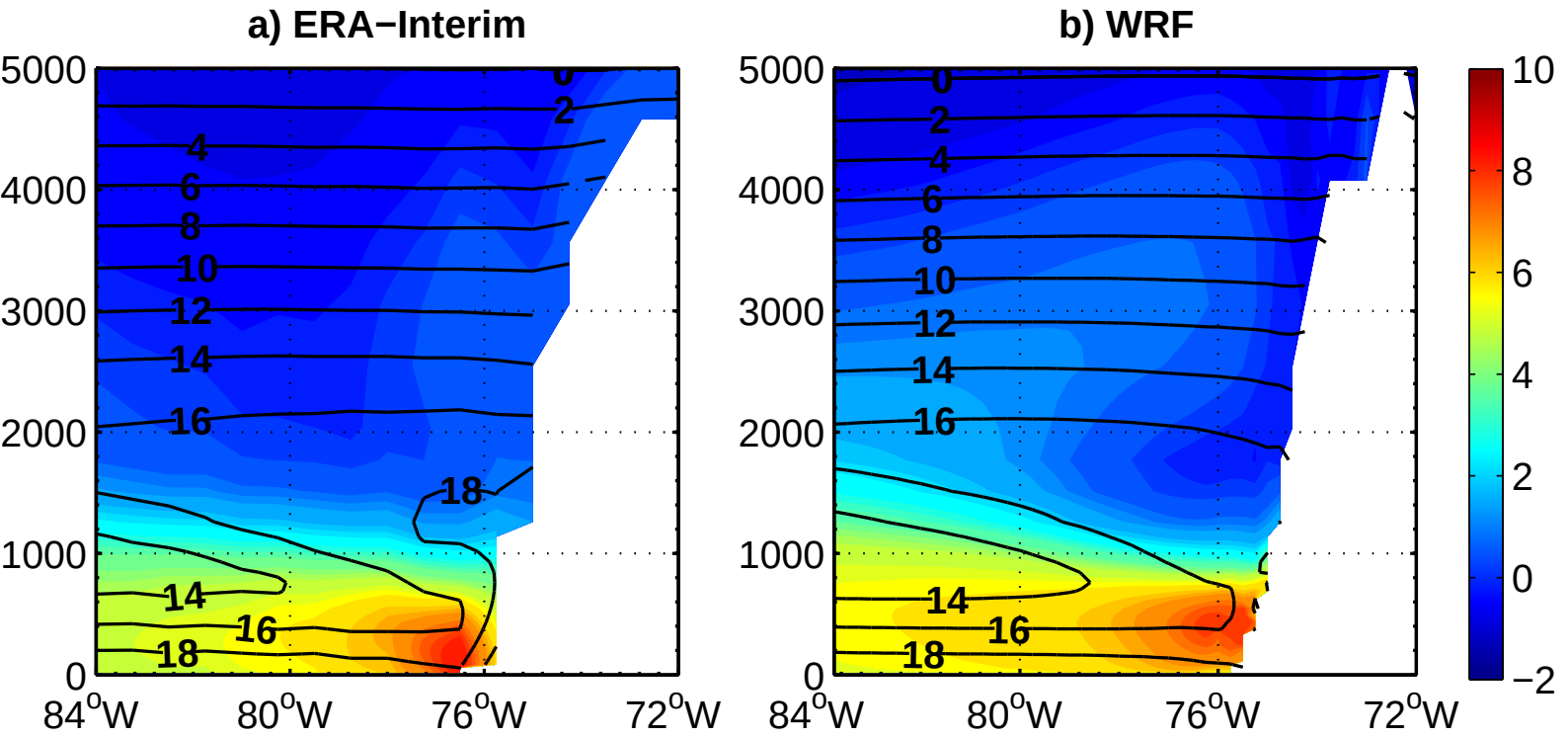
a) ERA−Interim
b) WRF
5000
4000
3000
2000
1000
0
84°W
80°W
76°W
72°W
0
2
4
6
8
10
12
14
16
18
10
8
6
4
2
0
−2

Figure 5

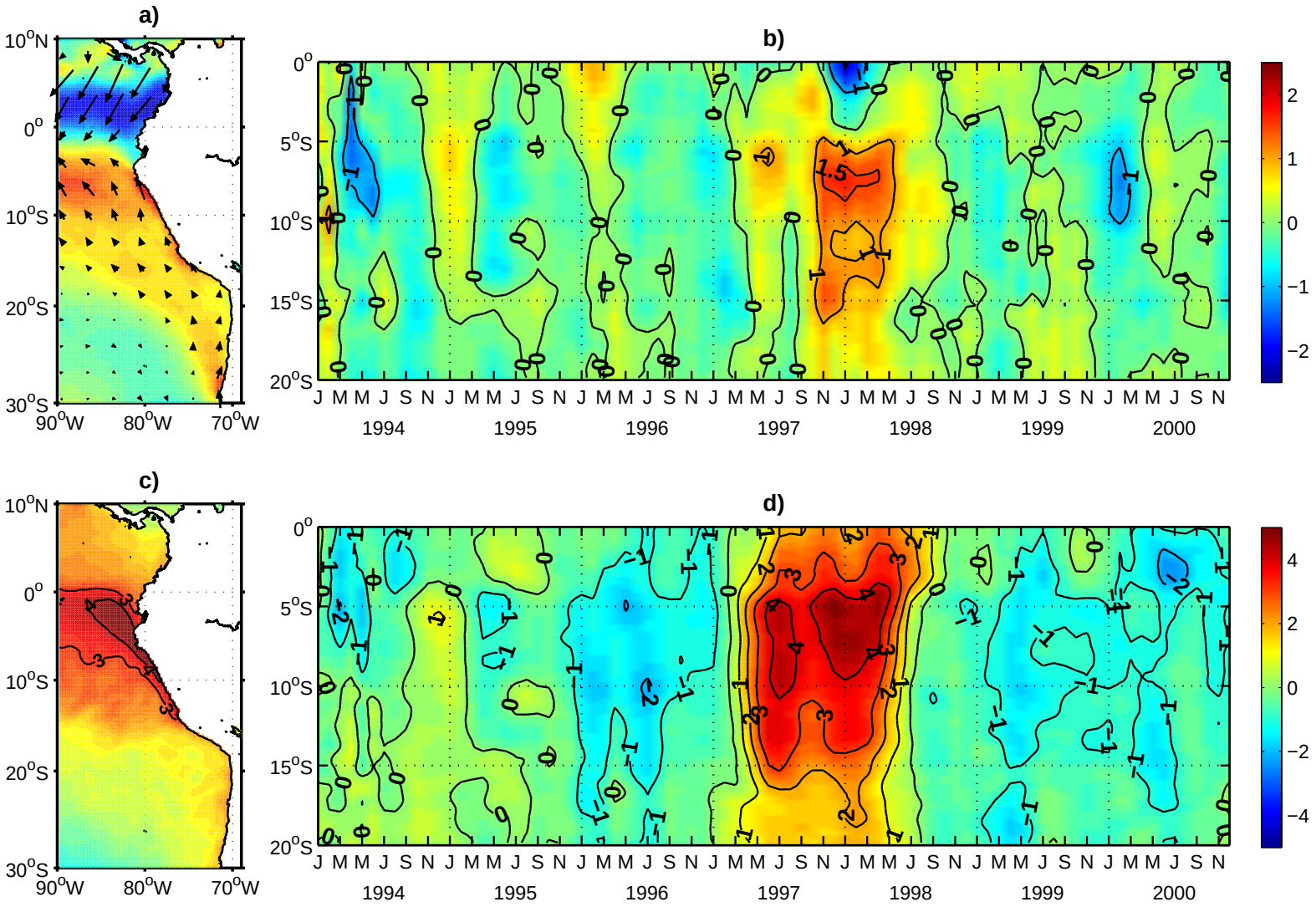
a)
b)
c)
d)
10°N
0°
10°S
20°S
30°S
90°W
80°W
70°W
0°
5°S
10°S
15°S
20°S
J M M J S N J M M J S N J M M J S N J M M J S N J M M J S N J M M J S N J
1994
1995
1996
1997
1998
1999
2000

Figure 6

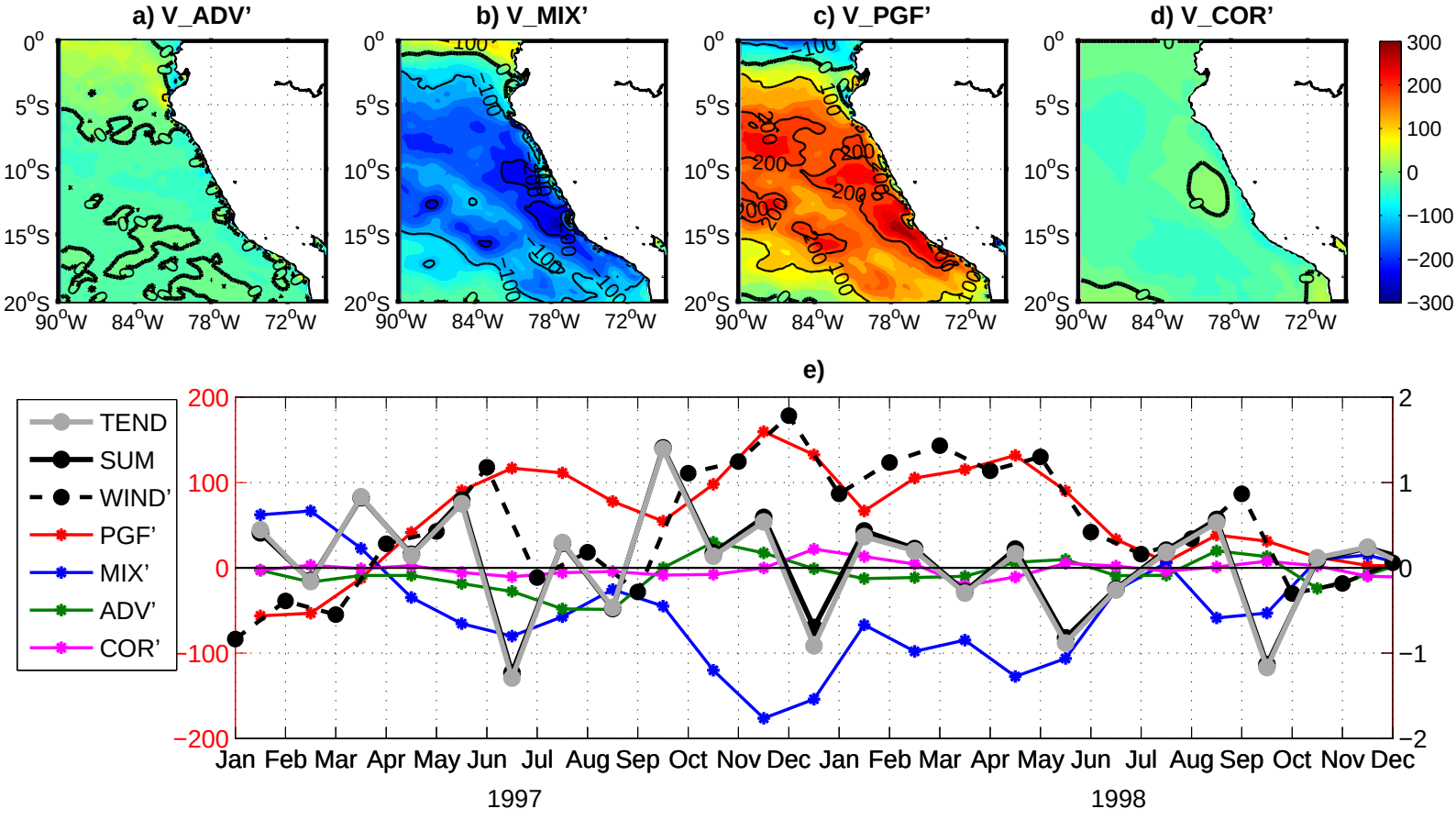
a) V_ADV'
b) V_MIX'
c) V_PGF'
d) V_COR'
0°
5°S
10°S
15°S
20°S
90°W
84°W
78°W
72°W
300
200
100
0
−100
−200
−300

e)
TEND
SUM
WIND'
PGF'
MIX'
ADV'
COR'
200
100
0
−100
−200
2
1
0
−1
−2
Jan Feb Mar Apr May Jun Jul Aug Sep Oct Nov Dec Jan Feb Mar Apr May Jun Jul Aug Sep Oct Nov Dec
1997
1998

Figure 7

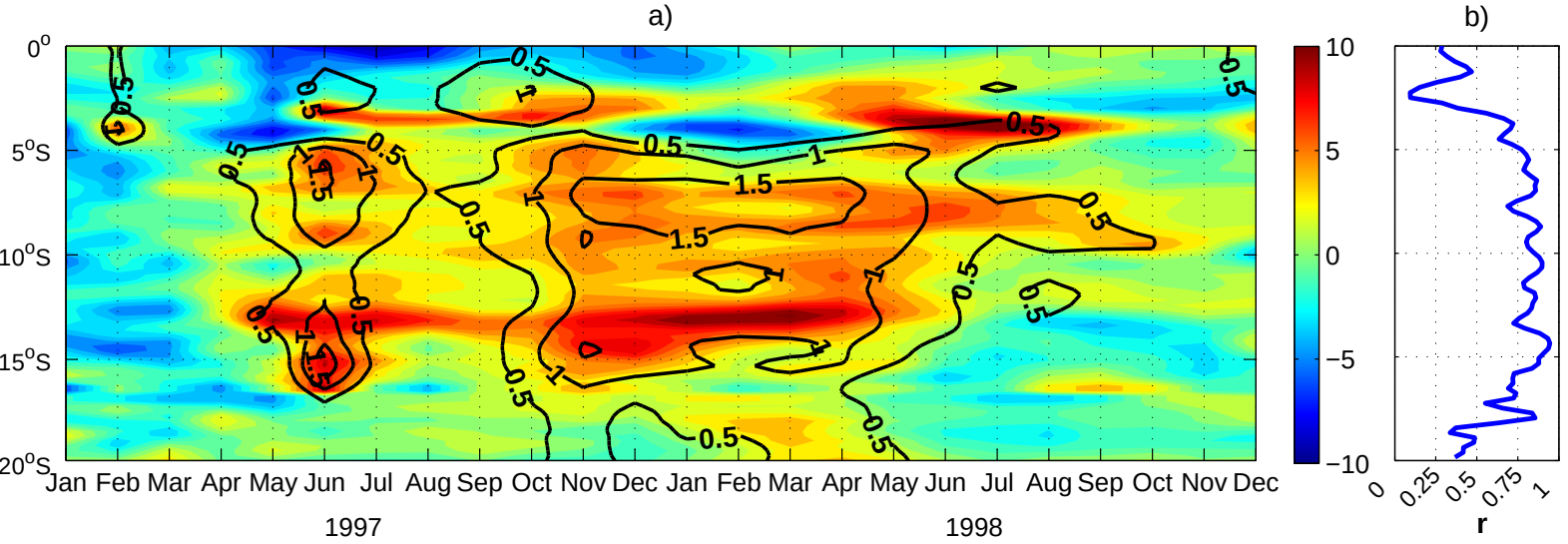
a)
b)
0°
5°S
10°S
15°S
20°S
Jan Feb Mar Apr May Jun Jul Aug Sep Oct Nov Dec Jan Feb Mar Apr May Jun Jul Aug Sep Oct Nov Dec
1997
1998
10
5
0
−5
−10
0
0.25
0.5
0.75
1
r

Figure 8

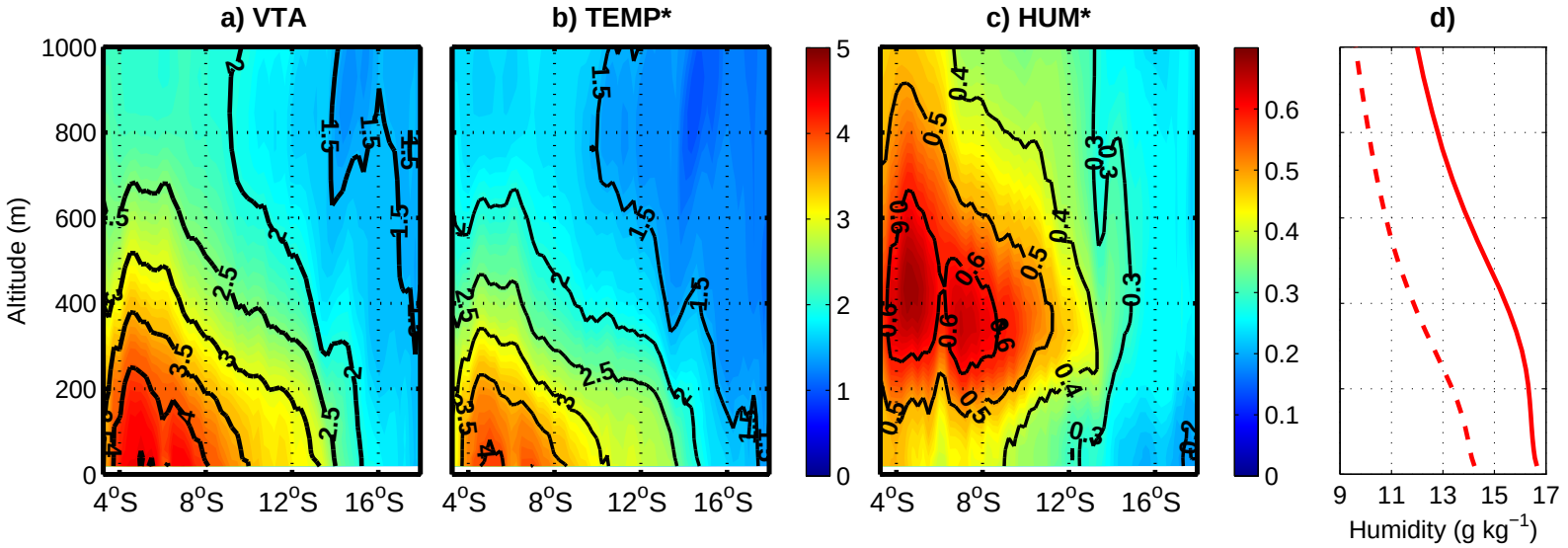
a) VTA
b) TEMP*
c) HUM*
d)
Altitude (m)
1000
800
600
400
200
0
4°S
8°S
12°S
16°S
5
4
3
2
1
0
0.6
0.5
0.4
0.3
0.2
0.1
0
9
11
13
15
17
Humidity (g kg^{-1})

Figure 9

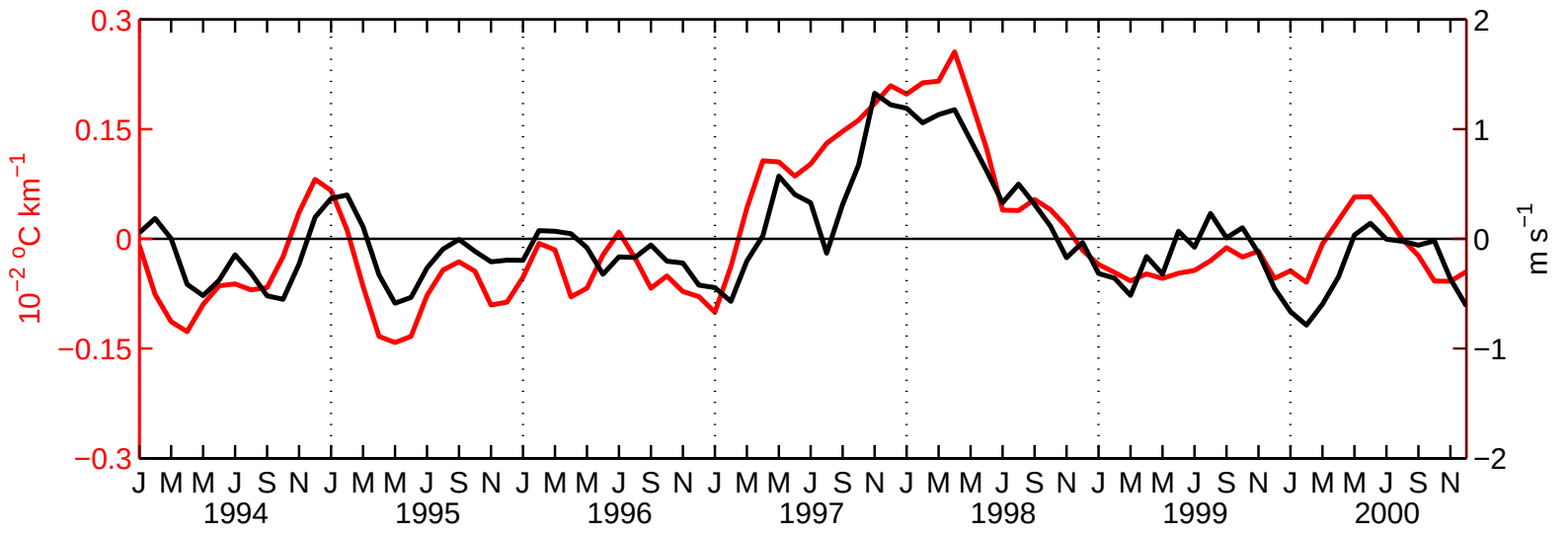
0.3
0.15
0
−0.15
−0.3
2
1
0
−1
−2
10^{-2} °C km^{-1}
m s^{-1}
J M M J S N J M M J S N J M M J S N J M M J S N J M M J S N J M M J S N J M M J S N
1994
1995
1996
1997
1998
1999
2000

Figure 10

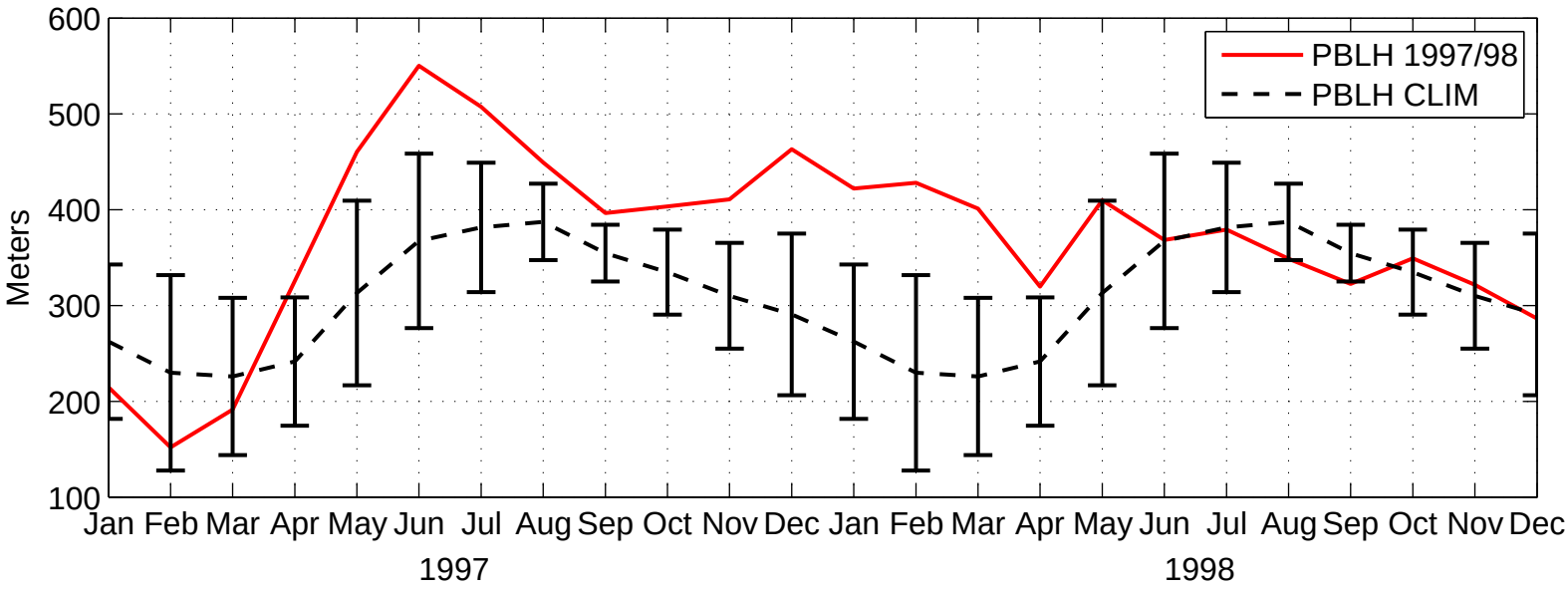
600
500
400
300
200
100
Meters
PBLH 1997/98
PBLH CLIM
Jan Feb Mar Apr May Jun Jul Aug Sep Oct Nov Dec Jan Feb Mar Apr May Jun Jul Aug Sep Oct Nov Dec
1997
1998

Figure 11

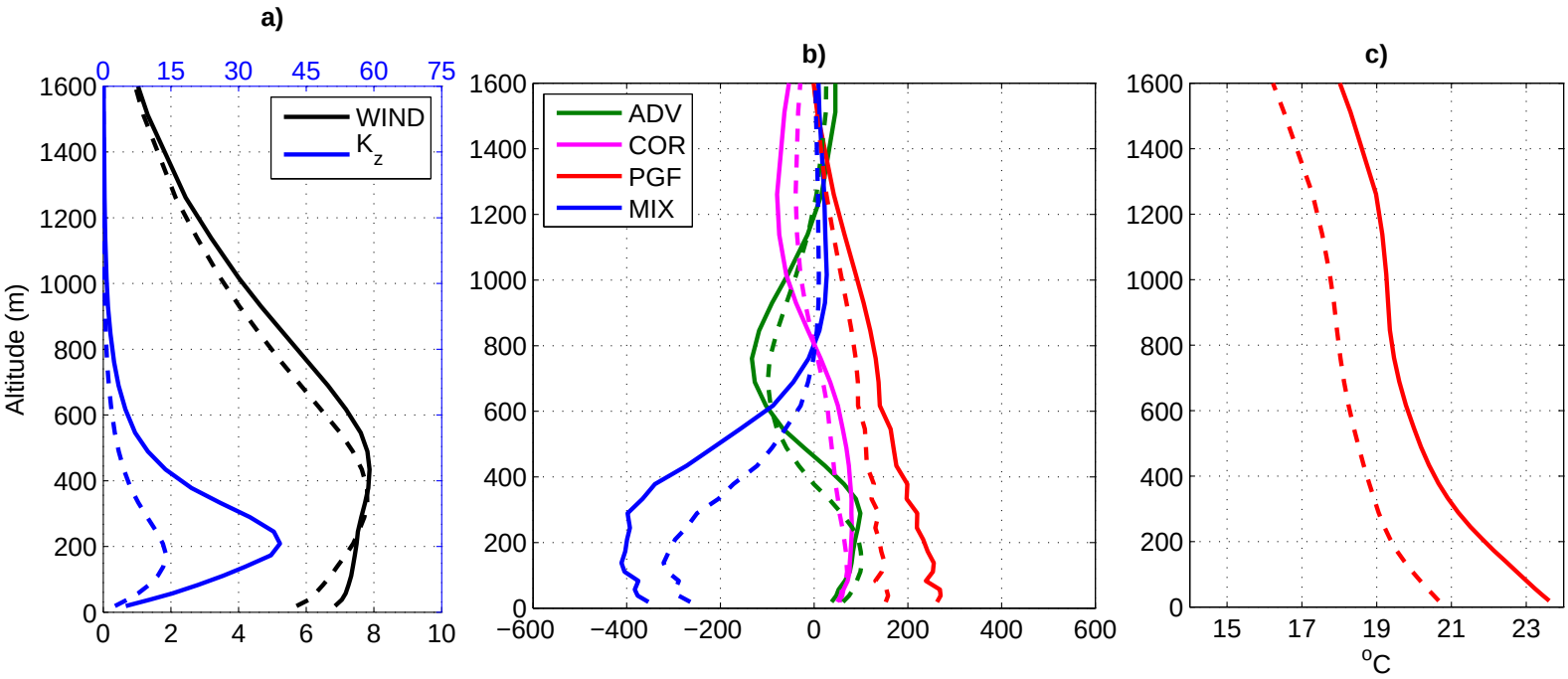

Figure 12

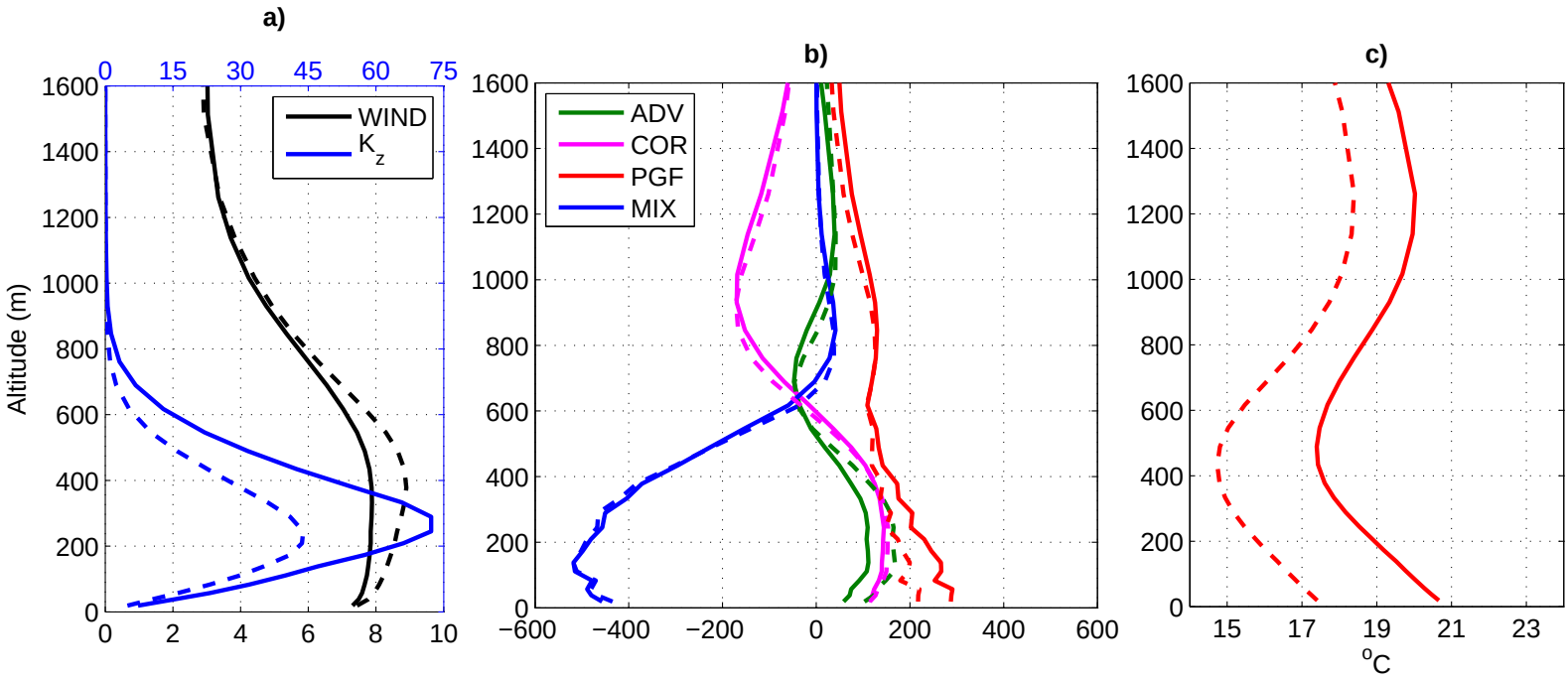

Figure 13

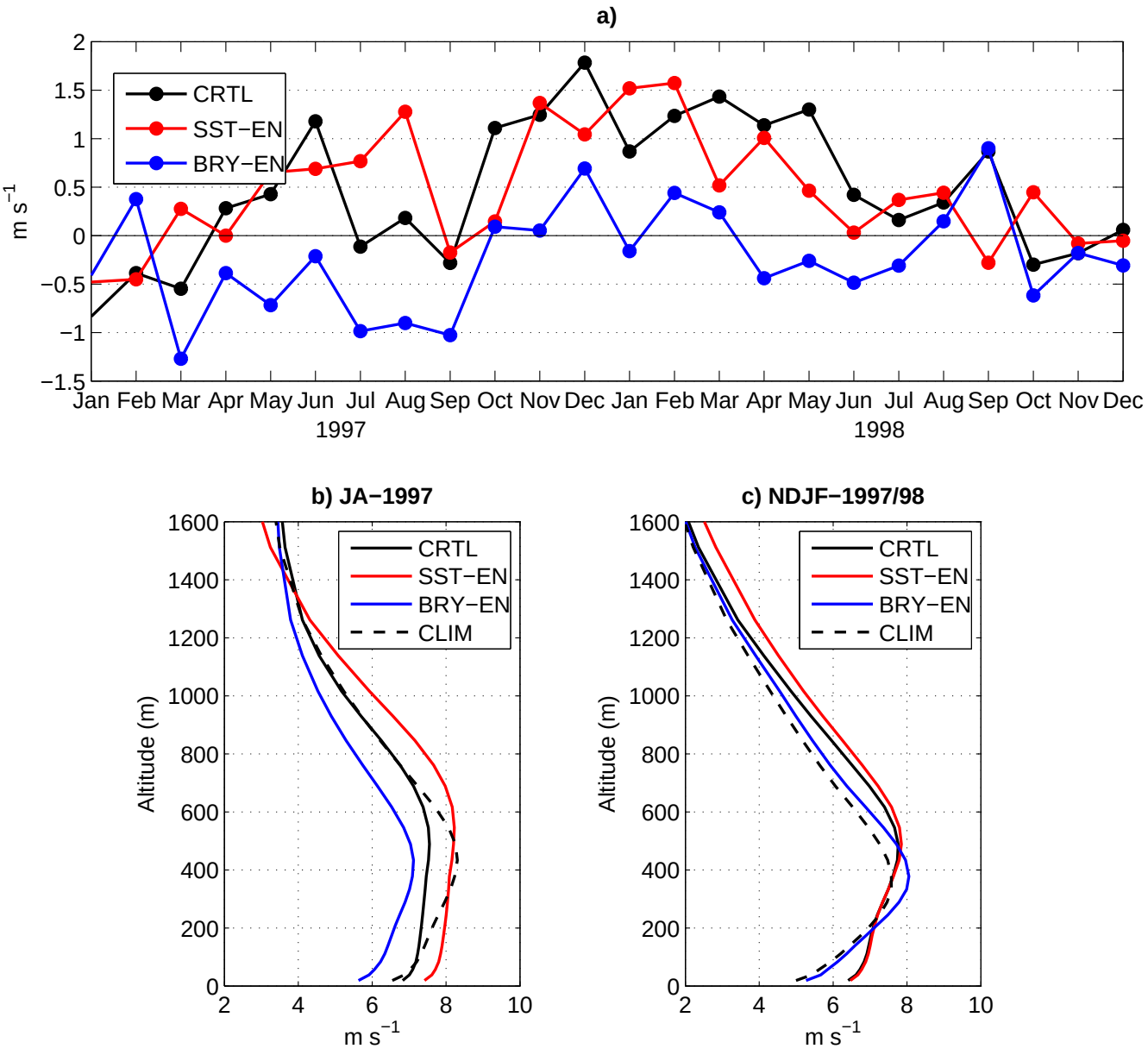
a)
CRTL
SST−EN
BRY−EN
m s−1
2
1.5
1
0.5
0
−0.5
−1
−1.5
Jan Feb Mar Apr May Jun Jul Aug Sep Oct Nov Dec Jan Feb Mar Apr May Jun Jul Aug Sep Oct Nov Dec
1997
1998
b) JA−1997
c) NDJF−1997/98
CRTL
SST−EN
BRY−EN
CLIM
Altitude (m)
1600
1400
1200
1000
800
600
400
200
0
2
4
6
8
10
m s−1

Figure 14

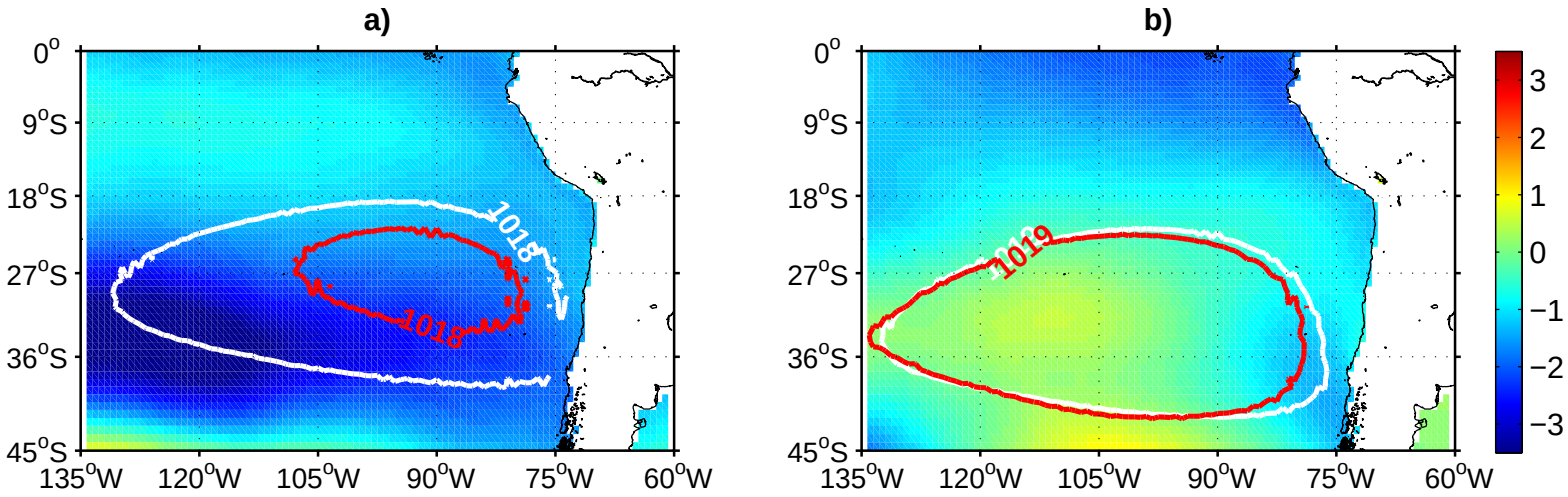
a)
b)
0°
9°S
18°S
27°S
36°S
45°S
135°W
120°W
105°W
90°W
75°W
60°W
1018
1016
1019
3
2
1
0
−1
−2
−3

Figure 15

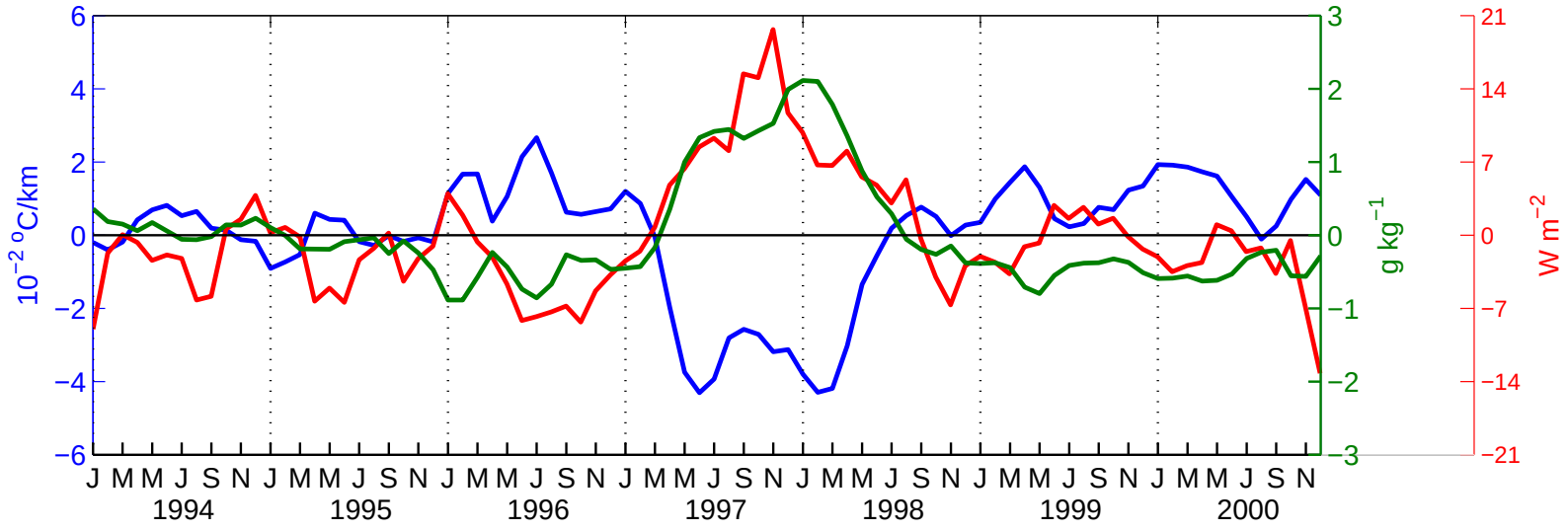
6
4
2
0
−2
−4
−6
10^{-2} °C/km
3
2
1
0
−1
−2
−3
g kg^{-1}
21
14
7
0
−7
−14
−21
W m^{-2}
J M M J S N J M M J S N J M M J S N J M M J S N J M M J S N J M M J S N J M M J S N
1994
1995
1996
1997
1998
1999
2000

Figure 16

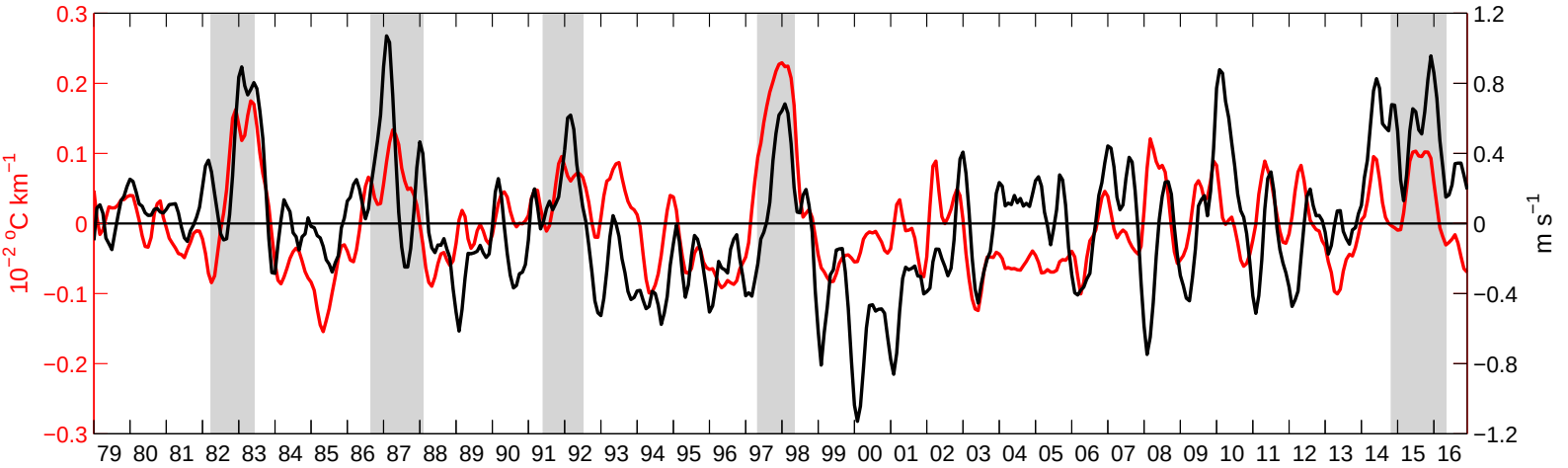
0.3
0.2
0.1
0
−0.1
−0.2
−0.3
10^{-2} °C km^{-1}
1.2
0.8
0.4
0
−0.4
−0.8
−1.2
m s^{-1}
79 80 81 82 83 84 85 86 87 88 89 90 91 92 93 94 95 96 97 98 99 00 01 02 03 04 05 06 07 08 09 10 11 12 13 14 15 16

Table 1

Table 1. Parameterizations used in WRF model for the simulations.

Processes	Scheme	Reference
Shortwave Radiation	Dudhia scheme	Dudhia (1989)
Longwave Radiation	RRTM scheme	Mlawer et al. (1997)
Microphysics	WRF Single-Moment 6-class scheme	Hong and Lim (2006)
Cumulus	Betts-Miller-Janjic scheme	Janjic (1994)
Surface Layer	MYNN surface layer	Nakanishi and Niino (2009)
Land Surface	Noah Land Surface Model	Chen and Dudhia (2001)
Planetary Boundary Layer	MYNN Level 2.5 PBL	Nakanishi and Niino (2009)

3.4 Additionnal results and discussion (not included in the paper)

Here, we extend our results and discussion about the wind drop-off in the model validation. We also extend our results on shortwave flux at air-sea interface and air temperature on land surface, which were useful to extend the discussion referring on land sea thermal contrast.

3.4.1 The wind drop-off

The wind decrease towards the coast (i.e. the wind drop-off) was poorly simulated by the model. The WRF winds are too strong at the coast in comparison with the satellite winds (Fig. 3.1). Capet et al. (2004) showed that increasing the spatial resolution (from 27 km to 3 km) in the COAMPS model increased the wind drop-off at the coast of California. However the range of spatial resolution in Capet et al. (2004) is higher than in our case (25 km) and the region is different (higher latitude, lower mountain range). Oerder et al. (2016) show that the simulated WRF wind drop-off (near 20 °S off South Peru) is in better agreement with satellite wind and rawinsonde data, when the model resolution is higher (∼9 km). This is likely due to a better representation of the coastal orography, among other effects. It will be verified in the next chapter. Besides, the wind drop-off can not be measured accurately with satellite wind measurements within 50 km from the coast. We will address this aspect of the wind in another chapter (section 4.3.1). The large differences between QSCAT and ERS offshore are probably due to differences in the algorithms that retrieve surface wind from the wind stress which are nearly directly measured by the scatterometers scaterrometers.

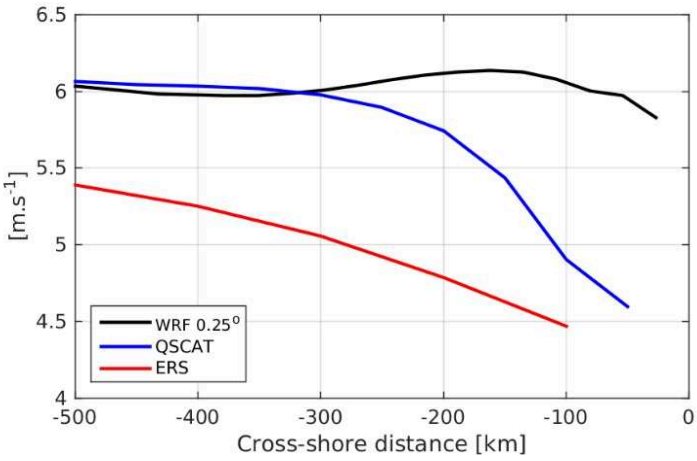

Fig. 3.1 *Mean zonal profiles of the wind speed in the year 2000, averaged between 7 °S and 13 °S, from WRF model, and the scatterometers QSCAT and ERS.*

3.4.2 Shortwave flux at the air-sea interface

The spatial distribution of the mean downward shortwave flux at the surface is not well reproduced by the model (specially over land) compared with data from two satellites (SRB and ISCCP; Fig. 3.2a, b and c). It is related with the difficulty to simulate the cloud cover in this region (Wyant et al., 2010). Satellite data shows two minimum shortwave flux patterns ($\sim$175 W m^{-2}) over sea located off the continental coast between 12–30 °S and between 0–8 °N in the Panama Bight region. Note that the shortwave flux measured by SRB is stronger than ISCCP data. The shortwave flux along the Peru-Chile coast is overestimated by the model by 13% off Peru and 20% off Chile with respect to ISCCP (less with respect to SRB). Moreover, the shortwave flux modelled is strongly underestimated over land on the steep slopes of the Andes and is overestimated in the Amazon basin rainforest.

On the other hand, eventhough the mean shortwave flux is poorly reproduced, the shortwave anomalies simulated by the model during 1997-1998 El Niño are of the correct magnitude (Figs. 3.2d, e and f)). Model and observations show strong shortwave positive anomalies ($\sim$50–70 W m^{-2}) between 0–8 °N and off the coast of northern Chile ($\sim$25 W m^{-2}).

Figure 3.3 shows the mean annual cycle of the shortwave flux from the model and observations in the coastal domain over sea and over land. Over sea the WRF downward shortwave flux annual cycle is in agreement with observations. Over land the WRF shortwave flux is strongly underestimated, particularly in summer with 250 W m^{-2} in the observations against 180 W m^{-2} in WRF (-28%). We may underestimate the land-sea thermal gradient due to this shortwave bias. Note that the poor representation of downward shortwave radiation and associated cloud cover in models of the Southeast Pacific lower troposphere is a well-known problem (e.g. Wyant et al. (2010)).

3.4.3 Air temperature on land surface

Despite the shortwave bias, the model reproduces reasonably well the surface air temperature distribution and, more importantly for the purpose of the present study, the air temperature anomalies at surface during EN, in agreement with reanalysis data (see Fig. 3.4). It shows that the air temperature increases more over sea than over land associated with the strong SST warming during El Niño, thus reducing the land-sea thermal contrast.

However, the land-sea thermal contrast is believed to have an impact on the wind at a smaller spatial scale, as suggested by Enfield (1981) in the region of Lima. To evaluate the skill of the model to reproduce the local air temperature conditions, we computed the mean annual cycle and the monthly averaged air temperature above land at 12 °S (Lima location) in the model. We found a temperature inversion in winter (see Fig. 3.5). These model results are in agreement with those computed by Enfield (1981) using rawinsonde data for the period 1963-1977 (see his Figure 4). We conclude that a high resolution modelling will be necessary to test the Enfield's conclusions.

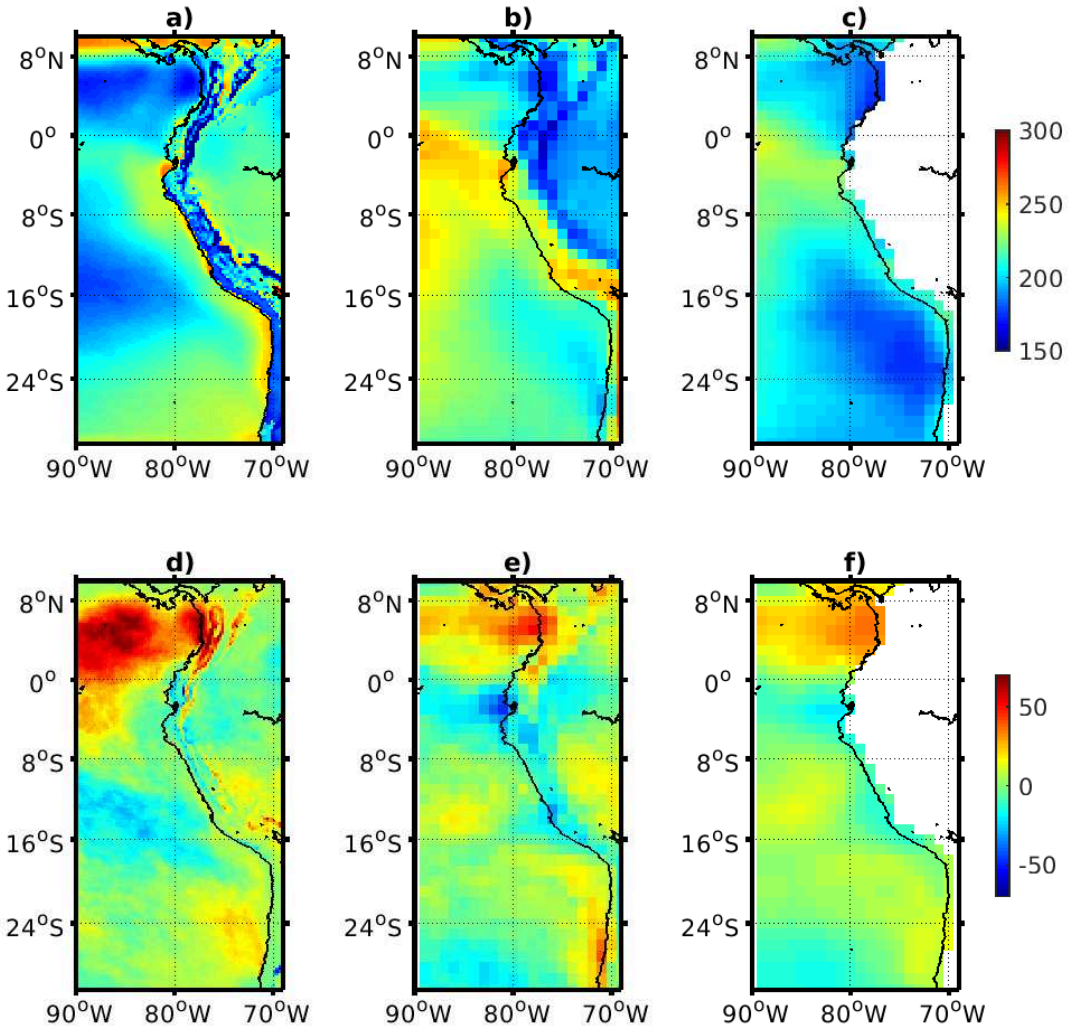

Fig. 3.2 *Mean shortwave flux at the surface* ($\mathrm{W\,m^{-2}}$) *for the period 1994-2000 from a) WRF, b) SRB and c) ISCCP. d-f) Respective anomalies during El Niño period November 1997-January 1998.*

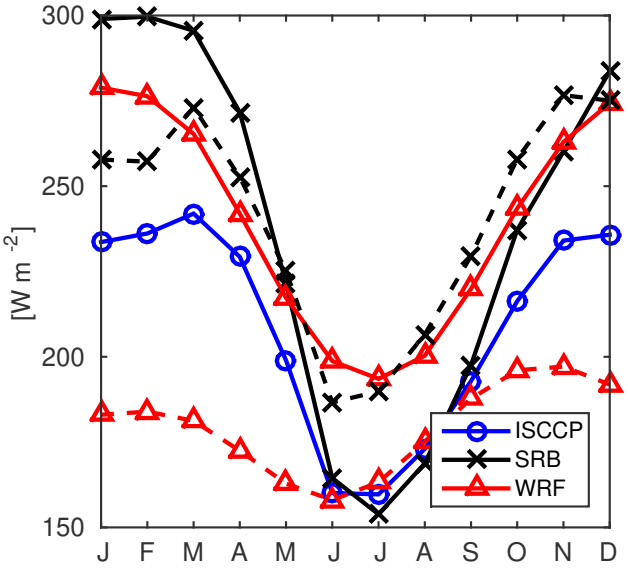

Fig. 3.3 *Mean annual cycle of the downward shortwave flux at the surface from WRF model and satellite observations (ISCCP, SRB). Data were averaged for the period 1994-2000 in a 100 km wide coastal domain over sea between* 7–15 °S. *Dashed lines correspond to data over a 100 km wide coastal domain over land. Note that ISCCP data is only available over sea.*

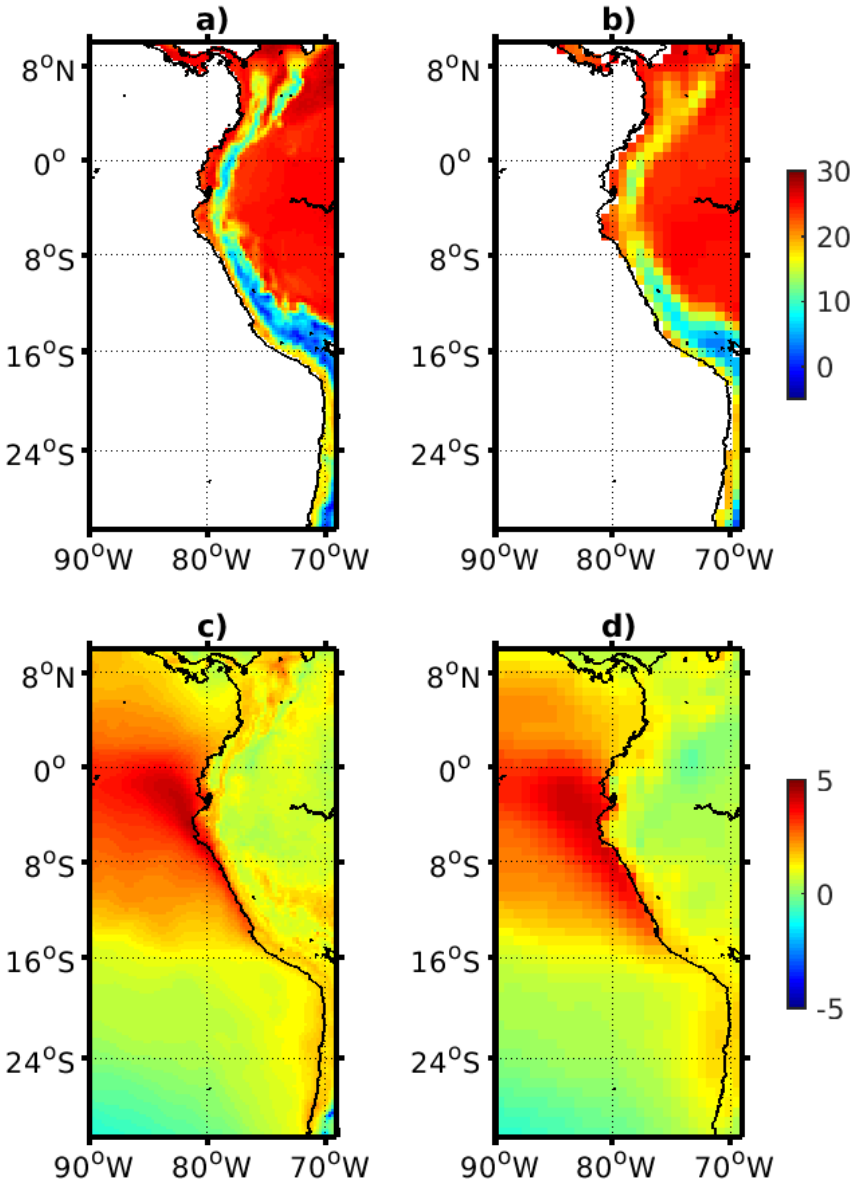

Fig. 3.4 *Air temperature at 2 meters over land from a) WRF model and b) ERA-interim. Anomalies of the air temperature at 2 meters from the surface during November 1997-January 1998 (Niño conditions) from c) WRF and d) ERA-interim. Units are in* °C.

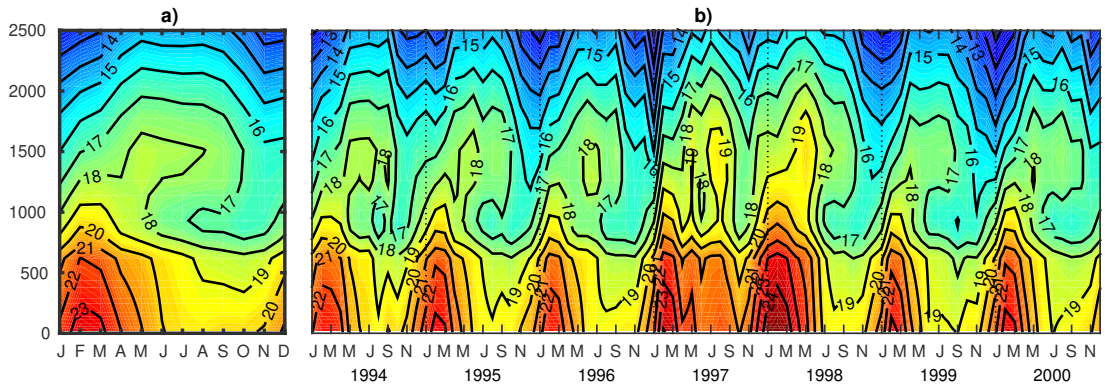

Fig. 3.5 *a) Mean annual cycle of air temperature over Lima (12 °S) and b) monthly average for the period 1994-2000.*

Chapter 4

Climate change impact on the Peruvian coastal winds

4.1 Introduction

Global Climate Models (GCMs) do not simulate realistically the wind and sea surface temperature in nearshore regions because of their coarse spatial resolution (∼100–200 km) and/or their regional biases (Belmadani et al., 2014; Wang et al., 2014). Hence, there is a great need to achieve the downscaling of GCMs climate change projections to obtain finer-scale projections with realistic representation of the regional conditions.

As mentioned in chapter 1, there are few regional studies about the impact of the climate change on the upwelling-favorable wind on the Peruvian upwelling system. Using scatterometer gridded winds ($0.5° \times 0.5°$) from QuikSCAT, Goubanova et al. (2011) applied a statistical downscaling method to obtain surface wind at ∼50 km of resolution from the outputs of the IPSL-CM4 global model. They found that surface alongshore winds off Peru show a significant weakening (5–10 %) in summer over the $2CO_2$ and $4CO_2$ scenarios. It was associated with a decrease of intraseasonal variability of the coastal winds off Peru. Belmadani et al. (2014) used the LMDz atmospheric global model with progressively refined horizontal resolution of $0.5° \times 0.5°$ in the Peru-Chile upwelling region. They found that downscaled winds show a weakening off Peru in both summer (20–30 %) and winter (5–10 %). They were associated with the SPA southward shift and the increase of precipitation over the tropics associated with convective anomalies.

The limitations of these regional wind projections are the models relatively low spatial resolution (∼50–100 km), the downscaling of a single global model, and the idealized CMIP3 scenarios ($2CO_2$ and $4CO_2$) that were used. In this chapter we assess the regional impact of climate change on coastal winds off Peru using a high resolution atmospheric model, the multi-model mean (MMM) of 31 CMIP5 models, and the new RCP8.5 pessimistic scenario. We also study the mechanisms governing local wind changes and relate them to previous findings from other authors.

4.2 Model and data

4.2.1 WRF model configuration

We used the WRF model version 3.7.1 with three nested domains (Fig. 4.1a). The largest domain encompasses the tropical Pacific region with a horizontal resolution of 105 km. It was also used to carry out downscaling of climate change projections of the South Pacific Convergence Zone (see Dutheil et al. (2018)). The second domain covers the Peru and Northern Chile regions (30 °S-12 °N) with a horizontal resolution of 21 km. The innermost domain covers nearly all of the Peru coast (17 °S-5 °S) with a horizontal grid spacing of 7 km. The high resolution of the innermost domain improves the representation of the orography and shape of the coastline (Fig. 4.1b). A total of 32 vertical levels were used in the parent domain, and 60 vertical levels in the second and innermost domain, with 21 levels in the first ∼1000 m which allows to represent better the coastal terrain located between the Andes and the ocean (Oerder, 2016). The physical parameterizations used in this study are described in section 2.3.

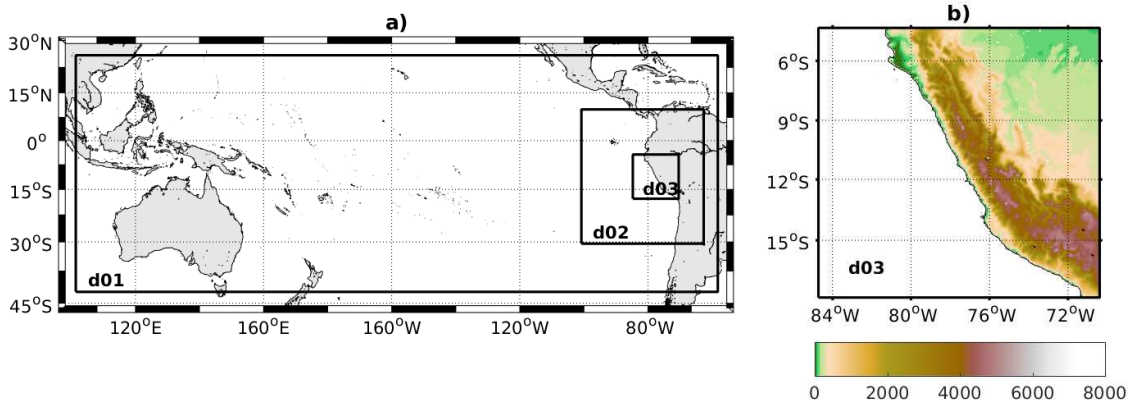

Fig. 4.1 *a) The three model domains used in the WRF simulations: d01, d02 and d03, with horizontal resolution of 105, 21 and 7 km respectively b) Model orography (in meters) above sea level for the innermost domain.*

4.2.2 Model simulations

First, we performed two simulations on the largest domain (WRF 105 km) independently: a control simulation over the period 1994-2003, using 6-hourly lateral boundaries conditions from the NCEP2 reanalysis and SST forcing from the OISST database (Reynolds et al. 2007); and a climate change simulation where anomalies of the seasonal cycle from the CMIP5 multi-model mean (CMIP5 MMM) for the RCP8.5 scenario (period 2086-2095) are added to the 6-hourly NCEP2 lateral boundary conditions and to the OISST forcing, following the same methodology as in Dutheil et al. (2018).

Then, two simulations (control and climate change) were performed on the nested domain of 21 km of resolution using the coarse solutions from the WRF 105 km simulations

in one-way nesting mode. Finally, high resolution simulations (7 km) were performed on the innermost domain using the solutions from the WRF 21 km simulations, control and climate change respectively.

Anomalies of the seasonal cycle from the CMIP5 MMM were generated from 31 CMIP5 climate models (see subsection 2.1.2). They are monthly differences of the future climate from 2080 to 2100 (RCP8.5 scenario) with the present climate from 1989 to 2009. It means that the interannual variability at the boundaries is prescribed in the future climate and is identical to that of the present climate. The anomalies are added to the NCEP2 temperature, water vapour mixing ratio, geopotential height, and wind at each vertical model level, and to the OISST sea surface temperature to build the boundary conditions, the initial state and the surface (SST) forcing of the climate change simulation. This methodology approach to assess future climate change, called the pseudo global warming method (PGW), allows to reduce the model bias of the CGCMs projection by the use of the climate difference estimated by the CGCMs (Rasmussen et al., 2011).

For example, Figure 4.2a shows the annual mean SST ensemble averaged for 31 global models over the period 1989-2009. It shows the well-known SST pattern in the tropical Pacific, warm pool in the west and a cold tongue in the east. This pattern is not well reproduced by the models compared to observations (Reynolds et al., 2007) given that they exhibit a quite robust and strong positive bias of ∼2–3 °C off the West coast of South America (Fig. 4.2b). This bias is well known and has been attributed to different processes: lack of low-altitude clouds, lack of upwelling of cool water, abscence of surface oceanic eddies (Richter, 2015). To build the SST forcing for the climate change simulation, we computed the monthly climatological differences in SST from the CMIP5 MMM between the period 2080-2100 (RCP8.5 scenario) and 1989-2009 (Fig. 4.2c). They are added to the SST forcing from NCEP2 (OISST), using the following equation:

$$SST(WRF_{RCP8.5}) = SST(NCEP2, daily) + SST_{clim}(CMIP5_{RCP8.5}, 2080{-}2100, monthly) - SST_{clim}(CMIP5_{historical}, 1989-2009, monthly)$$

This allows to filter the bias shown in Figure 4.2b. However it assumes (and it is a strong assumption) that the strong SST bias in the CMIP models has no impact on the amplitude of the CMIP SST anomalies, which is impossible to verify. A similar formula is used for other variables for the boundary conditions.

Note that the patterns of the SST climate anomalies (future-present) in summer and winter differ from each other off Peru (Fig. 4.3a, b), and the SST climate anomalies are stronger in June and are weaker in January-February in the nearshore area (100-km coastal band; Fig. 4.3c).

4.3 Results

4.3.1 Surface wind validation

We start with the evaluation of the simulated surface winds in the present period. To show the impact of the model resolution on modeled nearshore winds, the annual mean surface wind from WRF 105 km, WRF 21 km and WRF 7 km (here after referred to as WRF105,

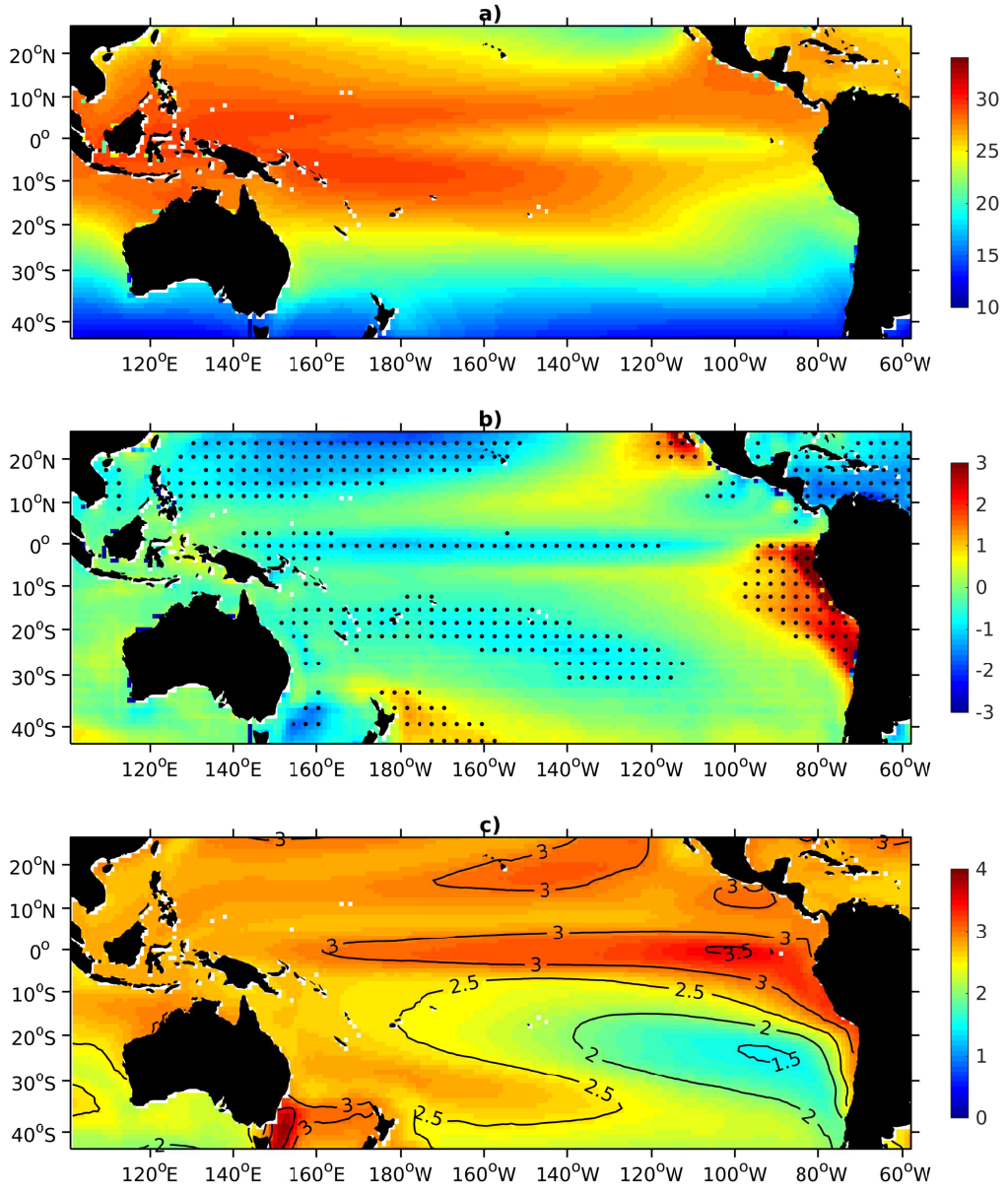

Fig. 4.2 *a)The annual ensemble mean SST for 31 global models (period 1989-2009). b) The annual ensemble mean SST bias calculated by the difference between the model SST and the AVHRR SST observations. The dots denote where 80% of the 31 models have the same sign for the SST bias. c) Differences in SST between the periods 2080-2100 (RCP8.5 scenario) and 1989-2009 (historical simulation) from 31 CMIP5 global climate models.*

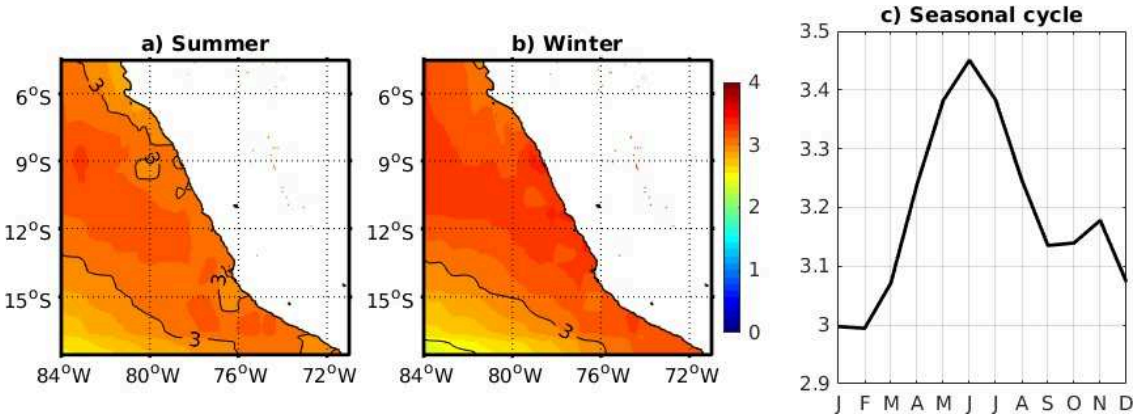

Fig. 4.3 *SST climate anomalies (future-present) in a) summer and b) winter in the Peru region. c) Seasonal cycle of the SST climate anomalies averaged in a 100 km coastal band between 7–15 °S. Data from the CMIP5 MMM.*

WRF21 and WRF7 respectively) are shown for the small model domain in Fig. 4.4a, b and c, respectively. Also shown is the climatological mean surface wind from QuikSCAT in Fig 4.4d. Satellite observations show that surface wind blows north-westward (approximately parallel to the coastline) with stronger intensity offshore (around 7.5 $\mathrm{m\,s^{-1}}$). The intensity of offshore winds (the trade winds offshore) is slightly overestimated by all model simulations (WRF105, WRF21 and WRF7). On the other hand, the wind intensity decreases shoreward, up to ∼4.5 $\mathrm{m\,s^{-1}}$ off the North coast in observations. It is well reproduced by WRF7, but overestimated by WRF105 and underestimated by WRF21.

Fig. 4.4e shows cross-shore profiles of wind speed (the so-called wind drop-off, Capet et al. (2004)) averaged between 7–13 °S obtained from the three model configurations and QuikSCAT observations. It shows that WRF105 produces a strong wind decrease shoreward (the so-called wind drop-off) but it cannot resolve the nearshore zone due to its lower resolution. WRF21 produces a weak wind drop-off in the first 200 km off the coast, and WRF7 reproduces reasonably well the wind drop-off in the coastal zone in agreement with observations. Note that the QuikSCAT satellite have a "blind zone" near the coast of approximately 50 km where no data are available (Bentamy and Fillon, 2012).

Figure 4.5 shows the climatological mean annual cycle of the alongshore wind off the Peru coast from WRF7 and QuikSCAT over the period 2000-2003. Overall, modelled and observed alongshore wind climatologies are in agreement on the seasonal cycle. The strongest winds (<7 $\mathrm{m\,s^{-1}}$) are found during austral winter (July–September) around 15 °S, where there is a well-marked seasonal cycle. It is well reproduced by the model. On the other hand, the alongshore wind is weaker during austral summer (January-March), especially between 5–12 °S. It is overestimated by the model by about 1 $\mathrm{m\,s^{-1}}$ (∼ 25% error).

Figure 4.6 shows the seasonal variability of the wind drop-off. According to QuikSCAT observations, the wind drop-off is stronger in summer and weaker in winter. The wind decrease from ∼5 $\mathrm{m\,s^{-1}}$ at 200 km offshore to ∼3.8 $\mathrm{m\,s^{-1}}$ at 50 km offshore in summer (i.e. 8×10^3 m/s/km), and it decrease from ∼6.5 $\mathrm{m\,s^{-1}}$ at 200 km offshore to ∼5.7 $\mathrm{m\,s^{-1}}$ at 50 km offshore in winter (i.e 5×10^3 m/s/km). The model reproduces well the cross-shore

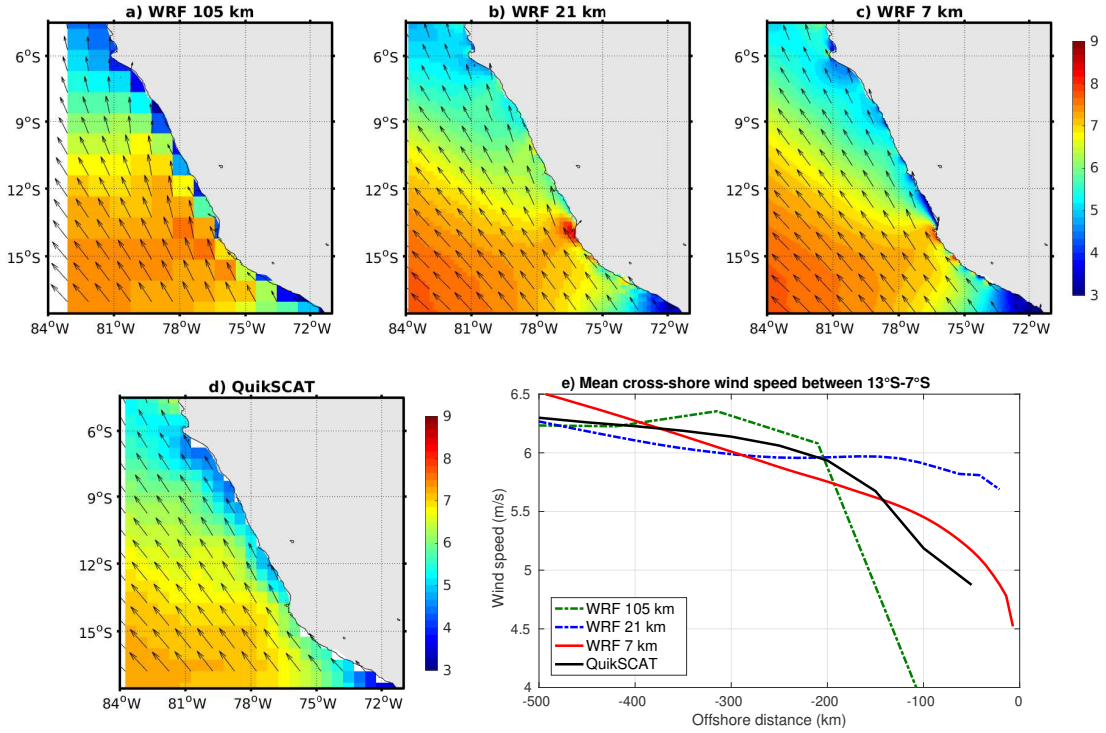

Fig. 4.4 *Mean surface wind for the period 2000-2003 from a) WRF105, b) WRF21, c) WRF7 simulations, and d) QuikSCAT satellite observations. e) Mean cross-shore surface wind speed between 7–13 °S.*

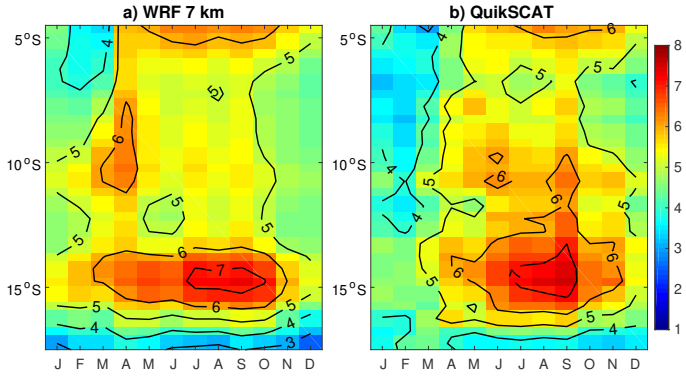

Fig. 4.5 *Mean annual cycle of alongshore wind (averaged in a coastal band of ∼100 km) from a) WRF7 and b) QuikSCAT over the period 2000-2003. Model data was interpolated on the 1/4° QuikSCAT grid.*

wind speed compared to QuikSCAT, except in summer where modelled wind speed is overestimated by about $1\,\mathrm{m\,s^{-1}}$ at 100 km offshore. Unfortunately there are no in situ observations such as the VOCALS data base to evaluate the nearshore wind in summer.

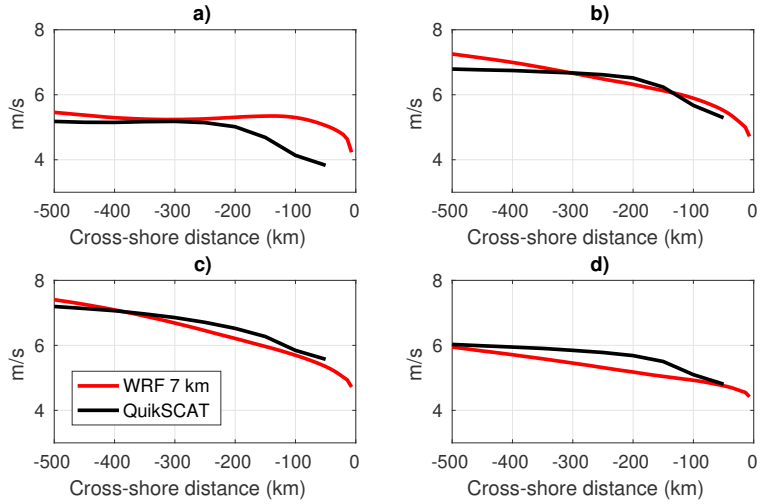

Fig. 4.6 *Mean cross-shore surface wind speed (between 7–13 °S) in a) summer, b) autumn, c) winter, and d) spring, for the period 2000-2003, from WRF7 (red lines) and QuikSCAT (black lines).*

4.3.2 Future changes in the mean and seasonal cycle of the surface wind

The mean surface winds in the period 2086-2095 under the scenario RCP8.5 from WRF21 and WRF7 are shown in Figures 4.7a and 4.7d respectively. Their differences with the period 1994-2003 are shown in Figures 4.7b and 4.7e. Also shown is the relative change (in %) in the mean seasonal cycle of alongshore winds off the Peru coast (Figures 4.7c and 4.7f). We found weak changes in the mean state of the surface winds. Wind change in the offshore region is positive, about $0.2\,\mathrm{m\,s^{-1}}$ at 400-km offshore and it decreases shoreward. In the nearshore region, wind change is slightly negative off the northern and southern coast of Peru, and is slightly positive off the central coast. Positive change in the nearshore region between 11–14 °S is greater in WRF7 than in WRF21. Concerning the change in the seasonal cycle of the alongshore winds, they tend to weaken in spring and summer (by ∼5 %) off the northern and southern coast, and alongshore winds tend to intensify in fall and winter off the central coast by ∼5 % in WRF21 and ∼10 % in WRF7. Wind differences driven by resolution will be discussed later (section 4.4).

Figure 4.8 shows that the offshore wind changes can be different from the nearshore wind changes, for example the offshore wind speed changes are always positive, whereas the nearshore wind changes are negative in summer and positive in winter. Something peculiar happens between 11 °S and 14 °S near the coast (north of the Paracas peninsula, where Pisco bay is located), where wind change is always positive. This will be discussed in more details in next section.

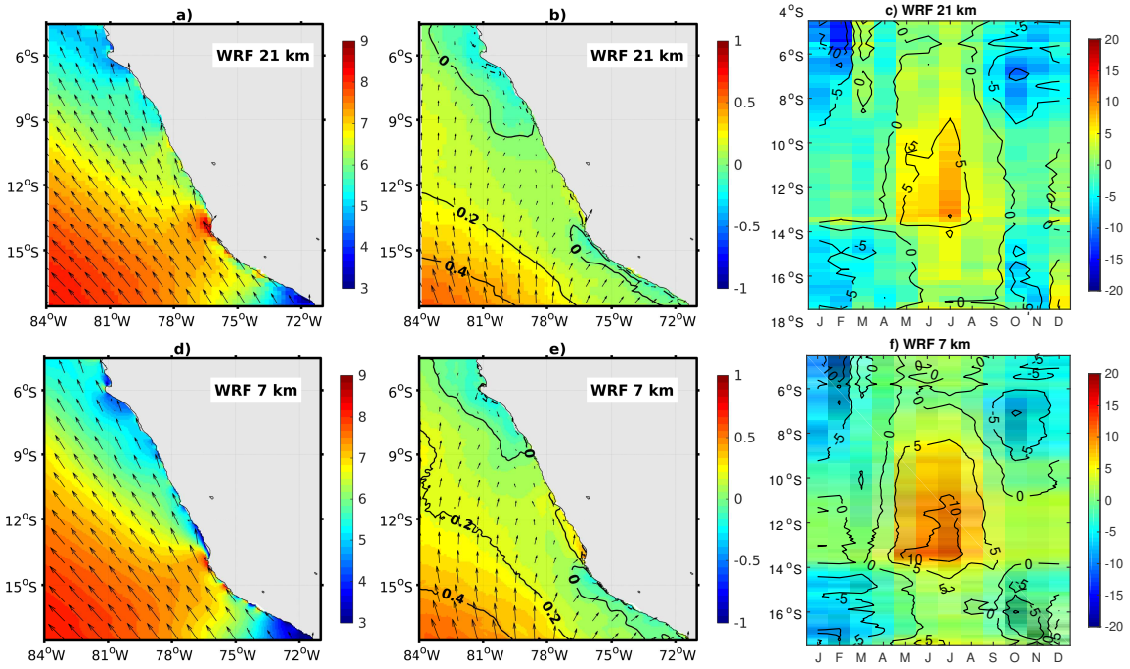

Fig. 4.7 *Mean surface wind in the period 2086-2095 under the RCP8.5 scenario from a) WRF21 and d) WRF 7km. Change in mean surface wind (2086-2095 average minus 1994-2003 average) from b) WRF21 and e) WRF7. Relative change (in %) in the mean seasonal cycle of alongshore winds (in a coastal band of ∼100 km) for the period 2085-2095 relative to the period 1994-2003 from c) WRF21 and f) WRF7.*

4.3.3 Climate-change induced modifications of the momentum budget

First, in order to investigate the spatial patterns of the forces which drive the surface winds off Peru under historical and future conditions, we computed the annual mean meridional component of the forces in the first layer of the model for the whole domain (Figs. 4.9 and 4.10). Second, to examine the coastal wind change dynamics, we computed the summer and winter mean of the wind and the alongshore forces in a coastal band of 100 km along the Peru coast (Figs. 4.11 and 4.12).

Figure 4.9 shows the spatial structure of the different forces driving the meridional surface wind in present conditions (period 1994-2003). These terms are computed in the model surface layer in contact with the ocean (see subsection 2.3.3). Note that winds off Peru are mostly oriented South-North. Figure 4.9a shows the advection term (V_ADV). In most of the domain the magnitude of this term is nearly zero, except in the nearshore region north of 14 °S off the Pisco bay. There, this term shows a local positive maximum, showing that it accelerates the meridional wind locally.

Figure 4.9b shows the pressure gradient (V_PGF). This term is positive in nearly the whole region. It shows high values off the South coast and offshore, which decrease to the north. Particularly, it shows a local negative minimum value north of 14 °S off the Pisco bay in contrast to the advection term local positive maximum. The Coriolis (V_COR) and vertical mixing (V_MIX) terms are negative in the whole region (Figs. 4.9c and

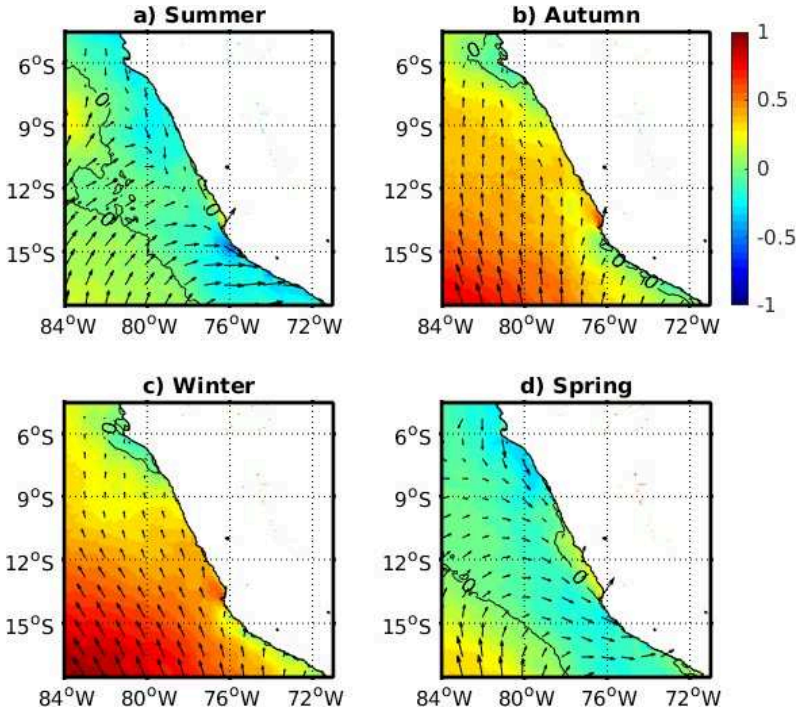

Fig. 4.8 *Change in mean surface wind in a) summer, b) autumn, c) winter, and d) spring, from WRF7 simulation.*

4.9d). They show strongly negative values off the South coast that decrease to the north showing some similar structures to those seen in the pressure gradient term.

Comparison of advection, pressure gradient, Coriolis and vertical mixing terms shows that in general the pressure gradient is the dominant force (Fig. 4.9b), which is mainly compensated by the Coriolis force and vertical mixing (Figs. 4.9c and 4.9d), except in the nearshore region north of 14 °S off the Pisco bay where advection plays an important role in balancing the negative pressure gradient. On average over the time period, trends in the wind (DV/dt) are much weaker than the other terms of the momentum balance (not shown).

Figure 4.10 shows the momentum anomalies due to climate change, i.e. the difference between the RCP8.5 (period 2086-2095) and the present time (period 1994-2003). Comparison of change in advection, pressure gradient, Coriolis and vertical mixing shows that at large scale pressure gradient and vertical mixing are the dominant forces (Figs. 4.10b and 4.10d). The pressure gradient change shows relatively strong positive anomalies ($\sim$150 m s^{-1}) in the South-West region that decrease shoreward. The vertical mixing change is negative and opposed to the pressure gradient change. The two terms almost balance each other everywhere in the domain, except in the nearshore region north of 14 °S off the Pisco bay where advection change is positive and relatively strong (Fig. 4.10a) and pressure gradient change is negative. The Coriolis term change has smaller values (Fig. 4.10c).

In order to analyze the dynamical processes associated with the upwelling-favorable winds off the Peru coast, an alongshore momentum budget is performed in a 100-km

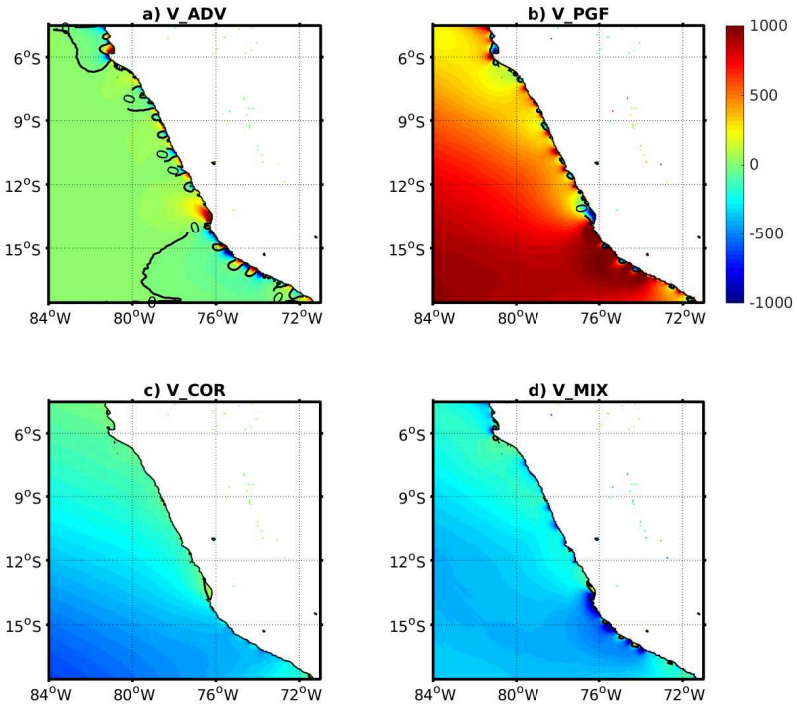

Fig. 4.9 *Mean annual meridional component of the surface forces (in* $\mathrm{m\,s^{-1}}$*) in the period 1994-2003: a) advection (V_ADV), b) pressure gradient (V_PGF), c) Coriolis force (V_COR) and d) turbulent vertical mixing (V_MIX).*

coastal band following Belmadani et al. (2014). Results show that the alongshore momentum budget is dominated by pressure gradient and vertical mixing, which compensate each other (Figs. 4.11b and 4.12b for summer and winter, respectively), except between 12–14 °S (off the Pisco bay) where the advection term plays an important role in the momentum balance. In addition, it shows that the model at high resolution is able to capture a lot of the alongshore wind variability that is induced by the capes and bays along the coast, as shown by Boé et al. (2011) and Renault et al. (2015) for the California region.

In future conditions during summer (January-March), the pressure gradient decreases along the coast for the most part (Fig. 4.11c) similarly as the alongshore winds (Fig. 4.11a). The pressure gradient decrease is stronger between 14–17 °S where the alongshore wind decrease is about $-0.5\,\mathrm{m\,s^{-1}}$. It will be shown in section 4.3.5 that the decrease in pressure gradient and alongshore winds during summer is in association with the poleward displacement of the South Pacific Anticyclone.

On the other hand, the alongshore wind increases along the coast between 8–15 °S in winter (July-September) under future conditions (Fig. 4.12a). As in summer, the pressure gradient and vertical mixing are the dominant forces driving the wind along the coast, except between 12–14 °S where advection plays an important role (Fig. 4.12b). In future conditions, the pressure gradient tends to increase relatively strongly (∼16 %) between

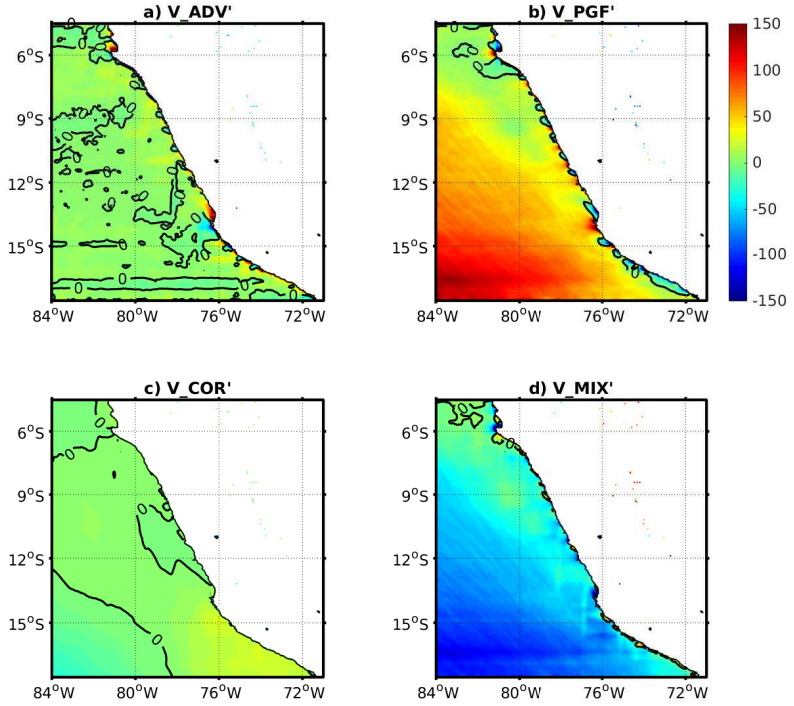

Fig. 4.10 *Change in the mean annual meridional component of the surface forces (in* $\mathrm{m\,s^{-1}}$*) between the period 2086-2095 under the scenario RCP8.5 and the period 1994-2003: a) advection (V_ADV), b) pressure gradient (V_PGF), c) Coriolis force (V_COR) and d) turbulent vertical mixing (V_MIX).*

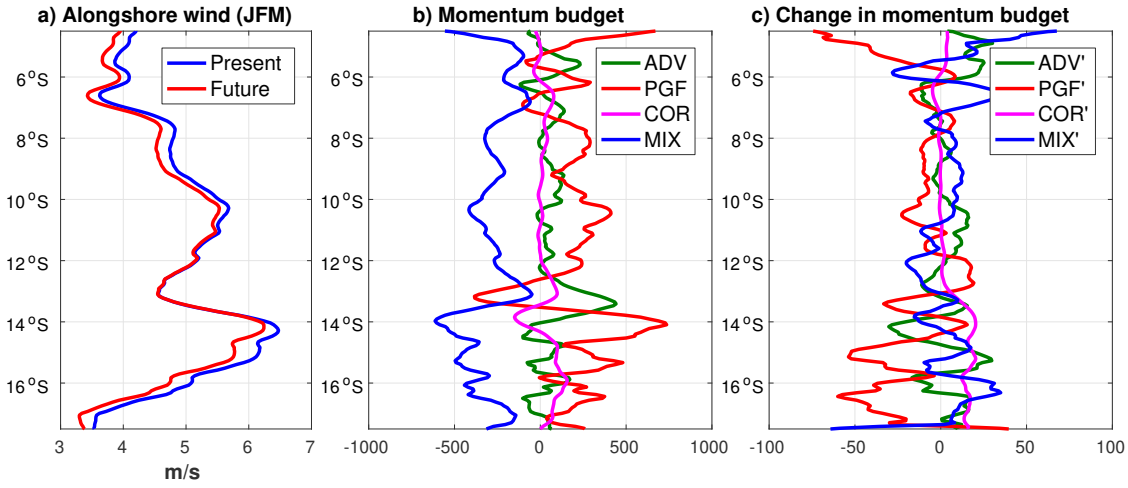

Fig. 4.11 *a) Mean alongshore wind along the Peru coast in summer (January-March) for present (1994-2003) and future (2086-2095) conditions. b) Mean alongshore momentum budget along the Peru coast for present conditions. c) Projected change in the mean alongshore momentum budget.*

13.5–15.5 °S and moderately (∼13 %) between 9–12.5 °S, while the advection term tends to increase moderately (∼10 %) between 7–14 °S (Figs. 4.7c).

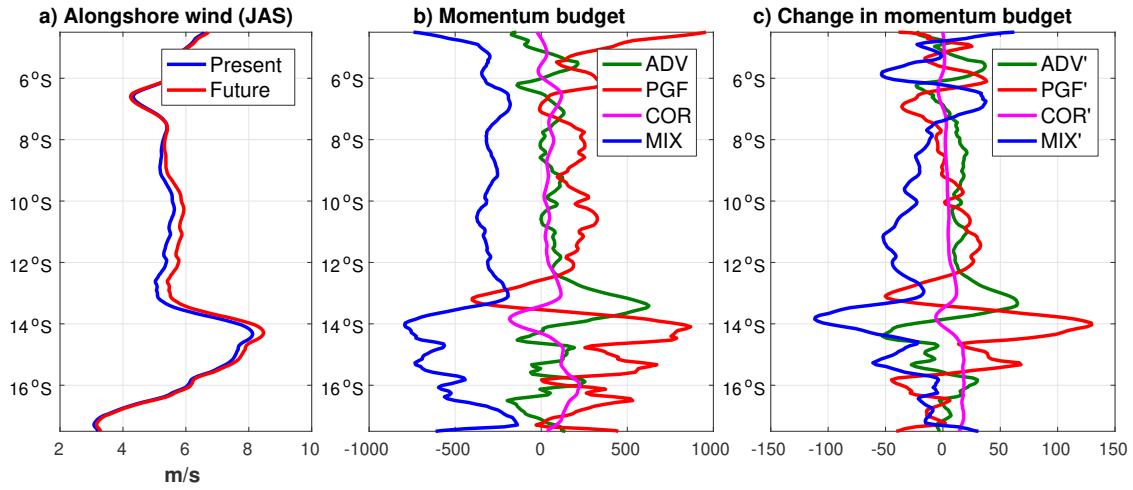

Fig. 4.12 *Same as Fig. 4.11 but for winter (July-September)*

Advection terms of the momentum budget and local wind intensification

We found that the advection term of the momentum budget plays a major role in the coastal wind local intensification observed between 12–14 °S in the Paracas-Pisco bay (Fig. 4.12c) during May-August. In order to investigate the zonal, meridional and vertical advection of momentum, we computed these terms offline from the climatological velocities. We used the following formula:

$$V\_ADV = -U\frac{\partial V}{\partial x} - V\frac{\partial V}{\partial y} - W\frac{\partial V}{\partial z}$$

where V_ADV is the total advection of meridional momentum, $-U\partial V/\partial x$ is the zonal advection term (V_ADV_x), $-V\partial V/\partial y$ is the meridional advection term (V_ADV_y), and $-W\partial V/\partial z$ is the vertical advection term (V_ADV_z) of the meridional momentum.

Figure 4.13 shows the mean total advection term of meridional momentum and their respective zonal, meridional and vertical contributions between May and August in present conditions in the Paracas-Pisco bay area. It shows that downwind of the peninsula, the advection accelerate the meridional wind component V (Fig. 4.13a). This has been documented in previous studies of expansion fans near capes (e.g. Perlin et al. (2011); Soares et al. (2018)). This wind acceleration is mainly due to the meridional advection term that largely dominates (Fig. 4.13c). The zonal advection is weak (even slightly negative near the cape; Fig. 4.13c), with the exception of the inner bay where it is of comparable intensity than the meridional advection. The contribution of the vertical advection term is negligible, except around the cape (positive downwind and negative upwind of the peninsula; Fig. 4.13d).

Figure 4.14 shows the change in total advection and the change in the zonal, meridional and vertical terms over May-August under future conditions. The total advection

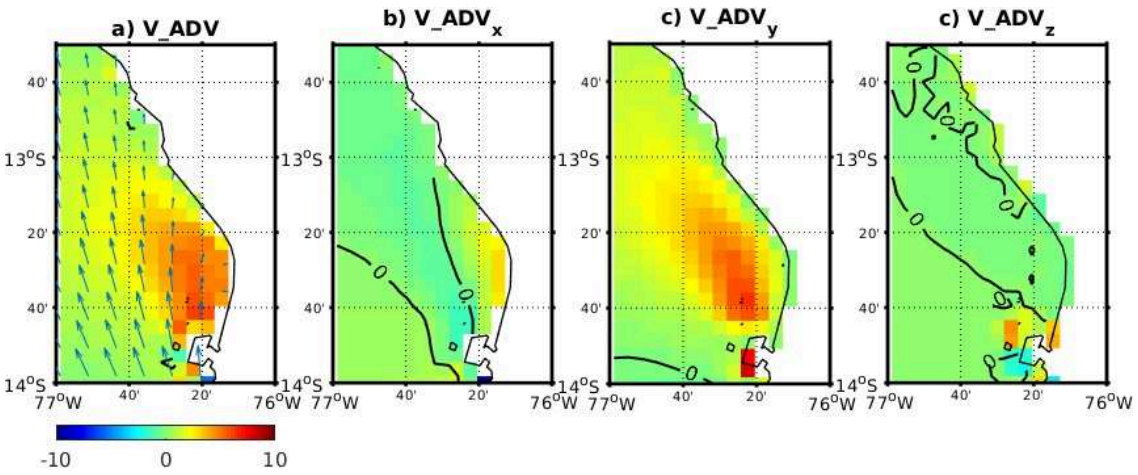

Fig. 4.13 *a) Total advection of meridional momentum over May-August under present conditions and their respectives b) zonal, b) meridional and vertical contributions in the Paracas-Pisco bay area. Arrows in a) indicate surface winds.*

term increases in the bay area under future conditions (Fig. 4.14a). The zonal advection term is enhanced nearshore in the bay (Fig. 4.14b), whereas the meridional term is enhanced mainly north of the Paracas peninsula (76°20′W,13°50′S; Fig. 4.14c). The vertical advection term is enhanced around the cape (Fig. 4.14d). Overall, the total advection term increase is mainly related to change in the meridional advection.

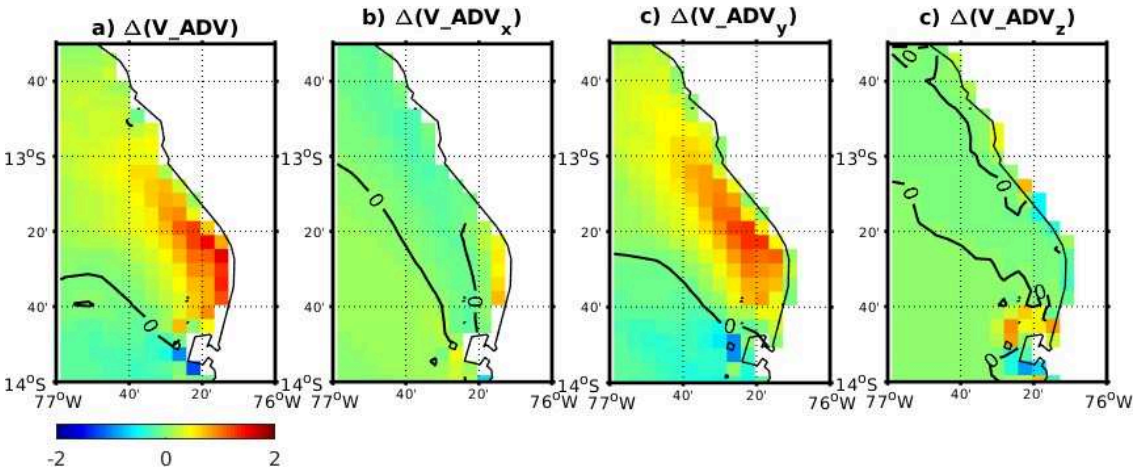

Fig. 4.14 *a) Change in total advection of meridional momentum over May-August under future conditions. Change of the b) zonal, b) meridional and vertical advection contributions.*

4.3.4 Future changes in the vertical structure of the PBL

Here we examine the changes in the mean vertical structure of the PBL (turbulent vertical mixing coefficient (K_z), temperature, and momentum vertical mixing term) between

present and future conditions. Spatio-temporal averages are computed between 7–15 °S and within the first 100 km from the coast.

Figures 4.15a-b show the vertical sections of the annual mean air temperature along the Peru coast for future and present conditions, respectively. The air temperature shows an almost homogeneous increase of 3–4 °C between the surface and 1600 m. There remains a well marked temperature inversion in winter and not in summer (Fig. 4.15c). Similarly, the air humidity in the vertical section increases almost uniformly by 2–3 g kg^{-1} between the surface and 1600 m (Fig. 4.16a-b), both during summer and winter (Fig. 4.16c).

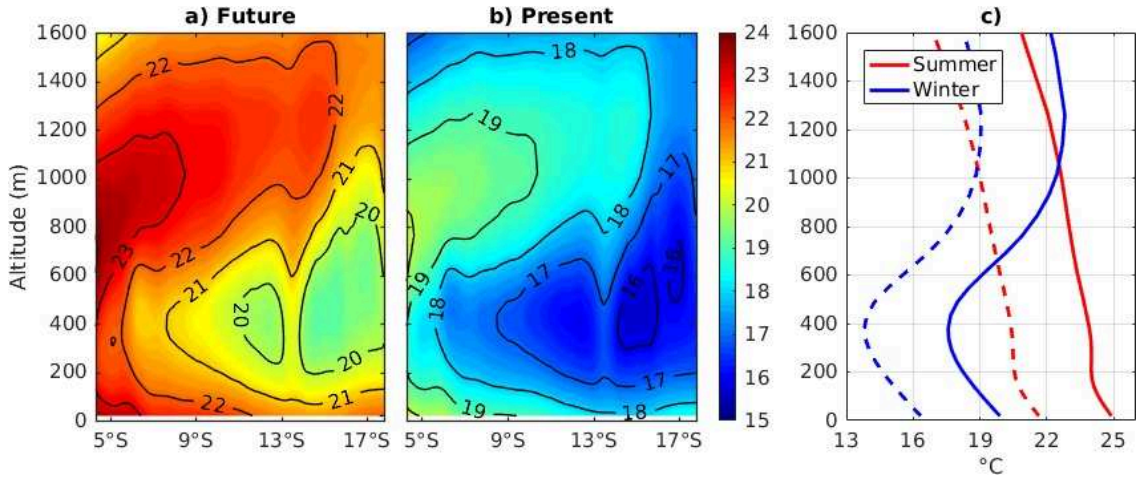

Fig. 4.15 *Alongshore vertical section of the annual mean of air temperature for a) future and b) present conditions. c) Air temperature vertical profile for summer and winter seasons in future conditions. Doted lines show the air temperature in present conditions.*

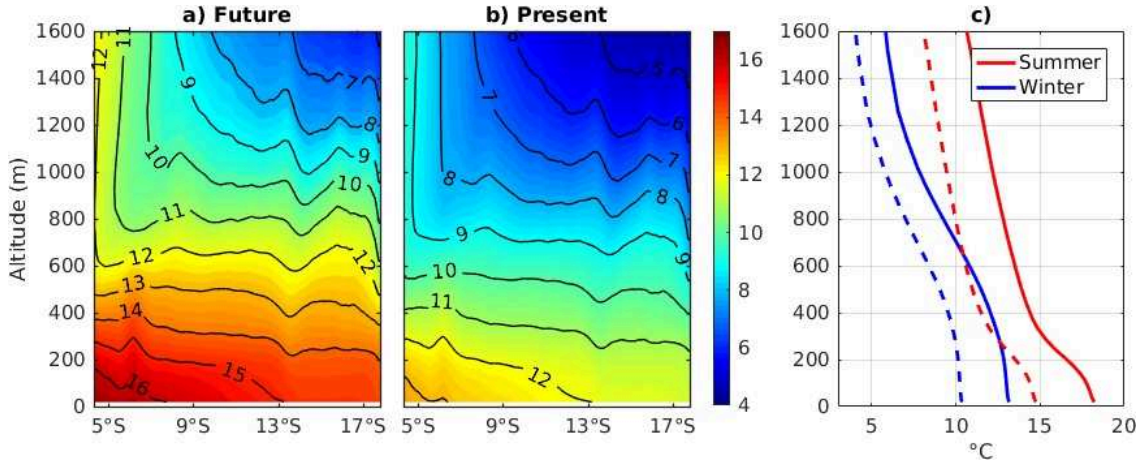

Fig. 4.16 *Alongshore vertical section of the annual mean of air humidity for a) future and b) present conditions. c) Air humidity vertical profile for summer and winter seasons in future conditions. Doted lines show the air humidity in present conditions.*

The vertical profiles of alongshore wind, turbulent vertical mixing coefficient, and momentum terms show very weak changes between the surface and 1600 m in summer (Fig. 4.17). On the other hand, while the mixing coefficient almost does not change in winter (Fig. 4.18), the wind intensification in winter occurs between the surface and ∼700 m with a maximun change at ∼300 m which produces a slight increase of the wind shear below ∼300 m.

The contribution of the wind shear increase to the turbulent stress ($\tau = K_z.dV/dz$) and the unchanged vertical mixing coefficient (K_z) act such that the momentum vertical mixing is reduced in winter in warm conditions (Fig. 4.18a; blue line in Fig. 4.18b). This means that a less efficient downward vertical flux of momentum from the upper layers to the surface layer occurs in winter under warm conditions. It is balanced by the increase of pressure gradient and advection terms (green and red lines respectively in Fig. 4.18b).

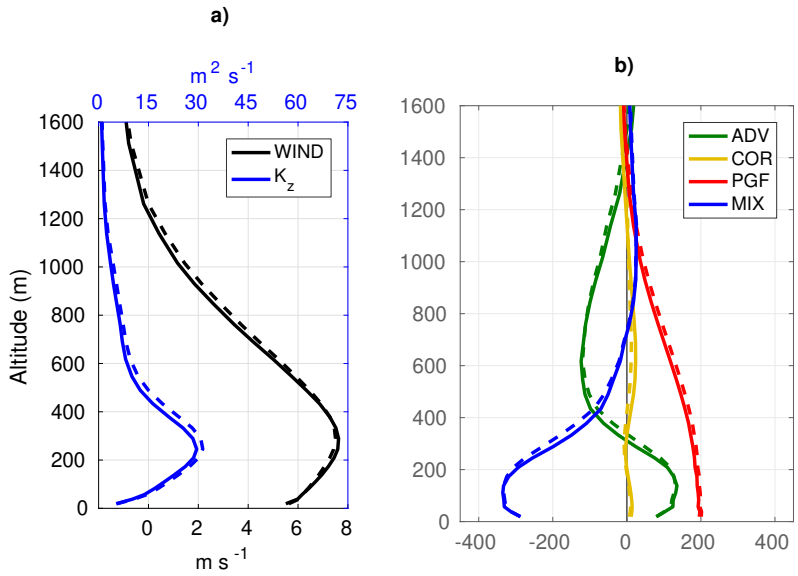

Fig. 4.17 *Mean summer vertical profile of a) alongshore wind (in* $\mathrm{m\,s^{-1}}$*) and turbulent vertical mixing coefficient (*K_z *in* $\mathrm{m^2\,s^{-1}}$*) and b) alongshore forces (in* $\mathrm{m\,s^{-1}}$*). Average were computed between* 7–15 °S*, and within* 100 km *from the coast. Full and dashed lines correspond to future and historical conditions, respectively.*

4.3.5 Role of the large scale atmospheric forcing and local forcing

In this subsection, we analyze the possible mechanisms which could govern the coastal wind changes.

a) The South Pacific Anticyclone (SPA)

Changes in alongshore winds may be driven by changes in the large scale atmospheric circulation, particularly the strength and location of the South Pacific Anticyclone (SPA). Figure 4.19 displays the changes in surface atmospheric pressure during the summer and winter seasons.

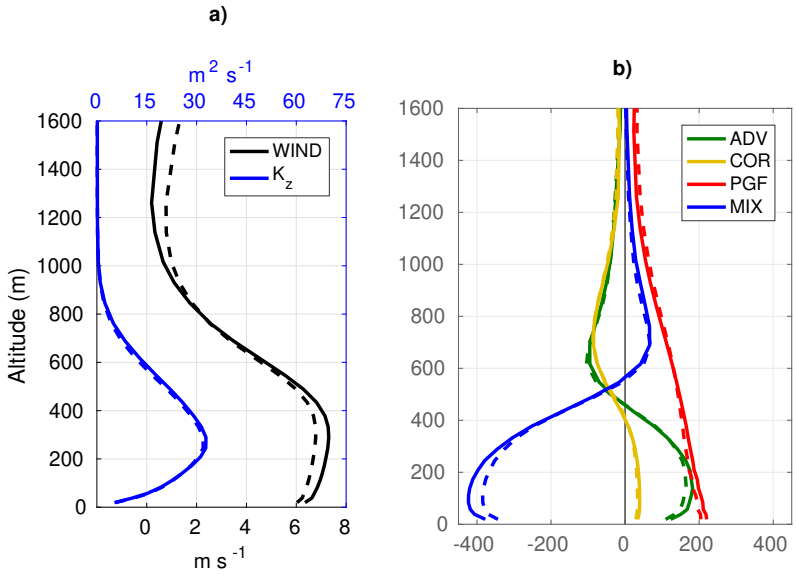

Fig. 4.18 *Same as Fig. 4.17 but for winter.*

In summer, the SPA is located at its southernmost position and is less intense (white lines in Fig. 4.19a). It moves towards southwest (away from the Peru coast) and the pressure at its center increases by ∼2 hPa under future conditions with respect to present conditions (black lines in Fig. 4.19a). It results that the surface atmospheric pressure increases at subtropical latitudes off Chile and decreases at tropical latitudes off the Peru coast (shading colors in Fig. 4.19a). This likely induces the decrease in alongshore pressure gradient (Fig. 4.11c) that induces a general weakening of alongshore winds off Peru coast in summer (Fig. 4.11a).

In winter, the SPA is located at its northernmost position and is more intense than summer (white lines in Fig. 4.19b). It almost does not change its position but the pressure at its center increases in ∼2 hPa under future conditions (black lines in Fig. 4.19b). This produces an intensification of surface atmospheric pressure off Peru and Chile, strong at subtropical latitudes and weak at tropical latitudes (shading colors in Fig. 4.19b). This likely increases the pressure gradient off the Peru coast and, consequently, may produce the moderate wind increase.

Monthly variations of the SPA (intensity, latitude and longitude of the maximum pressure within the SPA) are shown in Figure 4.20. Under present conditions, the seasonal variation of the intensity shows a maximum in September-October (∼1026 hPa) and minimum in May (∼1022 hPa, blue line in Fig. 4.20a). Moreover, the center of the SPA is located at its southernmost position in February (∼34.5 °S) and at its northernmost position in June (∼28.5 °S, blue line in Fig. 4.20b). It is located at its westernmost position in January (∼110 °W) and at its easternmost position in September-November (∼94 °W, blue line in Fig. 4.20c). Under future conditions, the intensity of the center of the SPA increases around the year by ∼2 hPa, with a maximum value in September and minimum value in May (red line in 4.20a). Regarding its position, except in July the SPA center moves towards the south (red line in 4.20b) and except in January, February, July and August, the SPA center moves towards the west (red line in 4.20c). Note that the center

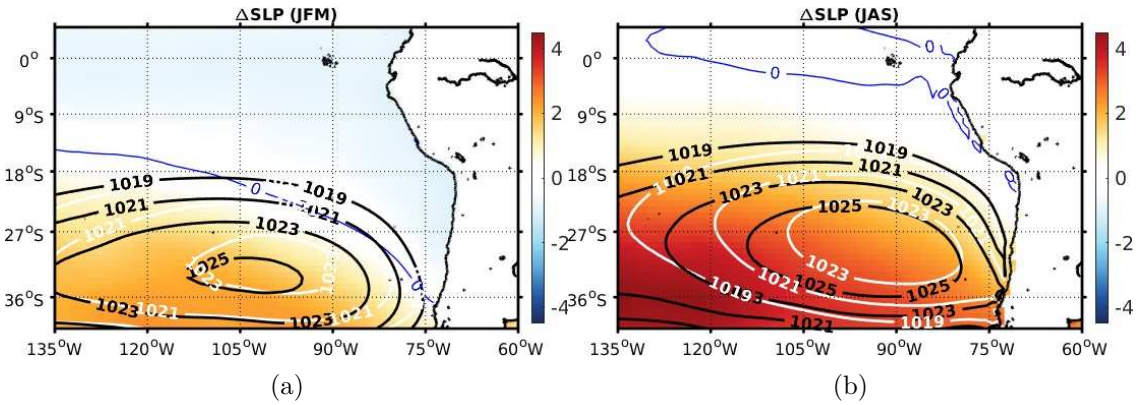

Fig. 4.19 *Mean sea level pressure in present and future conditions (white and black contours respectively) and sea level pressure change (shading) for a) summer (January-March) and b) winter (July-September). Blue lines indicate zero sea level pressure changes. Outputs from WRF105 simulations.*

of the SPA was determinated by the maximum monthly value of sea level pressure data in the 120–80 °W,20–45 °S area. These displacements and intensifications of the SPA likely have an impact on the alongshore pressure gradient and may influence the coastal winds.

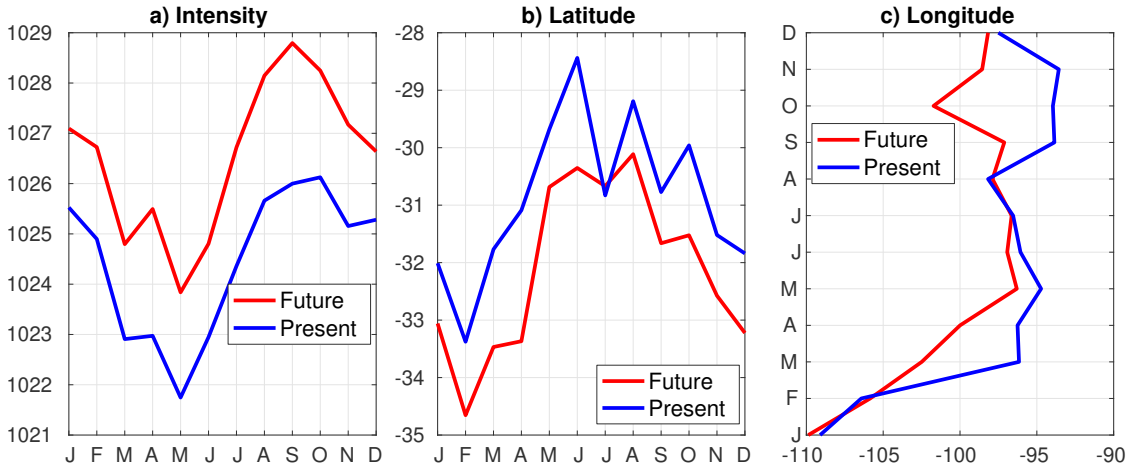

Fig. 4.20 *Climatology of the a) intensity, b) latitudinal position, and c) longitudinal position of the South Pacific Anticyclone (SPA) for present and future conditions (blue and red lines respectively).*

b) The land-sea thermal contrast

Bakun (1990) proposed that the nearshore winds in upwelling regions may increase in the future due to the increase of land-sea temperature difference. He suggested that under global warming, due to the increase of the greenhouse gases, land temperature will rise faster than ocean temperature and the pressure will decrease stronger on land, driving an enhancement of the cross-shore pressure gradient and thereby increasing the upwelling

favorable winds.

As Bakun says the land surface temperature increase more than sea surface temperature in our simulations (Fig. 4.21a), and the land sea temperature contrast increase in both summer and winter seasons (Fig. 4.21b and c). However, the sea level pressure increases on land (by 4–6 hPa; Fig. 4.22) rather than diminish, in disagreement with Bakun's hypothesis. Moreover, in spite of a decrease of winds in summer, the land-sea gradient increases, also invalidating Bakun's hypothesis in the summertime.

Note that García-Reyes et al. (2013) using reanalysis database showed that the variability in upwelling-favorable winds is dominated by oceanic atmospheric pressure systems, and only weakly influenced by terrestrial atmospheric pressure systems.

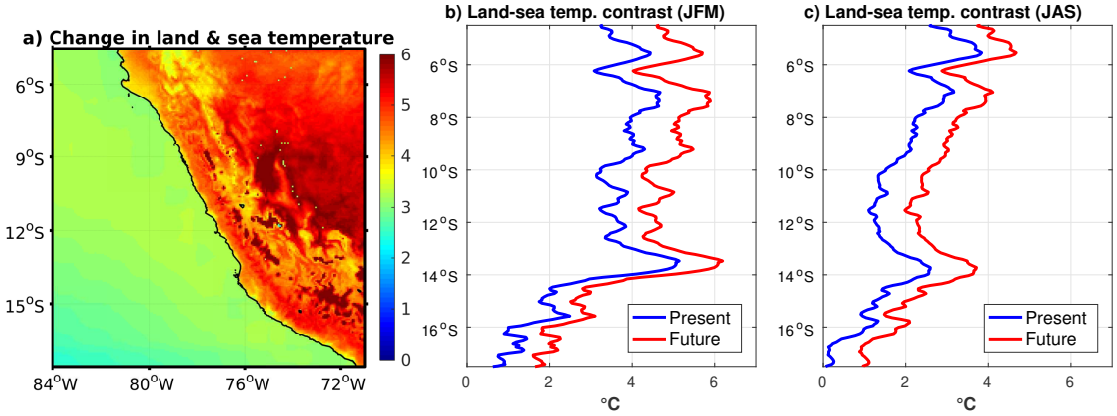

Fig. 4.21 *a) Change in land and sea surface temperature. b) Land sea temperature contrast in summer (January-March) for present and future conditions. c) Same as b) but in winter (July-September).*

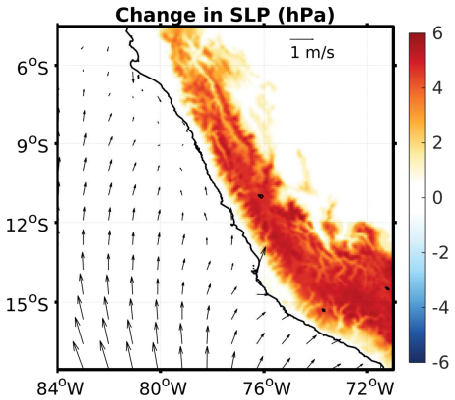

Fig. 4.22 *Change in the mean sea level pressure (in* hPa, *colors) and wind (in* $\mathrm{m\,s^{-1}}$, *vectors)*

c) Precipitation anomaly

Belmadani et al. (2014) showed that the change in surface velocity could be associated

to changes in convection in the North of Peru. Using a vorticity balance in the surface layer, they found that:

$$\beta V \approx f\frac{\partial W}{\partial z} + curl(friction)$$

with $\beta = \partial f/\partial y$ (f Coriolis parameter)>0

They showed that the changes of vorticity in the $4CO_2$ climate scenario were dominated by changes in the planetary vorticity term ($f\partial W/\partial z$), thus:

$$\Delta V \approx f\Delta(\frac{\partial W}{\partial z})$$

where $\Delta(X) = X_{4CO_2} - X_{PI}$.

As $f < 0$ and $\Delta(\partial W/\partial z) > 0$ because convection is enhanced by the warming, the ΔV is negative, thus V will decrease.

Our simulations show an increase of the precipitation (associated with a convection enhanced) in summer, but it occurs mainly near the equatorial Pacific and far from the Peru coast (Fig. 4.23a). So, its contribution on the weakening of the coastal wind in summer should not be too strong, as in the case of Belmadani et al. (2014) simulations. Note that simulations with the IPSL global model used by Belmadani et al. (2014) tipically show the overestimation of precipitation in regimes of atmospheric subsidence (Dufresne et al., 2013).

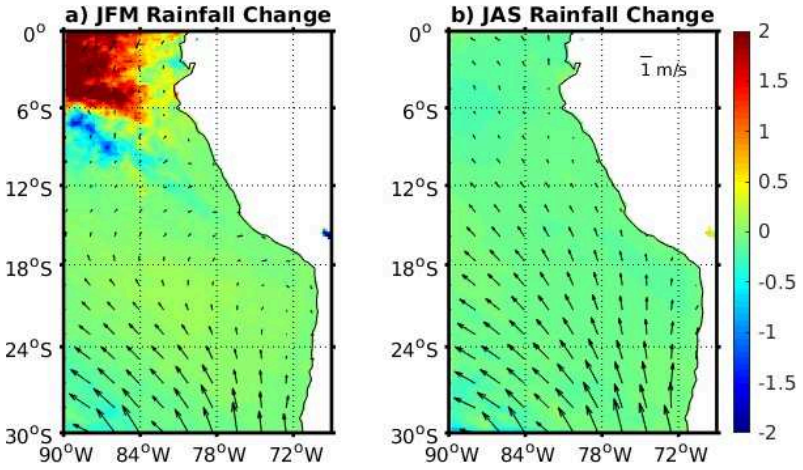

Fig. 4.23 *Change in precipitation (in* mm d^{-1}*, colors) and wind (in* m s^{-1}*, vectors) for a) summer and b) winter from WRF* 21 km.

4.3.6 El Niño wind anomalies under future conditions

In order to evaluate the impact of climate change on El Niño wind anomalies, we compared wind anomalies during the November 1997-February 1998 from WRF7 control simulation against the wind anomalies during the November 2089-February 2090 from WRF7 climate change simulation (Fig. 4.24). Note that SST anomalies are the same in both cases by construction of our future SST forcing (see section 4.2.2). Positive wind anomalies are

stronger near the coast and decrease offshore under present and future conditions (Figs. 4.24a and b respectively). The major differencens between both spatial patterns are located off the North coast where wind anomalies under future conditions are less intense that under present conditions (Figs. 4.24c).

To better understand these differences, we compared the alongshore wind anomalies from both simulations (Fig. 4.25). They show a temporal displacement and intensification of the wind anomaly peak in the Northern coast from February to April (from $\sim 1\,\mathrm{m\,s^{-1}}$ under present conditions to $\sim 1.5\,\mathrm{m\,s^{-1}}$ under future conditions) as a effect of climate change (Figs. 4.25a, b).

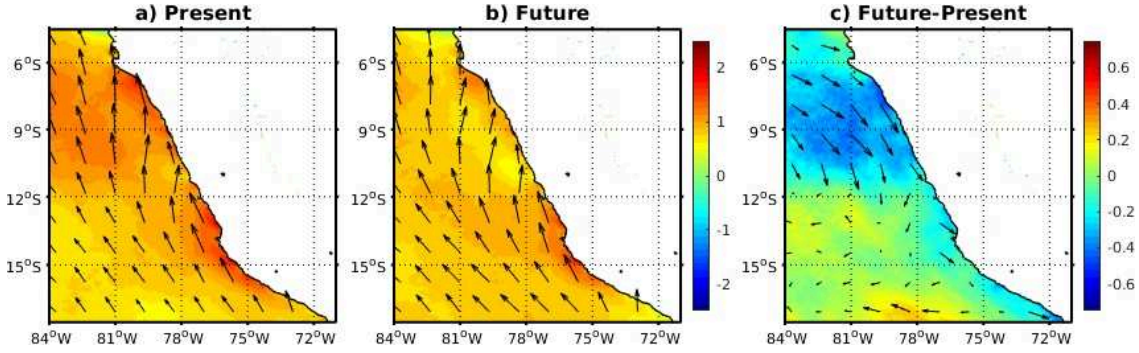

Fig. 4.24 *Mean surface wind anomalies (in* $\mathrm{m\,s^{-1}}$*) from WRF7 over El Niño conditions: a) November 1997-February 1998 and b) November 2089-February 2090 (RCP8.5 scenario). c) Differences between b and a).*

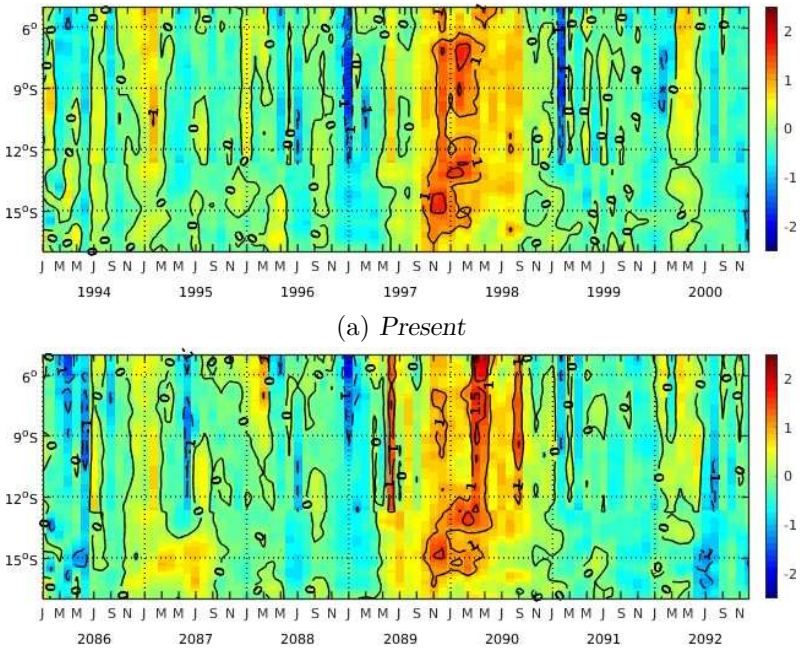

(a) *Present*

(b) *Future*

Fig. 4.25 *Time-latitude diagrams of alongshore wind anomalies from WRF7.*

In order to evaluate if the temporal displacement and increase of the 1997-1998 El Niño wind anomalies peaks observed in the high resolution WRF 7 km climate change simulation is a robust characteristic of El Niño events under future conditions, we performed two WRF simulations at 105 km of horizontal resolution for a relatively long time periods (1982-2016 for current conditions and 2074-2108 for the RCP8.5 scenario). Figure 4.26 shows time series of monthly wind anomalies averaged in a 160-km-wide coastal band and between 7–11 °C for present and future conditions (black and red lines respectively in Fig. 4.26) for five El Niño periods.

For the 1982-1983 El Niño period, the wind anomaly maximum peak in May 1982 occurs one month later (in June) under future condtions (there is also a peak intensification of $\sim 0.5\,\mathrm{m\,s^{-1}}$). For the 1987-1988 El Niño period, the peak in February 1987 increases by $\sim 0.25\,\mathrm{m\,s^{-1}}$ and the maximum peak in April 1987 occurs one month later (in May) under future conditions. While the maximum peaks for the El Niño 1991-1992 and El Niño 1997-1998 (in February 1992 and January 1998 respectively) occur two months later (in April) under future conditions. For the 2015-2016 El Niño period, the maximun peak occurs in July 2015, while the maximun peak occurs in September under future conditions. Despite the peaks displacement, there is a good correlation between future and present wind anomalies, suggesting that the interannual variability of coastal winds off Peru is mainly driven by the SST interannual variability (as we showed in chapter 3), which is exactly similar in the future and current conditions by construction in our simulation framework (see subsection 4.2.2). The differences observed between future and current El Niño wind anomalies are probably associated to differences in the regional atmospheric conditions (position of the SPA, etc.). To investigate further this aspect, running ensemble simulations to suppress the impact of the atmospheric variability could be useful.

In addition, we compared El Niño wind anomalies from WRF7, WRF21 and WRF105 to evaluate the influence of the model resolution. We found that the spatial patterns of surface wind anomalies during El Niño conditions are quite similar, with strong wind anomalies alongshore and off the North coast (Fig. 4.27). It shows that model resolution used for our study about El Niño winds (1/4°) in the previous chapter 3 was adequate for that task and the results are independent of the model resolution.

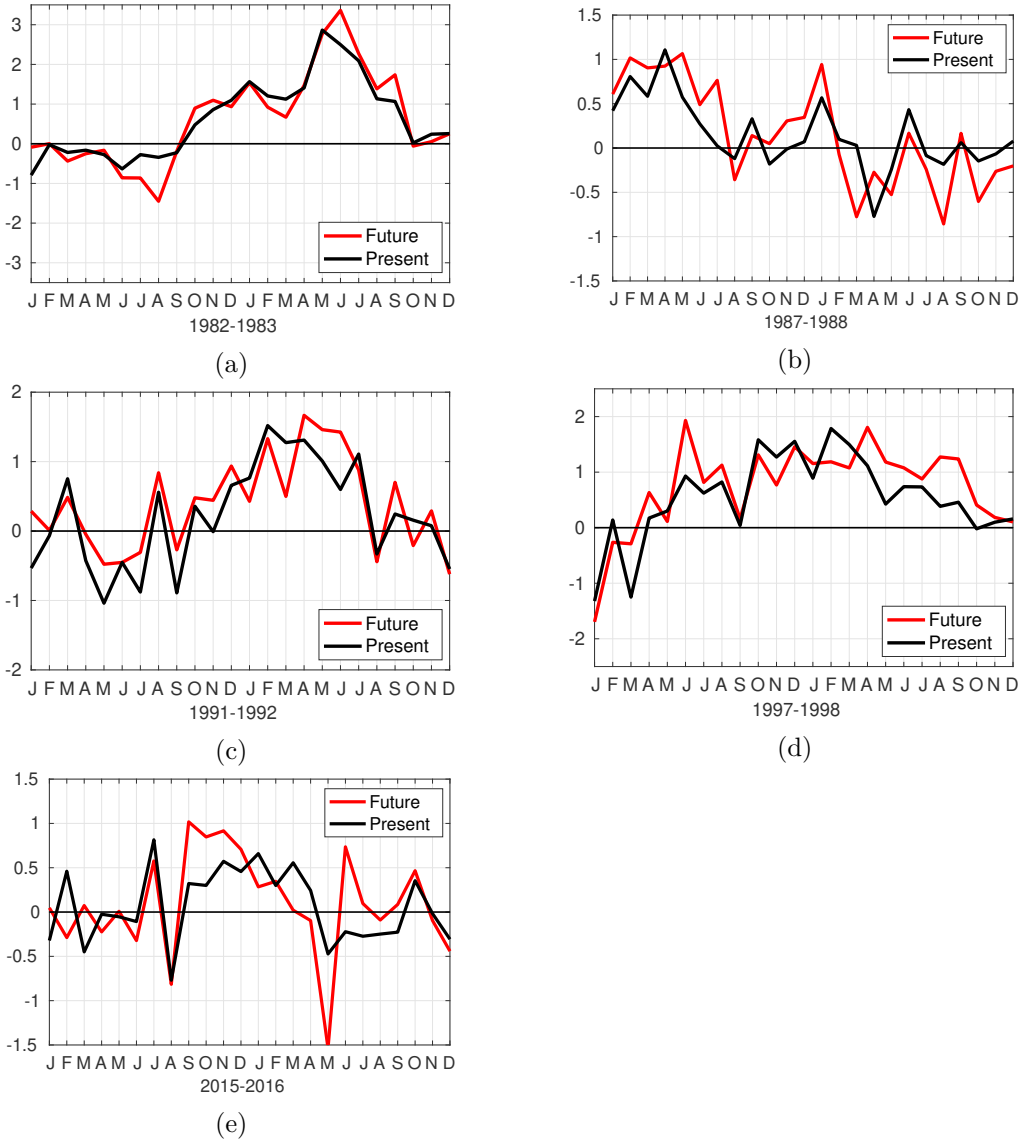

Fig. 4.26 *Time evolution of alongshore wind anomalies (in* $\mathrm{m\,s^{-1}}$*) for WRF* 105 km *in future (red line) and present (black line) conditions for five El Niño events. Anomalies were averaged in a 160-km-wide coastal band and between* 7–11 °S.

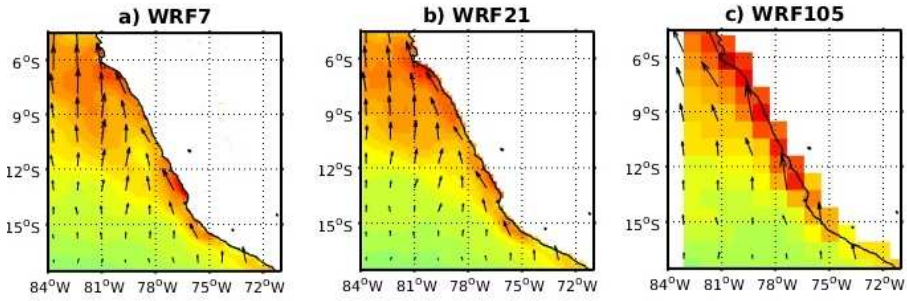

Fig. 4.27 *Mean surface wind anomalies (in* $\mathrm{m\,s^{-1}}$*) over February 2090-May 2090 (Niño conditions) from a) WRF7, b) WRF21 and c) WRF105.*

4.4 Discussion and conclusions

A high resolution regional atmospheric model is used to investigate the impact of climate change on upwelling favorable winds off the Peru coast. The WRF model is applied using three nested domains with 105, 21 and 7 km of horizontal resolution. We performed a control simulation in the period 1994-2003 forced by the NCEP2 reanalysis, and a climate change simulation where mean anomalies of the seasonal cycle from 31 CMIP5 global models are added to the NCEP2 lateral boundary conditions. The high resolution atmospheric simulation (WRF7), evaluated with satellite data, reproduced well the intensity, seasonal and interannual variability of alongshore winds, as well as the spatial variability of the mean wind drop-off near the coast. We found weak changes in the mean state of upwelling favorable winds off Peru for period 2086-2095 under the RCP8.5 scenario with respect to the control simulation. In overall, winds tend to decrease in spring-summer (∼0–5 %) and to increase in fall-winter (∼5–10 %), so that there is a slight intensification of the seasonal cycle. In particular, there is a local strong intensification of the nearshore winds in the Paracas-Pisco bay area between ∼12–14 °S during winter.

A momentum balance shows that in the whole region the pressure gradient is the dominant force driving the surface wind acceleration. Under the climate change scenario, the pressure gradient decreases in summer and increases in winter, driving the weakening and/or intensification of the winds off the coast respectively. For the nearshore region between ∼12–14 °S in the Paracas-Pisco bay area which is protected by an orographic obstacle, the advection term plays a crucial role on the wind dynamics. In this region, the total advection term increase under future conditions, mainly related to the enhancement of the meridional advection.

On the other hand, air temperature and humidity are uniformily increased in the planetary boundary layer (PBL), so that temperature inversion characteristics do not change. The turbulent vertical mixing coefficient increases in summer, but the change of the vertical mixing of momentum is negative, showing that Wallace's mechanism (enhancement of the vertical transport of momentum) may not be important at this scale in the Peru region.

The wind changes are mainly associated to changes in the intensity and position of the South Pacific Anticyclone. The decrease of the coastal winds off the Peru coast during

summer under future conditions seems to be associated to the SPA displacement towards the south despite of its intensification. In contrast the coastal winds intensification during winter seems to be linked with the SPA intensification. It suggest that changes in coastal winds off Peru are very sensitive to the changes in the position and intensity of the SPA under future conditions. 0n the other hand, model results show that the land-sea temperature contrast, which has been hypothesized to be a potential local factor to drive a coastal wind intensification in upwelling systems (Bakun, 1990), increases in spite of a decrease of coastal winds in summer, invalidating Bakun's Hypothesis in the summertime for the Peru region. In addition, our simulations show a increase of the precipitation in summer, which could contribute to the weakening of the wind during this season as was suggested by Belmadani et al. (2014), but it occurs far from the Peru coast so that its contribution on the coastal winds decrease in summer should not be too strong, as in the case of Belmadani et al. (2014). Finally, we confirm that interannual variability of the coastal winds off Peru are mainly driven by the interannual variability of the SST alongshore gradient under present and future conditions.

Our results confirm the weakening of coastal winds off Peru in summer found in previous studies (Goubanova et al., 2011; Belmadani et al., 2014), but contrast with the annual mean (Table 4.1). Note that the wind decrease in summer is important for biogeochemistry because the summer season is the most productive season and the availability of nutrients controls the intensity of surface productivity (Echevin et al., 2008). Thus regional climate change may induce a less productive summer season. The discrepancies among these studies may come from specific differences in the projected change of the position and intensity of the SPA.

Reference	Model (and scenarios)	Resolution	Period		Wind response		
			Future	Present	Annual mean	summer	winter
Goubanova et al. (2011)	CMIP3 ($2CO_2$ and $4CO_2$)	50 km	2120-2149	1970-1999	↓ (5-10%)	↓ (5-10%)	→
Belmadani et al. (2014)	CMIP3 ($2CO_2$ and $4CO_2$)	50 km	2079-2099	1979-1999	↓ (10-20%)	↓ (20-30%)	↓ (5-10%)
This study	CMIP5 (RCP8.5)	7 km	2086-2095	1994-2003	→	↓ (0-5%)	↑ (5-10%)

Table 4.1 – Characteristics and results of previous climate change studies of coastal winds off Peru.

A potential limitation of our results is that anomalies of the SST seasonal cycle from the CMIP5 multi-model mean at lower resolution (∼1 degree) were linearly extrapolated in the nearshore region to force our high resolution atmospheric climate change simulation. It could introduce unrealistic SST patterns that could impact the coastal wind (Oerder et al., 2015). Moreover, another potential limitation of our study is that our forced atmospheric simulations cannot take into account the retroaction of the atmosphere on the ocean, which could modify the nearshore surface temperature. So, ocean-atmosphere coupled simulations could be needed to study with better precision the impact of climate change in nearshore regions.

Chapter 5

Conclusions and perspectives

This thesis examined the coastal wind dynamics in the Peruvian upwelling system under two very different warming conditions: interannual El niño event and long term warming in a climate change scenario. It allowed to improve the knowledge of the key mechanisms governing the coastal wind dynamics during El Niño events and under current and future climate scenarios. For this purpose, the Weather Research and Forecasting (WRF) model was configured for the Peru region as a regional climate model in terms of domain size, physical parameterization and lateral boundary conditions (Chapter 2).

In this chapter of the thesis, a summary of the main conclusions is provided for both studies on El Niño and climate change, as well as some pespectives for future works.

5.1 Coastal winds during El Niño events

In the first part of this thesis (Chapter 3), we studied the physical processes driving the coastal wind intensification observed during El Niño 1997-1998 in the Peruvian upwelling system. We performed a WRF simulation at a resolution of 1/4° in the period 1994-2000. It allowed to reproduce the alongshore wind anomalies observed off the Peru coast during 1997-1998 El Niño event. Our analysis showed that:

- The alongshore pressure gradient anomalies drove the alongshore wind anomalies during El Niño period. They were mainly balanced by the vertical turbulent mixing anomalies (friction at the surface).
- The alongshore pressure gradient anomalies were generated by the stronger heating of the air column in the north than in the south, which was forced by the inhomogeneous warming of the SST along the Peru coast during El Niño event.
- A mechanism compensating the surface pressure gradients (so-called "back-pressure effect") was strong in the case of a marked temperature inversion above the PBL during part of the event. In contrast, a weak temperature inversion allowed shallow convection to develop without triggering any "back-pressure effect" in the rest of the event.
- It is likely that two conditions are needed to drive a strong wind anomalies during El Niño in the Peru coastal region: a SST anomaly alongshore gradient and a weak

or absent temperature vertical inversion.

- Our results suggest that an increase of the land–sea thermal gradient may not play a strong dynamical role for the alongshore wind during El Niño, in contrast to the so-called "Bakun's hypothesis".

In addition, we performed two sensitivity experiments to study the respective roles of large scale atmospheric signal and of the SST local forcing in driving the wind anomalies during El Niño. They confirmed that the coastal wind intensification was primarily driven by the local SST forcing, whereas large scale variability associated with the South Pacific Anticyclone modulated its effects.

Examination of other El Niño events over the period 1979-2016 using reanalysis data confirmed that intensifications of alongshore wind off Peru were associated with SST alongshore gradient anomalies, as during the 1997–1998 event.

5.1.1 El Niño winds feedback on ocean dynamics

As Kessler (2006) suggested, El Niño events are an example of winds forcing the ocean in one place (the westerly wind bursts in the western Pacific Ocean), oceanic Kelvin waves carrying the signal in thermocline depth across thousands of kilometers (eastward to the eastern equatorial Pacific), thus changing the SST remotely (anomalous SST gradient northward), which then feeds back to modify the winds in the distant location (winds off the Peru coast). In addition, the nearshore wind increase off Peru during an El Niño event produces a strong Ekman pumping in the ocean (i.e. downward velocity; Fig. 5.1) which contributes to deepen the thermocline and enhances the ocean warming in addition to the one produced by the downwelling Kelvin wave (Thomas et al., 2001). It would be interesting to study the response of the ocean forced by the El Niño-related wind anomalies. We could examine the upwelling response by evaluating the role of the wind spatial modifications during El Niño (e.g. Halpern (2002)) and the role of the horizontal advection due to El Niño poleward currents near the coast. To do so, we could use a regional ocean model (ROMS) forced by the WRF wind fields produced in chapter 3.

5.1.2 The "coastal El Niño" dynamics

Coastal El Niño events are defined as such when warm conditions are encountered near the coasts of Peru whereas cold-to-neutral conditions are found in the central equatorial pacific. Such events are scarce but have been encountered in 1891, 1925 and recently in summer 2017 (Takahashi and Martínez, 2017; Garreaud, 2018; Echevin et al., 2018). The behaviour of the ocean atmosphere system during the local warming "coastal El Niño" is different from "canonical" El Niño events. Indeed, northerly wind anomalies were observed during these events (Fig. 5.2, Fig 5.3a), in contrast to the well known upwelling-favorable southerly wind anomalies observed during the 'canonical" El Niño events. As in our previous study of the 1997-1998 El Niño, we could use the WRF model to study the wind dynamics during the local warming "coastal El Niño" and then use it to isolate the impact of the different effects (wind decrease, wind stress curl, etc.) on the ocean warming.

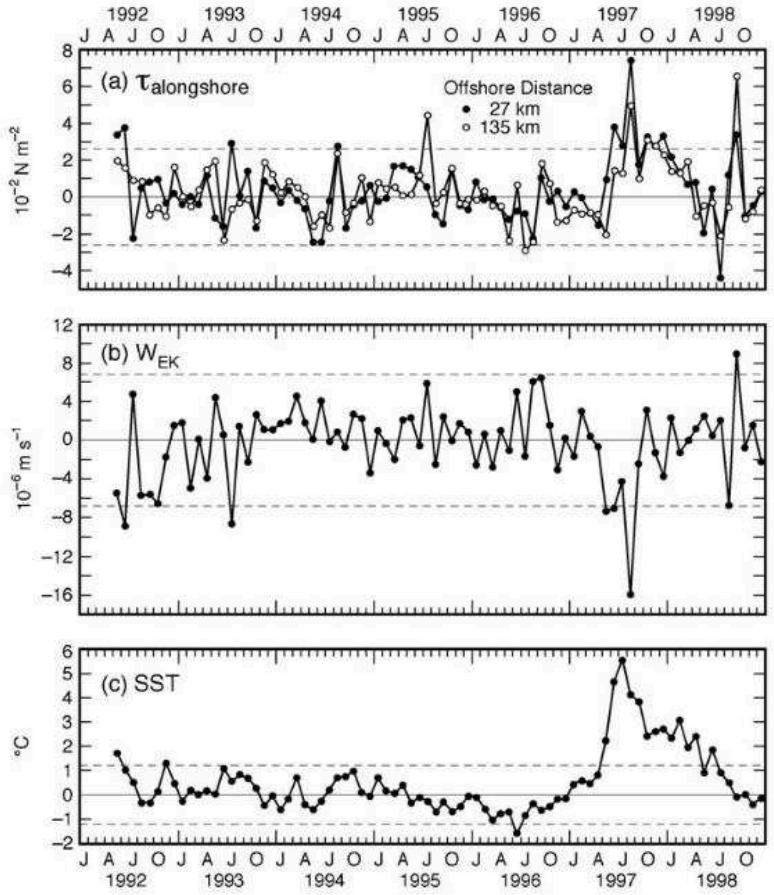

Fig. 5.1 *Monthly mean anomalies of a) alongshore wind stress, b) Ekman pumping/suction, and c) sea surface temperature (Halpern, 2002).*

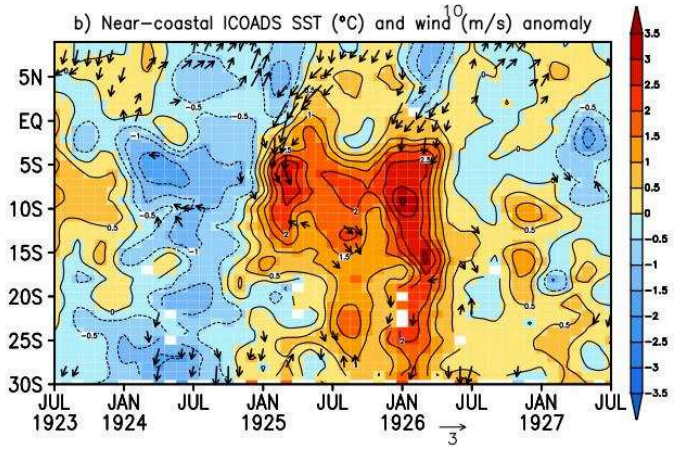

Fig. 5.2 *Monthly sea surface temperature (shading, °C) and surface wind ($m\,s^{-1}$) anomalies from ICOADS (Takahashi and Martínez, 2017).*

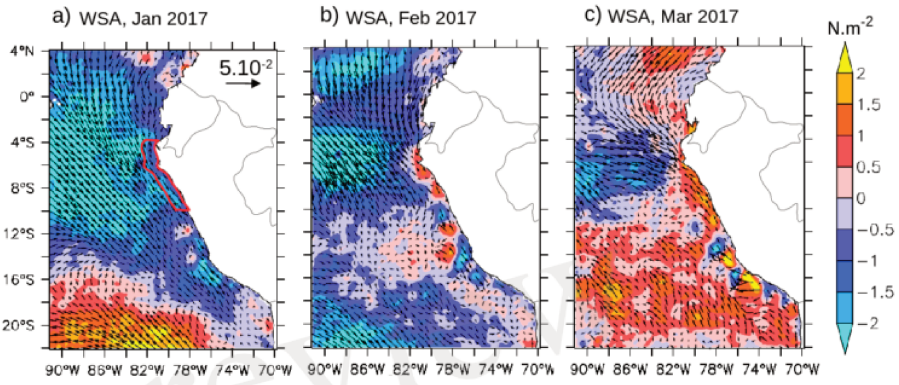

Fig. 5.3 *ASCAT monthly mean wind stress anomalies (in* $\mathrm{N\,m^{-2}}$*) in 2017: a) January, b) February, c) March. Anomalies were computed with respect to a climatology over 2013-2016 (Echevin et al., 2018).*

5.2 Climate change impact on coastal winds

In the second part of this thesis (Chapter 4), we studied the future changes in coastal winds in the Peruvian upwelling system by analysing a very high resolution (7 km) WRF simulations for historical and RCP8.5 climate scenario that realistically simulates the nearshore wind characteristics, such as the wind drop-off. For the historical simulation, the WRF model is used to directly downscale the NCEP2 reanalysis data within the period 1994-2003. For the assessment of possible future changes, we perturbed the lateral boundary conditions of NCEP2 with climate anomalies of the seasonal cycle from the CMIP5 Multi Model Mean (generated from 31 CMIP5 climate models). The results showed that:

- The mean state of the winds over the Peruvian upwelling system shows weak changes (<5%) in a period corresponding to 2086-2095 of the RCP8.5 scenario.
- The alongshore winds tend to decrease in spring-summer (∼0–5 %) and to increase in fall-winter (∼5–10 %), so that there is a slight intensification of the seasonal cycle.
- A momentum balance in current conditions showed that the pressure gradient and the vertical turbulent mixing are the dominant forces that drive the nearshore wind dynamics along the Peru coast, except between ∼12–14 °S (in the Pisco bay) where the advection term plays a important role in the momentum budget.
- The change in the momentum budget showed that the pressure gradient decrease (increase) drive the weakening (intensification) of the coastal wind in summer (winter) under future conditions, except between ∼12–14 °S where the relative strong intensification of local wind in winter is mainly driven by the cross-shore advection.
- Diagnostics about the change in sea level pressure showed that the changes in the pressure gradient off Peru coast are very sensitive to the change in both the intensity and position of the South Pacific Anticyclone.

- The land-sea thermal contrast increases under future conditions due to greater heat capacity of the ocean than the land. However, the wind decreases in summer, invalidating Bakun's hypothesis in the summertime.
- Model simulation showed an increase of precipitation off northern Peru in summer. This could also contribute to the weakening of the southerly wind in summer, as suggested by Belmadani et al. (2014).

5.2.1 Pespectives on additional regional downscaling

Given that the change in nearshore winds off Peru could be very sensitive to the change in position and intensity of the SPA, it should be taken into account when the wind projection of individual global models are examined. For example while coastal wind is projected to decrease in the IPSL-CM5 and CNRM-CM5 models (∼10–15 %), no change is projected with the GFDL-ESM2M model (Fig. 5.4). It suggests that additional regional downscaling of different large grid-scale climate models could be needed to improve the consensus on the projections of the wind in the Peruvian upwelling system for the end of the 21st century. In addition, it would be interesting to study the regional impact of climate change on coastal winds off Peru in a near future (e.g. the period 2020-2030).

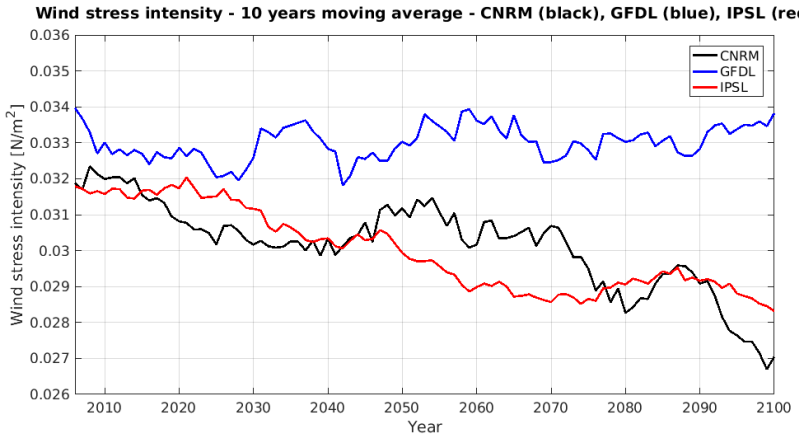

Fig. 5.4 *Mean wind stress intensity in a coastal box off Peru from IPSL-CM5A, CNRM-CM5 and GFDL-ESM2M global models (Gévaudan et al., 2018)-.*

5.2.2 Regional oceanic climate change scenarios

One motivation for this study was the possibility to produce high resolution atmospheric forcing to run regional oceanic models simulations. It will allow to produce regional oceanography climate change scenarios to estimate the impact of the global warming on the upwelling and regional circulation in the Peruvian upwelling system.

A few studies (Echevin et al., 2012; Oerder et al., 2015; Gévaudan et al., 2018) on dynamical downscaling of ocean climate scenarios from some global models (IPSL-CM4, IPSL-CM5, CNRM-CM5, GFDL-ESM2M) were performed using the ROMS regional ocean circulation model for the Peru upwelling system with different types of wind products. Echevin et al. (2012) used surface winds statistically downscaled from outputs of

the global model IPSL-CM4 performed by Goubanova et al. (2011) under quadrupling CO_2 scenario. Oerder et al. (2015) used downscaled surface winds from the LMDz model with increased horizontal resolution in the Peru-Chile upwelling system performed by Belmadani et al. (2014) under $2CO_2$ and $4CO_4$ scenario. Gévaudan et al. (2018) used QuikSCAT satellite winds perturbed by CMIP5 models without downscaling. They found a surface ocean warming of 3–4 °C (quite similar to the SST anomalies in the global model run, see Figure 5.5) and a reduction in upwelling intensity off Peru associated with the reduction of the alongshore winds, as well as an intensification of the poleward coastal undercurrent (PCUC), a shoaling of the equatorward surface coastal Peru-Chile current (PCC) and the strengthening of the mesoscale eddy activity when regional warming increases.

Similarly, it would be interesting to study the impact of the future winds downscaled using WRF on the ocean circulation. More precisely we suggest to do two ocean simulations: one forced by ocean boundary conditions from some reanalysis product (e.g. SODA; Carton and Giese (2008)) over the period 1994-2003 (same as our control atmospheric run) and by the WRF 7 km control run (1994-2003), and other forced by renalysis ocean boundary conditions plus ocean boundaries anomalies from CMIP5 multi model mean and by the WRF 7 km RCP8.5 simulation. By following this protocol, we would be fully consistent with the regional atmospheric simulations. Furthermore, it would be intersting to see how these simulations would contrast with the ocean simulations of Echevin et al. (2012), Oerder et al. (2015) and Gévaudan et al. (2018).

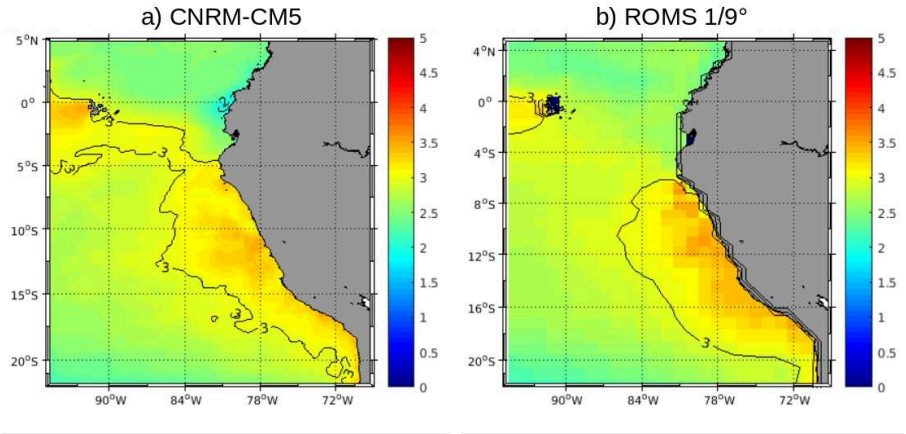

Fig. 5.5 *SST change between the periods 2091-2100 and 2006-2015 from a) CNRM-CM5 model and b) ROMS model (Gévaudan et al., 2018).*

5.2.3 High resolution atmosphere and ocean climate modelling

Understanding of the ocean dynamics in shallow regions of the Peruvian shelf and coastal embayments is still limited. As scatterometer winds have a blind zone near the coast, atmospheric high resolution outputs from WRF simulations for the present conditions could also be used to force ocean models to study the oceanic circulation at much smaller scale. For example, this could be done in the highly productive Paracas-Pisco bay (Fig. 5.6), where the wind surface has a different variability (e.g. seasonal cycle) than out

of the bay where the typical upwelling seasonal cycle occurs, and also in other coastal embayments where orographic obstacles are going to play a role (e.g. in the Shechura bay). Understanding the dynamics of these regions is extremely important because of their social and economic implications through artisanal fisheries, aquaculture in coastal embayments, contamination due to industrial waste, etc.

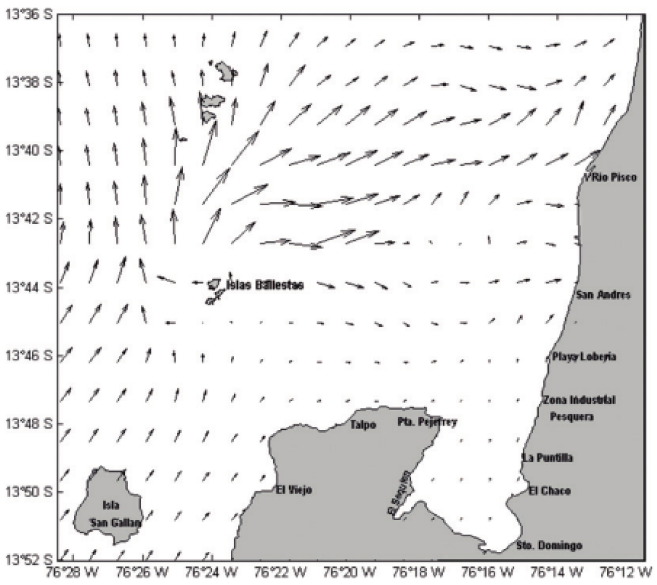

Fig. 5.6 *The distribution of sea surface wind in the Paracas Bay from in-situ observations for October 2013 (Morón et al., 2017).*

5.2.4 Regional coupled ocean/atmosphere model

The impact of the regional air-sea coupling over the Peru region is a relatively new research topic. Oerder et al. (2016) used model and observations to show that coupling between mesoscale sea surface temperature and wind stress intensity is strong in the Peru region (Fig. 5.7). Moreover, Oerder et al. (2018) used a high-resolution regional ocean–atmosphere coupled model and showed that the mesoscale activity is strongly reduced when the effect of the surface ocean current on the wind stress is taken into account.

On one hand, regional atmospheric models use a SST forcing which usually comes from the large scale ocean models (e.g. Belmadani et al. (2014) and this study) and thus do not resolve correctly the nearshore SST gradients. On the other hand, regional oceanic models use atmospheric forcing which usually come from the large scale atmospheric models and thus do not resolve correctly the nearshore wind drop-off. Under these forced framework models, the impact of the regional air-sea coupling is not considered. We suggest to develop and run a regional coupled ocean/atmosphere model to take into account the ocean/atmosphere local interactions and their impact on the dynamics of the lower atmosphere and the near-surface ocean under present and future conditions.

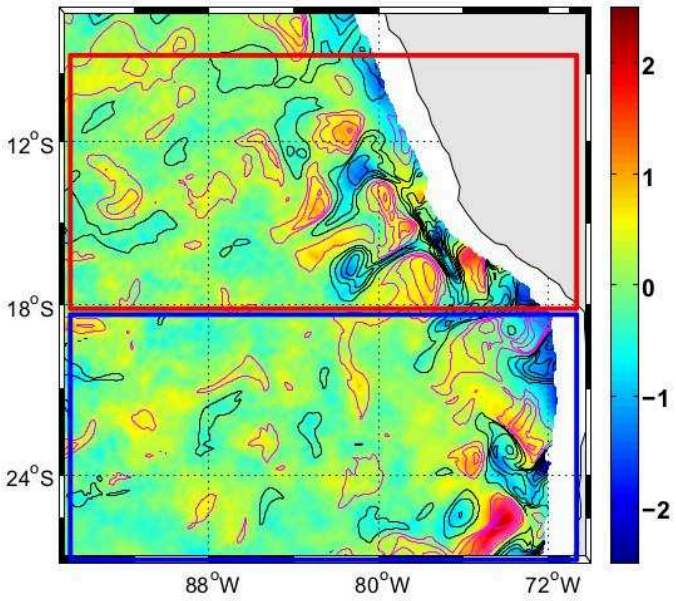

Fig. 5.7 *Surface wind stress mesoscale anomalies* ($10^{-2}\,\mathrm{N\,m^{-2}}$, *colors) and sea surface temperature anomalies* (°C, *contours). Fields are from a WRF-NEMO simulation and time-averaged over July 2007 (Oerder et al., 2016).*

Bibliography

Ancapichun, S., Garcés-Vargas, J., 2015. Variability of the Southeast Pacific Subtropical Anticyclone and its impact on sea surface temperature off north-central Chile. Ciencias Marinas 41 (1), 1–20.
URL http://cienciasmarinas.com.mx/index.php/cmarinas/article/view/23383

Bakun, A., 1990. Global climate change and intensification of coastal ocean upwelling. Science 247 (4939), 198–201.
URL http://www.ncbi.nlm.nih.gov/pubmed/17813287 14, 16, 18, 111, 118

Bakun, A., Weeks, S. J., 2008. The marine ecosystem off Peru: What are the secrets of its fishery productivity and what might its future hold? Progress in Oceanography 79 (2-4), 290–299.
URL http://dx.doi.org/10.1016/j.pocean.2008.10.027 8, 15

Barber, R. T., Chavez, F. P., 1983. Biological consequences of El Niño. Science 222, 1203–1210. 6

Battisti, D. S., Hirst, A. C., 1989. Interannual variability in a tropical atmosphere-ocean model: Influence of the basic state, ocean geometry and nonlinearity. Journal of the Atmospheric Sciences 46, 1687–1712. 6

Bayer, A. M., Danysh, H. E., Garvich, M., Gonzálvez, G., Checkley, W., Alvarez, M., Gilman, R. H., 2014. The 1997–1998 El Niño as an unforgettable phenomenon in northern Peru: a qualitative study. Disasters 38, 351–374. 6

Belmadani, A., Echevin, V., Codron, F., Takahashi, K., Junquas, C., 2014. What dynamics drive future wind scenarios for coastal upwelling off Peru and Chile? Climate Dynamics 43 (7-8), 1893–1914. 16, 17, 42, 95, 104, 112, 113, 118, 123, 124, 125

Bentamy, A., Fillon, D. C., 2012. Gridded surface wind fields from Metop / ASCAT measurements. International Journal of Remote Sensing 33 (6), 1729–1754. 99

Bjerknes, J., 1969. Atmospheric teleconnections from the equatorial pacific. Monthly Weather Review 97 (3), 163–172. 5

Boé, J., Hall, A., Colas, F., McWilliams, J. C., Qu, X., Kurian, J., Kapnick, S. B., 2011. What shapes mesoscale wind anomalies in coastal upwelling zones? Climate Dynamics 36 (11-12), 2037–2049. 4, 104

Bretherton, C., Uttal, T., Fairall, C., Yuter, S., Weller, R., Baumgardner, D., Comstock, K., Wood, R., Raga, G., 2004. The epic 2001 stratocumulus study. Bulletin of the American Meteorological Society 85 85, 967–977. 1

Bretherton, C. S., Wood, R., George, R. C., Leon, D., Allen, G., Zheng, X., 2010. Southeast pacific stratocumulus clouds, precipitation and boundary layer structure sampled along 20s during VOCALS-REx. Atmospheric Chemistry and Physics 10 (21), 10639–10654. 4

Capet, X. J., Marchesiello, P., McWilliams, J. C., 2004. Upwelling response to coastal wind profiles. Geophysical Research Letters 31 (13), 1–4. 4, 42, 89, 99

Capotondi, A., Wittenberg, A. T., Newman, M., Lorenzo, E. D., Yu, J. Y., Braconnot, P., Yeh, S. W., 2015. Understanding ENSO diversity. Bulletin of the American Meteorological Society 96, 921–938. 5

Carter, T., La Rovere, E., Jones, R., Leemans, L., Nakicenovic, N., Pittock, A., Semenov, S., Skea, J., 2001. Developing and applying scenarios. climate change 2001: Impacts, adaptation, and vulnerability. contribution of working group II to the third assessment report of the intergovernmental panel on climate change. Tech. Rep. 145-190, Cambridge University Press, Cambridge. 9

Carton, J. A., Giese, B. S., 2008. A reanalysis of ocean climate using simple ocean data assimilation (SODA). Mon. Weather Rev. 136, 2999–3017. 124

Chavez, F. P., Bertrand, A., Guevara-Carrasco, R., Soler, P., Csirke, J., 2008. The northern Humboldt Current System: Brief history, present status and a view towards the future. Progress in Oceanography 79 (2-4), 95–105. 2

Chavez, F. P., Ryan, J., Lluch-Cota, S. E., Niquen, M. C., 2003. From Anchovies to Sardines and back: Multidecal Change in the Pacific Ocean. Science. 7

Chen, F., Dudhia, J., 2001. Coupling an advanced land surface hydrology model with the penn state-NCAR MM5 modeling system. Part II: Preliminary model validation. Mon Weather Rev 129 (4), 587–604. 28

Chou, M.-D., Suarez, M. J., 1994. Tech. Rep. 104606, NASA Tech. Memo. 27

Colas, F., Capet, X., McWilliams, J. C., Shchepetkin, A., 2008. 1997-1998 El Niño off Peru: A numerical study. Progress in Oceanography 79 (2-4), 138–155.
URL http://dx.doi.org/10.1016/j.pocean.2008.10.015 8

Covey, C., AchutaRao, K. M., Cubasch, U., Jones, P., Lambert, S. J., Mann, M. E., Phillips, T. J., Taylor, K. E., 2003. An overview of results from the Coupled Model Intercomparison Project. Global and Planetary Change 37 (1-2), 103–133. 10

Cushing, D., 1990. Plankton production and year class strength in fish populations: an update of the match/mismatch hypothesis. Advances in Marine Biology 26, 250–294. 1

Dee, D. P., Uppala, S. M., Simmons, A. J., Berrisford, P., Poli, P., Kobayashi, S., Andrae, U., Balmaseda, M. A., Balsamo, G., Bauer, P., Bechtold, P., Beljaars, A. C., van de Berg, L., Bidlot, J., Bormann, N., Delsol, C., Dragani, R., Fuentes, M., Geer, A. J., Haimberger, L., Healy, S. B., Hersbach, H., Hólm, E. V., Isaksen, L., Kållberg, P., Köhler, M., Matricardi, M., Mcnally, A. P., Monge-Sanz, B. M., Morcrette, J. J., Park, B. K., Peubey, C., de Rosnay, P., Tavolato, C., Thépaut, J. N., Vitart, F., 2011. The ERA-Interim reanalysis: Configuration and performance of the data assimilation system. Quarterly Journal of the Royal Meteorological Society 137 (656), 553–597. 21

Dudhia, J., 1989. Numerical study of convection observed during the winter monsoon experiment using a mesoscale two-dimensional model. J Atmos Sci 46. 27

Dufresne, J. L., Foujols, M. A., Denvil, S., Caubel, A., Marti, O., Aumont, O., Balkanski, Y., Bekki, S., Bellenger, H., Benshila, R., Bony, S., Bopp, L., Braconnot, P., Brockmann, P., Cadule, P., Cheruy, F., Codron, F., Cozic, A., Cugnet, D., de Noblet, N., Duvel, J. P., Ethé, C., Fairhead, L., Fichefet, T., Flavoni, S., Friedlingstein, P., Grandpeix, J. Y., Guez, L., Guilyardi, E., Hauglustaine, D., Hourdin, F., Idelkadi, A., Ghattas, J., Joussaume, S., Kageyama, M., Krinner, G., Labetoulle, S., Lahellec, A., Lefebvre, M. P., Lefevre, F., Levy, C., Li, Z. X., Lloyd, J., Lott, F., Madec, G., Mancip, M., Marchand, M., Masson, S., Meurdesoif, Y., Mignot, J., Musat, I., Parouty, S., Polcher, J., Rio, C., Schulz, M., Swingedouw, D., Szopa, S., Talandier, C., Terray, P., Viovy, N., Vuichard, N., 2013. Climate change projections using the IPSL-CM5 Earth System Model: From CMIP3 to CMIP5. Vol. 40. 113

Dutheil, C. M., Bador, M., Lengaigne, M., Lefevre, J., Jourdain, N., Vialard, J., Jullien, S., Peltier, A., Menkes, C., 2018. Impact of surface temperature biases on climate change projections of the South Pacific Convergence Zone, submitted to Climate Dynamics. 96

Echevin, V., Aumont, O., Ledesma, J., Flores, G., 2008. The seasonal cycle of surface chlorophyll in the peruvian upwelling system: A modelling study. Progress In Oceanography 79, 167–176. 118

Echevin, V., Colas, F., Espinoza-Morriberon, D., Anculle, T., Vasquez, L., Gutierrez, D., 2018. Forcings and evolution of the 2017 coastal El Niño off Northern Peru and Ecuador, submitted to Frontiers in Marine Science. 120, 122

Echevin, V., Goubanova, K., Belmadani, A., Dewitte, B., 2012. Sensitivity of the Humboldt Current system to global warming: A downscaling experiment of the IPSL-CM4 model. Climate Dynamics 38 (3-4), 761–774. 123, 124

Enfield, D. B., 1981. Thermally driven wind variability in the planetary Boundary layer above Lima, Peru. J Geophys Res 86 (80), 2005–2016. 8, 90

Espinoza-Morriberón, D., Echevin, V., Colas, F., Tam, J., Ledesma, J., Vásquez, L., Graco, M., 2017. Impacts of El Niño events on the Peruvian upwelling system productivity. Journal of Geophysical Research: Oceans 122 (7), 5423–5444. 6

Falvey, M., Garreaud, R. D., 2009. Regional cooling in a warming world: Recent temperature trends in the southeast Pacific and along the west coast of subtropical South America (1979-2006). Journal of Geophysical Research Atmospheres 114 (4), 1–16. 15

Fréon, P., Barange, M., Arístegui, J., 2009. Eastern Boundary Upwelling Ecosystems: Integrative and comparative approaches. Progress in Oceanography 83 (1-4), 1–14. 1

García-Reyes, M., Sydeman, W. J., Black, B. A., Rykaczewski, R. R., Schoeman, D. S., Thompson, S. A., Bograd, S. J., 2013. Relative influence of oceanic and terrestrial pressure systems in driving upwelling-favorable winds. Geophysical Research Letters 40 (19), 5311–5315. 112

Garreaud, R., Falvey, M., 2008. The coastal winds off western subtropical south america in future climate scenarios. International Journal of Climatology. 15

Garreaud, R. D., 2018. Short Communication A plausible atmospheric trigger for the 2017 coastal El Niño (January 2017). 120

Goubanova, K., Echevin, V., Dewitte, B., Codron, F., Takahashi, K., Terray, P., Vrac, M., 2011. Statistical downscaling of sea-surface wind over the Peru-Chile upwelling region: Diagnosing the impact of climate change from the IPSL-CM4 model. Climate Dynamics 36 (7), 1365–1378. 15, 16, 17, 95, 118, 124

Gutiérrez, D., Bouloubassi, I., Sifeddine, A., Purca, S., Goubanova, K., Graco, M., Field, D., Méjanelle, L., Velazco, F., Lorre, A., Salvatteci, R., Quispe, D., Vargas, G., Dewitte, B., Ortlieb, L., 2011. Coastal cooling and increased productivity in the main upwelling zone off Peru since the mid-twentieth century. Geophysical Research Letters 38 (7), 1–6. 15

Gévaudan, M., Colas, F., Echevin, V., Espinoza-Morriberón, D., Tam, J., Gutierrez, D., 2018. Changes in the Peruvian upwelling system under future climate scenarios. Symposium: The Effects of Climate Change on the World's Ocean. 123, 124

Halpern, D., 2002. Offshore Ekman transport and Ekman pumping off Peru during the 1997-1998 El Niño. Geophysical Research Letters 29 (5), 19–1–19–4.
URL http://doi.wiley.com/10.1029/2001GL014097 120, 121

Hashizume, H., Xie, S. P., Fujiwara, M., Shiotani, M., Watanabe, T., Tanimoto, Y., Liu, T. W., Takeuchi, K., 2002. Direct observations of atmospheric boundary layer response to SST variations associated with tropical instability waves over the eastern equatorial Pacific. Journal of Climate 15 (23), 3379–3393. 42

Hong, S., Lim, J., 2006. The wrf single-moment 6-class microphysics scheme (wsm6). J Korean Meteorol Soc 42 (2), 129–151. 28

Iacono, M. J., Delamere, J. S., Mlawer, E. J., Shephard, M. W., Clough, S. A., Collins, W. D., 2008. Radiative forcing by long–lived greenhouse gases: Calculations with the aer radiative transfer models. J. Geophys. Res. 113. 28

Janjic, Z., 1994. The step-mountain eta coordinate model: further developments of the convection, viscous sublayer, and turbulence closure schemes. Mon Wea Rev 122, 927–945. 28

Kanamitsu, M., Ebisuzaki, W., Woollen, J., Yang, S.-K., Hnilo, J. J., Fiorino, M., Potter, G. L., 2002. NCEP–DOE AMIP-II Reanalysis (R-2). Bulletin of the American Meteorological Society 83 (11), 1631–1644.
URL http://journals.ametsoc.org/doi/10.1175/BAMS-83-11-1631 21

Kessler, W. S., 2006. The circulation of the eastern tropical Pacific: A review. Progress in Oceanography 69 (2-4), 181–217. 8, 14, 41, 120

Klein, S. A., Hartmann, D. L., 1993. The seasonal cycle of low stratiform clouds. 4

Lu, J., Vecchi, G. A., Reichler, T., 2007. Expansion of the Headley cell under global warming. Geophysical Research Letters 34 (6), L06805.
URL http://doi.wiley.com/10.1029/2006GL028443 14

McPhaden, M. J., 1999. Genesis and Evolution of the 1997-98 El Niño. Science 283 (5404), 950–954. 5

Mechoso, C. R., Wood, R., Weller, R., Bretherton, C. S., Clarke, A. D., Coe, H., Fairall, C., Farrar, T., Feingold, G., Garreaud, R., Grados, C., McWilliams, J., De Szoeke, S. P., Yuter, S. E., Zuidema, P., 2014. Ocean-cloud-atmosphere-land interactions in the southeastern pacific. Bulletin of the American Meteorological Society 95 (3), 357–375. 1, 3

Miranda, P. M., Alves, J. M., Serra, N., 2013. Climate change and upwelling: Response of Iberian upwelling to atmospheric forcing in a regional climate scenario. Climate Dynamics 40 (11-12), 2813–2824. 18

Mlawer, E., Taubman, S., Brown, P., Iacono, M., Clough, S., 1997. Radiative transfer for inhomogeneous atmosphere: RRTM, a validated correlated-k model for the longwave. J Geophys Res 102 (D14), 16663–16682. 28

Morón, O., Quispe, J., Lorenzo, A., Flores, G., Sánchez, S., Aronés, K., Solís, J. Quipuzcoa, L., 2017. Characterization of the physical, chemical, biological and sedimentological processes in the Ballestas and Chincha islands. 2013. Inf Inst Mar Perú 44 (4), 472–506. 125

Muñoz, R. C., Garreaud, R., 2005. Dynamics of the Low-Level Jet off the West Coast of Subtropical South America. Monthly Weather Review 133 (12), 3661–3677.
URL http://journals.ametsoc.org/doi/abs/10.1175/MWR3074.1 42

Nakanishi, M., Niino, H., 2009. Development of an improved turbulence closure model for the atmospheric boundary layer. J Meteorol Soc Jpn 87, 895–912. 28

Narayan, N., Paul, A., Mulitza, S., Schulz, M., 2010. Trends in coastal upwelling intensity during the late 20th century. Ocean Science 6 (3), 815–823. 15

Oerder, V., 2016. Interactions couplées océan-atmosphère à méso-échelle dans le pacifique sud-est. Ph.D. thesis, Sciences de l'Environnement d'Ile de France. 36, 96

Oerder, V., Colas, F., Echevin, V., Codron, F., Tam, J., Belmadani, A., 2015. Peru-Chile upwelling dynamics under climate change. J Geophys Res. 118, 123, 124

Oerder, V., Colas, F., Echevin, V., Masson, S., Hourdin, C., Jullien, S., Madec, G., Lemarié, F., 2016. Mesoscale SST–wind stress coupling in the Peru–Chile current system: Which mechanisms drive its seasonal variability? Climate Dynamics 47 (7-8), 2309–2330. 39, 89, 125, 126

Oerder, V., Colas, F., Echevin, V., Masson, S., Lemarié, F., 2018. Impacts of the Mesoscale Ocean-Atmosphere Coupling on the Peru-Chile Ocean Dynamics: The Current-Induced Wind Stress Modulation. Journal of Geophysical Research: Oceans 123 (2), 812–833. 125

Pauly, V., Christensen, V., 1995. Primary production required to sustain global fisheries. Nature 374, 255–257. 1

Perlin, N., Skyllingstad, E., Samelson, R., 2011. Coastal Atmospheric Circulation around an Idealized Cape during Wind-Driven Upwelling Studied from a Coupled Ocean–Atmosphere Model. Monthly Weather Review 139, 809–829. 106

Picaut, J., Hackert, E., Busalacchi, A., Murtugudde, R., Lagerloef, G., 2002. Mechanisms of the 1997-1998 El Niño-La Niña, as inferred from space-based observations. J Geophys Res Oceans. 107, 3037. 6

Rahn, D., Garreaud, R., 2013. A synoptic climatology of the near- surface wind along the west coast of south america. Int. J. Climatol. 34, 3628–3647. 3

Rasmussen, R., Liu, C., Ikeda, K., Gochis, D., Yates, D., Chen, F., Tewari, M., Barlage, M., Dudhia, J., Yu, W., Miller, K., Arsenault, K., Grubišić, V., Thompson, G., Gutmann, E., 2011. High-resolution coupled climate runoff simulations of seasonal snowfall over colorado: A process study of current and warmer climate. Journal of Climate 24 (12), 3015–3048. 97

Renault, L., Hall, A., McWilliams, J. C., 2015. Orographic shaping of us west coast wind profiles during the upwelling season. Climate Dynamics 46 (1-2), 273–289.
URL http://dx.doi.org/10.1007/s00382-015-2583-4 4, 104

Reynolds, R. W., Smith, T. M., Liu, C., Chelton, D. B., Casey, K. S., Schlax, M. G., 2007. Daily high-resolution-blended analyses for sea surface temperature. J. Climate, 5473– 5496. 23, 97

Richter, I., 2015. Climate model biases in the eastern tropical oceans: Causes, impacts and ways forward. Wiley Interdisciplinary Reviews: Climate Change 6 (3), 345–358. 97

Richter, I., Mechoso, C. R., 2006. Orographic influences on subtropical stratocumulus. J. Atmos. Sci. 63, 2585–2601. 2

Rykaczewski, R. R., Dunne, J. P., Sydeman, W. J., García-Reyes, M., Black, B. A., Bograd, S. J., 2015. Poleward displacement of coastal upwelling-favorable winds in the ocean's eastern boundary currents through the 21st century. Geophysical Research Letters 42 (15), 6424–6431. 14

Ryther, J., 1969. Photosynthesis and fish production in the sea. Science 166, 72–76. 1

Saha, S., Moorthi, S., Pan, H., Wu, X., Wang, J., Nadiga, S., Tripp, P., Kistler, R., Woollen, J., Behringer, D., Liu, H., Stokes, D., Grumbine, R., Gayno, G., Wang, J., Hou, Y., Chuang, H., Juang, H., Sela, J., Iredell, M., Treadon, R., Kleist, D., Van Delst, P., Keyser, D., Derber, J., Ek, M., Meng, J., Wei, H., Yang, R., Lord, S., Van Den Dool, H., Kumar, A., Wang, W., Long, C., Chelliah, M., Xue, Y., Huang, B., Schemm, J., Ebisuzaki, W., Lin, R., Xie, P., Chen, M., Zhou, S., Higgins, W., Zou, C., Liu, Q., Chen, Y., Han, Y., Cucurull, L., Reynolds, R., Rutledge, G., Goldberg, M., 2010. The NCEP climate forecast system reanalysis. Bull. Am.Meteorol. Soc. 91 (8), 1015–1057. 21

Skamarock, W., Klemp, J., Dudhi, J., Gill, D., Barker, D., Duda, M., Huang, X.-Y., Wang, W., Powers, J., 2008. A Description of the Advanced Research WRF Version 3. Technical Report (June), 113. 23

Snyder, M. A., Sloan, L. C., Diffenbaugh, N. S., Bell, J. L., 2003. Future climate change and upwelling in the California Current. Geophysical Research Letters 30 (15), 1–4. 18

Soares, P. M. M., Lima, D. C. A., Semedo, , Cardoso, R. M., Cabos, W., Sein, D., 2018. The North African coastal low level wind jet: a high resolution view. Climate Dynamics, 1–20. 106

Suarez, M. J., Schopf, P. S., 1988. A delayed action oscillator for ENSO. Journal of the Atmospheric Sciences 45, 3283–3287. 5

Sydeman, W. J., García-Reyes, M., Schoeman, D. S., Rykaczewski, R. R., Thompson, S. A., Black, B. A., Bograd, S. J., 2014. Climate change and wind intensification in coastal upwelling ecosystems. Science 345 (6192), 77–80. 15

Takahashi, K., Battisti, D. S., 2007. Processes controlling the mean tropical pacific precipitation pattern. Part I: The Andes and the eastern Pacific ITCZ. Journal of Climate 20 (14), 3434–3451. 2

Takahashi, K., Martínez, A. G., 2017. The very strong El Niño in 1925 in the far-eastern Pacific. Climate Dynamics 0 (0), 0. 120, 121

Tokinaga, H., Xie, S. P., 2011. Wave- and Anemometer-based sea surface wind (WASWind) for climate change analysis. Journal of Climate 24 (1), 267–285. 15

van Vuuren, D. P., Edmonds, J., Kainuma, M., Riahi, K., Thomson, A., Hibbard, K., Hurtt, G. C., Kram, T., Krey, V., Lamarque, J. F., Masui, T., Meinshausen, M., Nakicenovic, N., Smith, S. J., Rose, S. K., 2011. The representative concentration pathways: An overview. Climatic Change 109 (1), 5–31. 10, 12

Vargas, G., Pantoja, S., Rutllant, J. A., Lange, C. B., Ortlieb, L., 2007. Enhancement of coastal upwelling and interdecadal ENSO-like variability in the Peru-Chile Current since late 19th century. Geophysical Research Letters 34 (13), 1–6. 15

Vecchi, G. A., Soden, B. J., 2007. Global warming and the weakening of the tropical circulation. Journal of Climate 20 (17), 4316–4340. 14

Wallace, J. M., Mitchell, T. P., Deser, C., 1989. The Influence of Sea-Surface Temperature on Surface Wind in the Eastern Equatorial Pacific: Seasonal and Interannual Variability. 8

Wang, C., Zhang, L., Lee, S. K., Wu, L., Mechoso, C. R., 2014. A global perspective on CMIP5 climate model biases. Nature Climate Change 4 (3), 201–205. 95

Wang, D., Gouhier, T. C., Menge, B. A., Ganguly, A. R., 2015. Intensification and spatial homogenization of coastal upwelling under climate change. Nature 518 (7539), 390–394. URL http://dx.doi.org/10.1038/nature14235 14

Wood, R., Mechoso, C. R., Bretherton, C. S., Weller, R. A., Huebert, B., Straneo, F., Albrecht, B. A., Coe, H., Allen, G., Vaughan, G., Daum, P., Fairall, C., Chand, D., Gallardo Klenner, L., Garreaud, R., Grados, C., Covert, D. S., Bates, T. S., Krejci, R., Russell, L. M., De Szoeke, S., Brewer, A., Yuter, S. E., Springston, S. R., Chaigneau, A., Toniazzo, T., Minnis, P., Palikonda, R., Abel, S. J., Brown, W. O., Williams, S., Fochesatto, J., Brioude, J., Bower, K. N., 2011. The VAMOS ocean-cloud-atmosphere-land study regional experiment (VOCALS-REx): Goals, platforms, and field operations. Atmospheric Chemistry and Physics 11 (2), 627–654. 23

Wyant, M. C., Wood, R., Bretherton, C. S., Mechoso, C. R., Bacmeister, J., Balmaseda, M. A., Barrett, B., Codron, F., Earnshaw, P., Fast, J., Hannay, C., Kaiser, J. W., Kitagawa, H., Klein, S. A., Khler, M., Manganello, J., Pan, H. L., Sun, F., Wang, S., Wang, Y., 2010. The PreVOCA experiment: Modeling the lower troposphere in the Southeast Pacific. Atmospheric Chemistry and Physics 10 (10), 4757–4774. 90

Wyrtki, K., 1975. El Niño-The Dynamic Response of the Equatorial Pacific Oceanto Atmospheric Forcing. 5, 8

Zhang, D. L., Anthes, R. A., 1982. A high-resolution model of the planetary boundary layer sensitivity tests and comparisons with SESAME - 79 data. J. Appl. Meteor. 21, 1594–1609. 28

Zhang, Y., Rossow, W., Lacis, A., Oinas, V., Mishchenko, M., 2004. Calculation of radiative fluxes from the surface to top of atmosphere based on ISCCP and other global data sets: Refinements of the radiative transfer model and the input data. J. Geophys. Res. 23